1-1-2016

Studying the Large Scale Structure and interstellar Medium of Galaxies During the Epochs of Peak Cosmic Star formation and Reionization With Infrared Fine Structure Lines

Bade D. Uzgil
University of Pennsylvania, badeuzgil@gmail.com

Recommended Citation

Uzgil, Bade D., "Studying the Large Scale Structure and interstellar Medium of Galaxies During the Epochs of Peak Cosmic Star formation and Reionization With Infrared Fine Structure Lines" (2016). *Publicly Accessible Penn Dissertations*. 2070.
http://repository.upenn.edu/edissertations/2070

Studying the Large Scale Structure and interstellar Medium of Galaxies During the Epochs of Peak Cosmic Star formation and Reionization With Infrared Fine Structure Lines

Abstract

Infrared (IR) fine-structure (FS) lines from trace metals in the interstellar medium (ISM) of galaxies are valuable diagnostics of the physical conditions in a broad range of astrophysical environments, such gas irradiated by stellar far-ultraviolet (FUV) photons or X-rays from accreting supermassive black holes, called active galactic nuclei (AGN). The transparency of these lines to dust and their high escape fractions into the intergalactic medium (IGM) render them as useful probes to study the epochs of peak cosmic star formation (SF) and Reionization.

Chapter 1 of this thesis is a study of the ISM of the Cloverleaf quasar. Observations of IR FS lines from singly ionized carbon and neutral oxygen have allowed us to assess the physical conditions—parametrized by their gas density and the impingent FUV flux—prevalent in atomic gas heated by stellar FUV photons. We find that UV heating from local SF is not sufficient to explain the measured FS and molecular luminosities, and suggest that X-ray heating from the AGN is required to simultaneously explain both sets of data. The general picture of the Cloverleaf ISM that emerges from our composite model is one where the [CII] and [OI]63 line emission is produced primarily within PDRs and HII regions of a 1.3-kpc wide starburst, which is embedded in a denser XDR component that is the dominant source of heating for the CO gas. The fact that the star-forming PDR and HII region gas is co-spatial with the XDR—and within ~ 650 pc of the accreting black hole—provides strong evidence that SF is ongoing while immersed in a strong X-ray radiation field provided by the nearby AGN. This finding has implications for the co-evolution of supermassive black holes and their host galaxies. The work in this chapter will be submitted for first-author publication imminently.

In Chapter 2, we explore the possibility of studying the redshifted far-IR fine-structure line emission using the three-dimensional (3-D) power spectra obtained with an imaging spectrometer. The intensity mapping approach measures the spatio-spectral fluctuations due to line emission from all galaxies, including those below the individual detection threshold. The technique provides 3-D measurements of galaxy clustering and moments of the galaxy luminosity function. Furthermore, the linear portion of the power spectrum can be used to measure the total line emission intensity including all sources through cosmic time with redshift information naturally encoded. Total line emission, when compared to the total star formation activity and/or other line intensities reveals evolution of the interstellar conditions of galaxies in aggregate. As a case study, we consider measurement of [CII] autocorrelation in the $0.5 < z < 1.5$ epoch, where interloper lines are minimized, using far-IR/submm balloon-borne and future space-borne instruments with moderate and high sensitivity, respectively. In this context, we compare the intensity mapping approach to blind galaxy surveys based on individual detections. We find that intensity mapping is nearly always the best way to obtain the total line emission because blind, wide-field galaxy surveys lack sufficient depth and deep pencil beams do not observe enough galaxies in the requisite luminosity and redshift bins. Also, intensity mapping is often the most efficient way to measure the power spectrum shape, depending on the details of the luminosity function and the telescope aperture. The work in this chapter has been published in Uzgil et al. (2014).

In the final Chapter, we consider the extension of intensity mapping experiments targeting IR FS lines to the late stages of the Epoch of Reionization (EoR), at $z \sim 7$. Intensity mapping experiments of emission lines from the ISM of galaxies are highly complementary to experiments that are aiming to detect the 21 cm power spectrum during the same epoch, as the former is a direct probe of the sources of Reionization, and the latter is a probe of the effect of those sources on the surrounding IGM. Since current and planned observations are limited by cosmic variance at the bright end of the galaxy luminosity function, and will not be able to detect the faintest galaxies responsible for a significant fraction of the ionizing photon supply during EoR, intensity mapping is an appealing approach to study the nature and evolution of galaxies during this stage in the history of the Universe. Again, the utility of FS lines as ISM diagnostics, combined with the ability of intensity mapping to measure redshift-evolution in mean intensity of individual lines or the evolution of line ratios (constructed from multiple cross-power spectra), presents a unique and tantalizing opportunity to directly observe changes in properties of interstellar medium (such as hardness of the ionizing spectrum in galaxies and metallicity) that are important to galaxy evolution studies.

Degree Type
Dissertation

Degree Name
Doctor of Philosophy (PhD)

Graduate Group
Physics & Astronomy

First Advisor
James E. Aguirre

Second Advisor
Charles M. Bradford

Subject Categories
Astrophysics and Astronomy

STUDYING THE LARGE SCALE STRUCTURE AND INTERSTELLAR MEDIUM OF GALAXIES DURING THE EPOCHS OF PEAK COSMIC STAR FORMATION AND REIONIZATION WITH INFRARED FINE STRUCTURE LINES

Bade D. Uzgil

A DISSERTATION

in

Physics & Astronomy

Presented to the Faculties of the University of Pennsylvania in Partial Fulfillment of the Requirements for the Degree of Doctor of Philosophy

2016

Supervisor of Dissertation	Co-Supervisor of Dissertation
James E. Aguirre, Professor	Charles M. Bradford, Doctor

Graduate Group Chairperson

Marija Drndic, Professor

Dissertation Committee:
James Aguirre, Prof. Charles M. Bradford, Dr. Adam Lidz, Prof.
Gary Bernstein, Prof. Mark Devlin, Prof. Evelyn Thomson, Prof.

Ad astra per alia porci.
—John Steinbeck

ABSTRACT

STUDYING THE LARGE SCALE STRUCTURE AND INTERSTELLAR MEDIUM OF GALAXIES DURING THE EPOCHS OF PEAK COSMIC STAR FORMATION AND REIONIZATION WITH INFRARED FINE STRUCTURE LINES

Bade D. Uzgil

James E. Aguirre

Charles M. Bradford

Infrared (IR) fine-structure (FS) lines from trace metals in the interstellar medium (ISM) of galaxies are valuable diagnostics of the physical conditions in a broad range of astrophysical environments, such gas irradiated by stellar far-ultraviolet (FUV) photons or X-rays from accreting supermassive black holes, called active galactic nuclei (AGN). The transparency of these lines to dust and their high escape fractions into the intergalactic medium (IGM) render them as useful probes to study the epochs of peak cosmic star formation (SF) and Reionization.

Chapter 1 of this thesis is a study of the ISM of the Cloverleaf quasar. Observations of IR FS lines from singly ionized carbon and neutral oxygen have allowed us to assess the physical conditions—parametrized by their gas density and the impingent FUV flux—prevalent in atomic gas heated by stellar FUV photons. We find that UV heating from local SF is not sufficient to explain the measured FS and molecular luminosities, and suggest that X-ray heating from the AGN is required to simultaneously explain both sets of data. The general picture of the Cloverleaf ISM that emerges from our composite model is one where the [CII] and [OI]63 line emission is produced primarily within PDRs and HII regions of a 1.3-kpc wide starburst, which is embedded in a denser XDR component that is the dominant source of heating for the CO gas. The fact that the star-forming PDR and HII region gas is co-spatial with the XDR—and within ~ 650 pc of the accreting black hole—provides strong evidence that SF is ongoing while immersed in a strong X-ray radiation field provided by the nearby AGN. This finding has implications for the co-evolution of supermassive black holes and their host galaxies. The work in this chapter will be submitted for first-author publication imminently.

In Chapter 2, we explore the possibility of studying the redshifted far-IR fine-

structure line emission using the three-dimensional (3-D) power spectra obtained with an imaging spectrometer. The intensity mapping approach measures the spatio-spectral fluctuations due to line emission from all galaxies, including those below the individual detection threshold. The technique provides 3-D measurements of galaxy clustering and moments of the galaxy luminosity function. Furthermore, the linear portion of the power spectrum can be used to measure the total line emission intensity including all sources through cosmic time with redshift information naturally encoded. Total line emission, when compared to the total star formation activity and/or other line intensities reveals evolution of the interstellar conditions of galaxies in aggregate. As a case study, we consider measurement of [CII] autocorrelation in the $0.5 < z < 1.5$ epoch, where interloper lines are minimized, using far-IR/submm balloon-borne and future space-borne instruments with moderate and high sensitivity, respectively. In this context, we compare the intensity mapping approach to blind galaxy surveys based on individual detections. We find that intensity mapping is nearly always the best way to obtain the total line emission because blind, wide-field galaxy surveys lack sufficient depth and deep pencil beams do not observe enough galaxies in the requisite luminosity and redshift bins. Also, intensity mapping is often the most efficient way to measure the power spectrum shape, depending on the details of the luminosity function and the telescope aperture. The work in this chapter has been published in Uzgil et al. (2014).

In the final Chapter, we consider the extension of intensity mapping experiments targeting IR FS lines to the late stages of the Epoch of Reionization (EoR), at $z \sim 7$. Intensity mapping experiments of emission lines from the ISM of galaxies are highly complementary to experiments that are aiming to detect the 21 cm power spectrum during the same epoch, as the former is a direct probe of the sources of Reionization, and the latter is a probe of the effect of those sources on the surrounding IGM. Since current and planned observations are limited by cosmic variance at the bright end of the galaxy luminosity function, and will not be able to detect the faintest galaxies responsible for a significant fraction of the ionizing photon supply during EoR, intensity mapping is an appealing approach to study the nature and evolution of galaxies during this stage in the history of the Universe. Again, the utility of FS lines as ISM diagnostics, combined with the ability of intensity mapping to measure redshift-evolution in mean intensity of individual lines or the evolution of line ratios (constructed from multiple cross-power spectra), presents a unique and tantalizing opportunity to directly observe changes in properties of interstellar medium (such as hardness of the ionizing spectrum in galaxies and metallicity) that are important to galaxy evolution studies.

Contents

Preface

The study of cosmology versus the study of astrophysics is the study of the whole versus its parts, of the Universe versus its occupants, of, for example, the acceleration of space-time versus the ignition of supernovae. Certain questions are better addressed, undeniably, in one field and not the other—"Do we live in a multiverse?"—but some are fully understood only where the two fields intersect. One such question, of particular relevance to this thesis, concerns the origin and evolution of galaxies, such as our own Milky Way or our neighbors, Messier 82 (M 82) and Markarian 231 (Mrk 231).[1]

In order to discuss the evolution of galaxies from a purely cosmological perspective, it is first necessary to trade in the notion of a galaxy as a vast collection of stars, gas, and dust for a more austere definition, namely, a perturbation $\frac{\Delta\rho}{\rho}$ in density ρ. Indeed, it is a remarkable fact that all large-scale structure observed in the present Universe—from individual galaxies and superclusters (containing, say, some 10^5 galaxies) to the filaments and voids of the "cosmic web"—trace their origins to tiny fluctuations in density when the Universe was only a fraction of a second old; and, this fact is one of the predictions of the current most successful cosmological model.

The current model, however, cannot predict precisely the level of density perturbations in the early Universe which gave rise to the present assembly of mass in various observed structures. Instead, observations pin the order of density perturbations to $\frac{\Delta\rho}{\rho} \sim 10^{-5}$ at a time when the Universe was roughly 3.7×10^5 years old, corresponding to a time when the equilibrium between photons, protons, electrons, and hydrogen atoms was broken such that neutral hydrogen could outnumber electrons and protons. From then on, photons could decouple from matter,[2] expand with the Universe, cool from ~ 3000 K to 2.7 K, and eventually reach telescopes today as the Cosmic Microwave Background (CMB). The formation of the CMB, also referred to simply as "decoupling" or "recombination," marks a critical stage in the Universe's evolution, as neutral hydrogen is produced in abundance and will begin to collapse rapidly when the energy density of matter dominates over radiation in the Universe. (In fact, the collapse of all kinds of matter, including non-baryonic

---

[1] Here, "neighbor" is meant strictly in the astronomical sense. M 82 is located 2.9 Mpc = 2.9×10^6 pc = 8.9×10^{22} m from the Milky Way and Mrk 231, 180 Mpc = 1.8×10^8 pc = 5.5×10^{24} m.

[2] More precisely, photons could travel freely without being Thomson scattered from baryons.

matter, commences after decoupling because the speed of sound ceases to be relativistic.) If we suppose that matter consists entirely of baryons, then simply evolving the density perturbations—imprinted in the CMB as fluctuations in temperature $\frac{\Delta T}{T} \sim 10^{-5}$—to grow in time as expected for a matter-dominated Universe, i.e., allowing them to grow linearly with the cosmological expansion, under-predicts the observed range of density fluctuations today, which can be as high as $\frac{\Delta\rho}{\rho} \sim 10 - 10^2$ for galaxy clusters (returning to the astrophysicist's parlance). The inclusion of a significant non-relativistic, or cold, dark matter (DM) component into the current cosmological model, which we can now refer to somewhat meaningfully as the Λ-CDM model,[3] means, for example, that matter-domination occurs at an earlier time, giving perturbations more time to grow; since DM, by nature, does not interact with radiation, the perturbations in the DM density field also tend to grow more efficiently.

Once the amplitudes of density perturbations become large enough, their growth is no longer linear, and can be computed with N-body simulations (e.g., Springel et al. (2005)) that account for gravitational interactions between large numbers of particles. Alternatively, the nonlinear development of perturbations can be described with theories of collapse for spheroids (Press & Schechter 1974; White & Rees 1978) or, more accurately, ellipsoids (Sheth et al. 2001), in which matter collapses to smaller radii and forms gravitationally bound objects in virial equilibrium, with the virial mass, M, at the time of collapse becoming progressively larger at later times—an example of the hierarchical growth that governs the formation of structures in the Universe. The DM collapses first because the amplitude of $\frac{\Delta\rho}{\rho}$ in the DM density field was already larger than 10^{-5} at the formation of the CMB due to the premature growth of perturbations during the radiation-dominated era, forming bound objects called halos. These halos served as hosts for the formation of stars and later galaxies as baryons proceeded to accumulate in the attractive gravitational potential of the DM. Through gravitational interactions and mergers, the halos and baryons accumulate mass, exemplifying further the principle of hierarchical structure growth that ultimately results in the large-scale structure of the cosmos observed today.

Therefore, in the broad sense that galaxies initially formed from the collapse of baryons in DM halos, their evolution is inextricably linked to that of their hosts. While the abundance, spatial clustering, mass distribution, and other key properties of DM halos can be described with analytic theories (cf. Cooray & Sheth (2002) for a summary) introduced above, simply assuming that galaxies and DM halos follow the same evolutionary path—one that is theoretically well understood—leads to a number of predictions that do not agree with observations, such as the history of star formation in the Universe.

---

[3] Λ denotes the small, but non-zero cosmological constant which drives the observed acceleration of the Universe in the present day. The effect of Λ on density perturbations is to slow their growth.

Star formation in galaxies and dark matter halos The star formation rate (SFR, units of $\mathrm{M}_\odot$ yr^{-1}) is a useful indicator of a galaxy's evolutionary phase. According to observations (e.g., Daddi et al. (2007), Elbaz et al. (2011)) in the nearby and distant Universe, there is a correlation between a galaxy's stellar mass and its SFR (per unit stellar mass[4]). Galaxies may spend the most time in a phase where they form stars in line with this correlation—called the galaxy "main sequence"—compared to relatively short-lived phases during which star formation is enhanced (i.e., undergoing a "starburst" phase, as in M 82) and suppressed. Measurements of the space density of star formation, ρ_{SFR} ($\mathrm{M}_\odot$ yr^{-1} Mpc^{-3}), in the Universe across cosmic timescales (i.e., on the order $\sim 10^{9-10}$ yr $= 1 - 10$ Gyr) are a means of piecing together a global view of galaxy evolution (Madau & Dickinson 2014).

Suppose, then, that the evolution of DM halos is sufficient to describe the cosmic history of star formation. If galaxies merely follow the DM halo evolution, without any additional astrophysical processes involved, then the relation between SFR and DM halo mass should maintain a simple linear dependence. Then it is possible to use theoretical predictions for the number, or fraction, f_{coll}, of halos greater than a given mass, M_{min}, that have collapsed at a given time, or redshift z,[5] in the Universe's history in order to predict ρ_{SFR} at that time:

$$\rho_{\mathrm{SFR}}(z) \propto f_{coll}(M > M_{min}; z)\bar{\rho}(z)/t_{\mathrm{H}}(z), \tag{0.0.1}$$

where $\bar{\rho}(z)$ is the redshift-dependent average background density of DM in the Universe, and $t_{\mathrm{H}}(z)$ is the age of the Universe at z, i.e., the Hubble time at z. To calculate $f_{coll}(M > M_{min}; z)$, we have used the Sheth-Tormen halo mass function (Sheth et al. 2001), $\frac{\mathrm{d}N}{\mathrm{d}M\mathrm{d}V}$, which describes the average number N of DM halos between a mass M and $M + \mathrm{d}M$ per infinitesimal unit of (comoving[6]) volume $\mathrm{d}V$. The righthand panel of Figure 1 shows the resulting evolution of ρ_{SFR} with redshift, as well as empirically-based models from Robertson et al. (2015) and Hopkins & Beacom (2006a). The integral of ρ_{SFR} over the time spanned by this toy model has been normalized to match the integral of ρ_{SFR} reported in Robertson et al. (2015), since here we are mainly interested in whether the shape of the cosmic history of

---

[4] The SFR that is normalized by a galaxy's stellar mass is often referred to as the specific SFR (sSFR).

[5] Note that units of time are expressed in terms of redshift, z, which is defined in relation to the scale factor, $a(t)$, of the Universe: $z = \frac{a(t=0)}{a(t)} - 1$. The scale factor describes the extent to which a physical length d has been stretched from its present length d_0 due to the expansion of the Universe at a given time t, such that $d = a(t)d_0$, with $a(t = 0) = 1$ (and hence $z = 0$) locally. Because the wavelength, λ_{em}, of radiation emitted at a time t is similarly stretched by cosmological expansion, spectroscopy offers observers a useful means of identifying a source's redshift from its spectral line emission.

[6] A "comoving" distance in cosmology is used to refer to distances between objects that have been corrected for the expansion of the Universe. See, for instance, Hogg (1999) for definitions of relevant distances in cosmology.

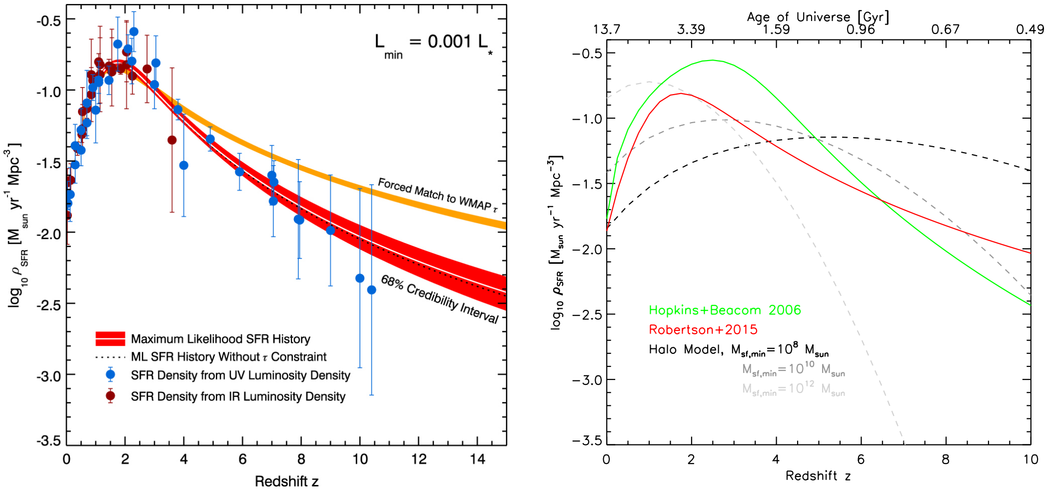

Figure 1: Cosmic star formation rate density, $\rho_{\rm SFR}$, as a function of redshift, z. (*left*): Blue and red data points indicate UV and IR luminosity densities, $\rho_{\rm UV}$ and $\rho_{\rm IR}$, respectively, converted to $\rho_{\rm SFR}$ with prescriptions from Madau & Dickinson (2014) and Kennicutt (1998a). The respective luminosity densities have been calculated by integrating observed luminosity functions down to 0.001 times the characteristic galaxy luminosity at a given redshift, L_*, as defined in the Schechter or double power-law formalism. The white line represents the maximum likelihood model for $\rho_{\rm SFR}$, with 1σ confidence region highlighted in red, when fitting a model to the data with the constraint that the model reproduces the *Planck* satellite's measurement of the Thomson optical depth, τ_e, assuming that the cosmic ionization rate is proportional to the cosmic star formation rate density. Dashed blue curve shows the maximum likelihood model of $\rho_{\rm SFR}$ when the *Planck* constraint is ignored. The orange swath is the result when the model is forced to match τ_e measured by WMAP. Figure from Robertson et al. (2015). (*right*): Models for $\rho_{\rm SFR}(z)$ according to Robertson et al. (2015) (red curve; same as white curve in left panel of this Figure) and Hopkins & Beacom (2006a) (green curve). Assuming that star formation rate is linearly related to DM halo mass, M—with constant of proportionality between $\rho_{\rm SFR}$ and M determined by forcing the integrated SFR density (in the interval $0 \leq z \leq 10$) to equal that of the Robertson et al. (2015) model—and applying the halo mass function from Sheth et al. (2001) to determine the population of DM halos with mass greater than M_{min} as a function of redshift, yields the cosmic star formation rate histories shown as the dashed curves. Different curves correspond to different assumptions regarding the the minimum mass, $M_{min} = M_{{\rm SF},min}$, at which a DM halo can begin forming stars, namely, $M_{{\rm SF},min} = 10^8$ (black), 10^{10} (dark gray), and 10^{12} $M_\odot$ (light gray).

$\rho_{\rm SFR}$ matches the observed trend with redshift; the prescribed dependence on $\rho_{\rm SFR}$ with M is linear, anyway, and so the amplitude can be forced to agree with observations by changing the constant of proportionality between them. This simple model of galaxy evolution is only sensitive to the mass at which a halo can begin forming stars, denoted $M_{{\rm SF},min}$. For example, halo masses between $\sim 10^8$–10^9 $\rm M_\odot$ are physically-motivated choices for $M_{min} = M_{{\rm SF},min}$, as these masses correspond to virial temperatures in the halo that ionize hydrogen and allow the gas to cool radiatively,[7] which, in turn, allows the gas to contract further and potentially form stars. In any case, the peak in cosmic star formation activity occurs when the fraction of mass contained in virialized DM halos of mass $M_{{\rm SF},min}$ is at a maximum, which happens at progressively later times (i.e., lower redshifts) for larger values of $M_{{\rm SF},min}$. Importantly, there is no single choice of $M_{{\rm SF},min}$ that matches the observed history of $\rho_{\rm SFR}$. This disagreement suggests that *the relation between SF and halo mass is highly non-linear, and that the star formation efficiency changes with halo mass.* The sources of this non-linearity are the complex astrophysical processes between baryons which we neglected in our toy model, but which govern the evolution of galaxies in addition to the gravitational influence of DM halo environment. Triggers of starburst activity, for example, which raise galaxies above the star-forming "main sequence," could be the result of galaxy-galaxy mergers or infall of cold gas into galaxies from DM halos. Feedback between accreting supermassive black holes at the centers of galaxies, called active galactic nuclei (AGN), and star-forming gas also appears to be play an important role in galaxy evolution—possibly a mechanism for regulating SF—and will be explored in Chapter 1 of this thesis.

Studies that target the Universe when it was approximately between 2 and 6 billion years old (or, between $z \approx 3$ and 1, respectively) probe a critical time frame in the evolution of galaxies, corresponding to the peak of cosmic SF as indicated in Figure 1, i.e, when galaxies appear to have been the most active in forming stars; $\rho_{\rm SFR}$ in this redshift range is 10 times higher than in the local ($z \sim 0$) Universe. SFR estimates in the lefthand panel of Figure 1 have been calculated from luminosity densities of ultraviolet ($\rho_{\rm UV}$; blue data points) and infrared ($\rho_{\rm IR}$; red data points) light rom galaxies, using prescriptions that take into account the correlation between a galaxy's UV and IR luminosities and its SFR (Madau & Dickinson 2014; Kennicutt 1998a). In the presence of interstellar dust, UV radiation from the gas within a galaxy is reduced from its intrinsic luminosity because it is readily absorbed by the dust grains, and re-emitted at IR wavelengths. Thus, while the observed UV luminosity of a galaxy indicates the energy output of its stellar populations—these are the primary sources of Lyman continuum photons[8] in purely star-forming systems—$\rho_{\rm UV}$ can lead to an underestimate of $\rho_{\rm SFR}$ for dusty star-forming galaxies (DSFGs) unless the correct extinction factors are applied. In Figure 2, the increasing fraction with redshift of SF in dust-rich environments

---

[7] via hydrogen recombinations and *bremsstrahlung*

[8] Photons with energies greater than 1 Rydberg = 13.6 eV.

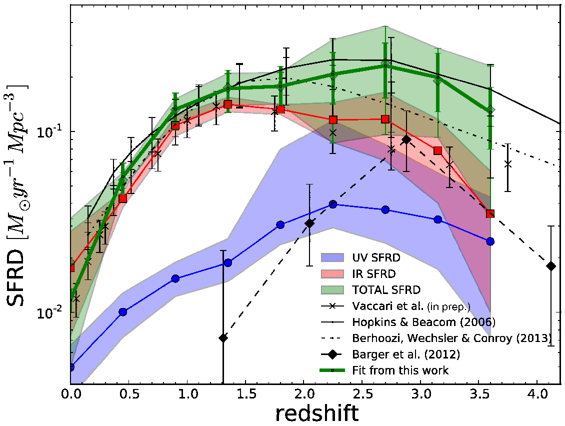

Figure 2: Cosmic star formation rate density ($\rho_{\rm SFR}$, or SFRD; green curve) as a function of redshift, deconstructed into contributions from SFRD as measured from $\rho_{\rm IR}$ (red curve) and $\rho_{\rm UV}$ (blue curve). UV luminosity densities in this Figure have not been corrected for extinction by dust. Figure from Burgarella et al. (2013a).

is illustrated by comparing $\rho_{\rm SFR}$ inferred from the measured (i.e., uncorrected for dust extinction) UV and IR emission from galaxies. By a redshift of $z \sim 0.5$, the so-called "hidden," or dust-obscured, fraction of $\rho_{\rm SFR}$ is already 80%, and remains between 75−90% throughout the epoch of peak SF activity (Burgarella et al. 2013a). The relative importance of obscured SF in this cosmic epoch motivates the need to understand the nature of extinction in these sources, and to have independent measures of $\rho_{\rm IR}$ for a more accurate bolometric estimate of SF. Furthermore, it also highlights the utility, in general, of probes of the SF process in galaxies during this cosmic epoch that are not significantly extincted by dust.

Far-infrared emission lines Since the the absorption efficiency of dust grains generally varies inversely with wavelength, IR emission lines emitted directly from star-forming gas provide a relatively unobscured view into the physical conditions in DSFGs compared to shorter-wavelength diagnostics of the SF process, such as the electronic transitions between energy levels of principal quantum numbers in the hydrogen (H) atom. While hydrogen is, indeed, the most abundant element in galaxies (and the Universe), the first excited state of atomic H is 10.3 eV ($E/k_{\rm B} = 1.2 \times 10^5$ K) above the ground level, so a downward transition from this state requires very hot gas ($T \gtrsim 10^4$ K) and results in emission of a UV Lyman-α photon, which is immediately absorbed by dust. Being a resonance line, Lyman-α photons also have large cross-sections for scattering with neutral hydrogen, which can complicate the interpretation of observed flux and make it difficult to understand intrinsic properties of the emitting source. Heavier elements like carbon and oxygen, which are only fractionally as abundant as hydrogen, have fine-structure (FS) splittings in their ground state that correspond to low-lying energy levels with energies above ground on the order of $10 - 10^3$ K. Transitions from these levels are excited in a

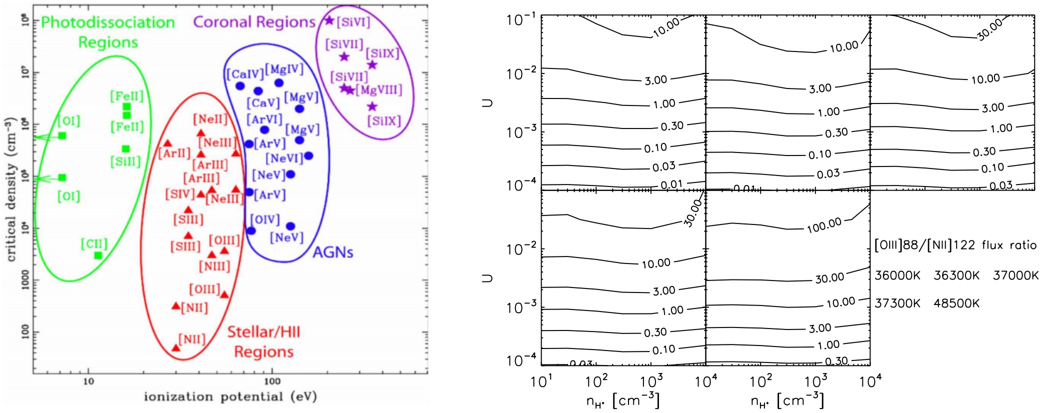

Figure 3: (*left:*) Infrared fine-structure line transitions frequently used in studies of the ISM. Lines are plotted as functions of their critical density and ionization energy, and are color-coded according to their application as diagnostics of regions of neutral and ionized gas: photodissociation regions (green), stellar HII regions (red), active galactic nuclei (blue), and coronal regions (purple). Figure from Spinoglio et al. (2009). (*right:*) Sensitivity of the flux ratio of [OIII]88 μm to [NII]122 μm emission to stellar temperature. Fluxes have been computed for plane-parallel HII region models using the publicly available radiative transfer code *Cloudy* (Ferland et al. 1998), and are presented as functions of the ionized gas density n_{H^+} (units of cm^{-3}) and the dimensionless ionization parameter U, which specifies the ratio of the flux of ionizing photons to n_{H^+}. The input ionizing spectra for the different HII region models are appropriate for stars with effective temperatures of 36000 K, 36300 K, 37000 K, 37300 K, and 48500 K. Note that the flux ratio is relatively independent of the ionized gas density, which is expected for a ratio of two ions with similar critical densities (cf. left panel of this Figure.)

wide range of environments throughout the star-forming medium, and result in the emission of IR photons—two facts which combine to position the IR FS lines as well-suited probes of galaxies during the epoch of peak cosmic SFR density. In fact, the IR FS lines are often the dominant coolants of the ionized and neutral atomic gas in galaxies, known collectively—along with molecular gas and a mixture of solids like dust and ice—as the interstellar medium (ISM); the total luminosity in a single FS line, such as the 158 μm transition in the ground state of singly ionized carbon, can account for as much as 0.1–1% of a galaxy's total IR luminosity.

The left panel of Figure 3 presents a set of IR FS lines that are commonly observed to originate throughout the ISM. These emission lines can be used to probe a wide range of astrophysical environments, including, e.g., regions of dense ionized hydrogen gas around stars (called stellar HII regions; corresponding emission lines color-coded in red in Figure 3) and regions of neutral hydrogen gas impinged upon by stellar far-UV photons (called photodissociation regions, or PDRs; color-coded in green), as well as regions of highly ionized gas around accreting supermassive black holes (called active galactic nuclei, or AGN; color-coded in blue). As with workhorse UV and optical emission lines often employed to diagnose physical conditions in the relatively unextincted ISM, the utility of the IR FS lines to characterize physical conditions (e.g., density, flux of ionizing photons, dynamics, etc.) in a galaxy's ISM is maximized by comparing observed fluxes in two or more lines in the form of flux ratios.

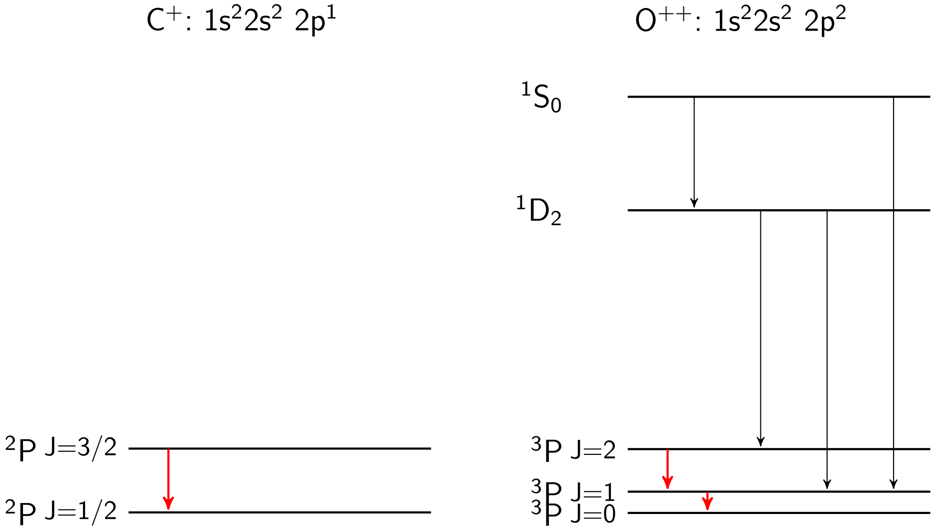

Figure 4: Schematic energy level diagrams for ground state electron configurations of singly ionized carbon, C^{+} (*left*), and doubly ionized oxygen, O^{++} (*right*). Energy levels are labeled using the spectroscopic notation, $^{2S+1}L_J$, where S, L, and J, refer to the spin, orbital, and total angular momentum quantum numbers, respectively. Downward arrows indicate electronic transitions. Important fine-structure transitions in the ISM of galaxies, namely, $^{2}P_{3/2} \rightarrow {}^{2}P_{1/2}$ for [CII] and $^{3}P_{1} \rightarrow {}^{3}P_{0}$ and $^{3}P_{2} \rightarrow {}^{3}P_{1}$ for [OIII], are highlighted in red. These transitions correspond to emission lines [CII]158 μm, [OIII]88 μm, and [OIII]52 μm, respectively.

Understanding the dependence of the intrinsic luminosity, L_i, in a given line transition i (or, equivalently, total gas cooling, Λ_i, in that transition) on various physical properties of the emitting regions is essential to grasping how physical quantities are extracted from FS line ratio observations. Consider the ground state electronic configuration of singly ionized carbon, C^{+}, which can be approximated as a two-level system (left panel of Figure 4) defined by its fine-structure. A downward electronic transition from the upper to the lower level (denoted as levels 2 and 1, respectively) results in the emission of an IR photon of wavelength 158 μm, referred to as [CII]158μm[9]. As described in, for example, Tielens (2005) and Osterbrock (1989), in the optically thin limit—i.e., in the case where emitted photons escape the "parent cloud" without scattering or absorption, which is appropriate for [CII]158μm (and many of the IR FS lines, in fact) in most astrophysical conditions—it is possible to determine the relative population of each energy level in a straightforward way by assuming that the rate of downward and upward transitions between levels is in equilibrium and proceeds exclusively via collisional excitations and de-excitations

---

[9] Square brackets indicate the transition is forbidden by electric dipole selection rules.

and spontaneous emission:

$$\underbrace{n_1 n\gamma_{12}}_{\text{upward transition}} \quad = \quad \underbrace{n_2 n\gamma_{21} + n_2 \mathrm{A}_{21}.}_{\text{downward transitions}} \tag{0.0.2}$$

In the above equation, A_{21} is the Einstein A coefficient for spontaneous emission (units of s^{-1}) and n, n_1, n_2 refer to the number densities (units of cm^{-3}) of the gas, and of carbon ions in levels 1 and 2. The coefficients γ_{12} and γ_{21} refer to the collisional excitation and de-excitation rates (units of $\mathrm{cm}^3\ \mathrm{s}^{-1}$), respectively, which depend on the quantum mechanical collision strength of an atom or ion and (weakly) on temperature. Equation 0.0.2 can be re-written as

$$\frac{n_2}{n_1} = \frac{n\gamma_{12}}{n\gamma_{21} + \mathrm{A}_{21}}. \tag{0.0.3}$$

Based on the form of Equation 0.0.3, we consider two interesting limiting cases where we can calculate the line cooling rate, given by $\Lambda_{[\mathrm{CII}]} = n_2 A_{21} h\nu_{21}$, where h is Planck's constant.

First, consider the low-density limit, where $n\gamma_{21} \ll \mathrm{A}_{21}$. If we define a critical density, $n_{crit} = \mathrm{A}_{21}/\gamma_{21}$, then this limit applies to all densities below the critical density, i.e., $n \ll n_{crit}$. Here, equation 0.0.3 simplifies to

$$\frac{n_2}{n_1} = \frac{n\gamma_{12}}{\mathrm{A}_{21}},$$

and the line cooling rate becomes

$$\Lambda_{[\mathrm{CII}]} = n n_1 \gamma_{12} h\nu_{21}, \tag{0.0.4}$$

indicating that a photon is emitted for every collisional excitation in this case.

Second, in the high-density limit, where $n\gamma_{21} \gg \mathrm{A}_{21}$ or $n \gg n_{crit}$, we have

$$\frac{n_2}{n_1} = \frac{\gamma_{12}}{\gamma_{21}}$$

and

$$\Lambda_{[\mathrm{CII}]} = n_1 \frac{\gamma_{12}}{\gamma_{21}} \mathrm{A}_{21} h\nu_{21} \tag{0.0.5}$$

Since the forms of the rate coefficients γ_{12} and γ_{21} are given explicitly as

$$\gamma_{12} = \frac{\beta\Omega_{12}}{g_1 T^{1/2}} \exp\left(-\frac{h\nu_{21}}{k_{\mathrm{B}}T}\right) \quad \text{and} \quad \gamma_{21} = \frac{\beta\Omega_{21}}{g_2 T^{1/2}}, \tag{0.0.6}$$

where $\beta = h^2/(k_{\mathrm{B}} m_e^3)^{3/2}$, m_e is the mass of the electron, k_{B} is Boltzmann's constant, T is the kinetic temperature of the gas, g_1 and g_2 are the statistical weights of each level, and Ω_{12} and Ω_{21} are quantum mechanical, dimensionless collisional strengths. Inserting the expressions for γ_{12} and γ_{21} in Equation 0.0.5, we find:

$$\Lambda_{[\mathrm{CII}]} = n_1 \frac{g_2 \Omega_{12}}{g_1 \Omega_{21}} \exp\left(-\frac{h\nu_{21}}{k_{\mathrm{B}} T}\right) \mathrm{A}_{21} h\nu_{21} \tag{0.0.7}$$

which implies that, in the high-density limit, collisional excitations/de-excitations dominate and bring carbon ions to local thermal equilibrium with the collision partners (e.g., electrons), allowing the level populations to be given by the Boltzmann distribution at the kinetic temperature T.

The dependence of Λ_i on gas density is just one example of how properties of the extragalactic ISM influence the observed emission in a given line transition. The line cooling rate also depends on many other properties of the ISM, such as the gas temperature relative to the separation between energy levels during the transition and the abundance of the emitting species, which is influenced by the metallicity of the gas, as well as the incident ionizing radiation on interstellar clouds. Thus, physical properties of the gas within galaxies can be difficult to extract from observation of individual emission lines. It is possible, however, to observe two or more emission lines in order to construct flux ratios in which various dependences on physical quantities are removed, leaving a dependence only a singly quantity to be measured. Observed flux ratios can be compared to their expected values from theory (e.g., Equations 0.0.4 and 0.0.7) in order to determine the prevalent physical properties of the ISM.

For example, the 52 μm and 88 μm transitions of doubly ionized oxygen (cf. Figure 4) are frequently used to determine the average density of ionized gas in galaxies. As they both arise from the same ion, these transitions are not dependent on the metallicity or ionization state of the gas. The fine structure levels involved in the transitions are also closely spaced in energy, so the transitions are also fairly insensitive to the gas temperature. With distinct critical densities $n_{crit} = 500$ cm^{-3} and 3,400 cm^{-3} for [OIII]88μm and [OIII]52μm, respectively, the corresponding flux ratio probes gas densities within the range defined by the different n_{crit}. When $n \ll n_{crit}$ or $n \gg n_{crit}$, the flux ratio is no longer dependent on gas density, but on the ratio of statistical weights (for $n \ll n_{crit}$) or the ratio of statistical weights times A_{21} (for $n \gg n_{crit}$), as demonstrated in Equations 0.0.4 and 0.0.7, albeit modified for a three-level system appropriate for the oxygen transitions. Figure 1.8 in Chapter 1 shows the theoretical value of the [OIII]88μm and [OIII]52μm flux ratio as a function of ionized gas density.

The left panel of Figure 3 presents a set of IR FS lines that are commonly observed to originate throughout the ISM, and which are frequently used in the construction of so-called "diagnostic" line ratios. In this figure, FS lines are plotted as functions of their ionization energies (IEs) and the densities, n_{crit}, at which they thermalize via collisions with electrons or hydrogen nuclei. This particular organization is helpful in locating pairs of emission lines that can be used to form flux ratios that probe the flux of Lyman continuum photons emitted from stellar populations and the gas density. Line ratios that are sensitive measures of gas density around star-forming regions, for example, include transitions from the same atom or ion, such as the 63 μm and 146 μm FS line transitions splitting the ground state of neutral oxygen, or the 52 μm and 88 μm transitions of the doubly ionized atom, as discussed above. These transitions have the same elemental abundances (so they are not dependent on the metallicity or ionization state of the gas) and are very closely spaced in energy (so they are not sensitive to gas temperature), but they have distinct critical densities (so their flux ratio will be highly sensitive to the gas density). The ratio of the oxygen 88 μm line to the 122 μm line of singly ionized nitrogen, which have similar critical densities but different ionization energies, is another useful ratio, probing the effective temperature of stellar populations in DSFGs (right panel of Figure 3 by gauging the impingent ionizing flux. (Examples of other line ratios and their sensitivity to physical conditions in the ISM are compiled in Appendix A.) As illustrated in lefthand panel of Figure 3, ratios of FS lines can be used to probe a wide range of astrophysical environments.

In Chapter 1—a detailed study of the multi-component ISM in an AGN with ongoing SF during the epoch of peak cosmic SF—we make use of the IR FS lines of singly ionized carbon (158 μm line transition of [CII]), neutral oxygen (63 μm transition of [OI]), singly ionized nitrogen (122 μm transition of [NII]), and doubly ionized oxygen (52 μm transition of [OIII]). Because the epoch of peak galaxy cosmic SFR density also correlates with the epoch of peak supermassive black hole accretion rate density, the target of this study, called the Cloverleaf, is a well-suited laboratory to study the evolution of galaxies.

The ability to study the FS lines in distant galaxies on an object-by-object basis is challenged by a reduction in line flux by the factor $(1 + z)^2$ due to the cosmological expansion, and so observing these lines in the Cloverleaf system at $z = 2.6$ is partly enabled by its high intrinsic bolometric luminosity—nearly 10^{14} times the luminosity of the Sun, $L_\odot$—and an additional magnification from gravitational lensing by foreground galaxies. Although galaxies with high IR luminosities called (ultra-)luminous infrared galaxies ($L_{\rm IR} \geq 10^{11}$ $L_\odot$) constitute the majority of the IR luminosity density (and thus the SFR density, as well) during the epoch of peak cosmic SF, their number density is orders of magnitude lower than fainter systems. This fact motivates the observational approach called intensity mapping, or 3-dimensional (3D) tomography, which does not rely on the detection of spectral line emission from individual sources, measuring instead the power spectrum of 3D fluctuations in line aggregate line emission over large volumes containing $\sim 10^2 - 10^3$ galaxies. Chapter 2 examines the merit of the intensity mapping technique as an additional tool for studying galaxy evolution during the epoch of peak cosmic SF by studying the feasibility of detecting the power spectrum from the 158 μm FS line transition of singly ionized carbon ([CII]158, for brevity of notation) during $0.5 \lesssim z \lesssim 2$. This chapter also introduces intensity mapping as a means of extract-ing redshift-evolution in aggregate FS line luminosity density, and compares the effectiveness of traditional galaxy surveys to measure the same quantity (as well as to measure the power spectrum).

Finally, in Chapter 3, the intensity mapping technique is considered in the context of another critical phase in galaxy evolution that coincides with a critical phase in the evolution of the Universe, namely, the Epoch of Reionization (EoR), during which the neutral hydrogen that formed when photons decoupled from baryons roughly 3.7×10^5 years after the Big Bang, and permeated the Universe, became reionized. The first galaxies, which are theorized to have formed at some $z \lesssim 50$, are currently considered to be the most likely source of the ionizing photons responsible for reionization, carving out expanding HII bubbles in the neutral hydrogen gas between galaxies called the intergalactic medium (IGM) until the Universe was fully ionized at some time between $z \sim 5.5 - 6$—about 1 Gyr after the Big Bang (Fan et al. 2006; Mortlock et al. 2011). According to observations of the galaxy luminosity function, which characterizes the comoving number density of galaxies of a given luminosity, the bulk of the galaxy population during EoR will be faint, making them difficult to detect even with the aid of magnification from strong gravitational lensing and sensitive instruments aboard the future James Webb Space Telescope observatory (e.g., Wise et al. (2014)). Because galaxies during EoR may not be as dusty as their $z \sim 1 - 3$ counterparts, the benefit of using IR FS lines to study galaxies during Reionization lies more in their applicability as diagnostics of SF and AGN than their transparency to dust. The high escape fractions of IR FS line photons from their parent clouds adds further appeal to these lines, in comparison to observations of galaxies targeting the 1216Å Lyman-α line, for example, which, as a resonance line, has a high cross-section for scattering with neutral hydrogen. Ultimately, the potential of EoR intensity mapping experiments to probe changes in the ISM of large populations of galaxies (that may otherwise be undetected) over cosmic timescales is a promising opportunity that warrants further study.

Chapter 1

Constraining ISM properties of the Cloverleaf Quasar with *Herschel* spectroscopy

1.1 Introduction

Parallel histories of cosmic star formation (SF) and supermassive black hole (SMBH) accretion are suggestive of a causal relationship between the two processes, yet the nature of this link remains an open question in astrophysics. At the root of this connection is the cold molecular gas in galaxies, which must be shared as fuel for both growing black holes and budding stellar nurseries. Far from simple competitors, however, the roles of SF and SMBH growth in a galaxy's evolution are varied and complex.(See, e.g., reviews on the subject by Heckman & Best (2014) and Madau & Dickinson (2014)). Molecular, star-forming gas in the circumnuclear region of galaxies known to host accreting SMBHs (called Active Galactic Nuclei, or AGN) are particularly useful test-beds for theories relating the feedback of the SMBH on SF (and vice versa) given the relatively short distances (~ 1 kpc) between the molecular gas and the SMBH.

The $z = 2.56$ Cloverleaf quasar and its host galaxy have emerged as a case study for co-extant SF and SMBH accretion during the epoch of peak galaxy assembly. Although the Cloverleaf was initially discovered in an optical survey of luminous quasars (Hazard et al. 1984), follow-up observations (Barvainis et al. 1992) of the sub-millimeter (submm) continuum revealed a slight excess in the rest-frame far-infrared (FIR) portion of its spectral energy distribution (SED) that was consistent in spectral shape with thermal emission from dust. This fact and the knowledge that the quasar is strongly gravitationally lensed (Magain et al. 1988), combined with the advent of high-z CO measurements (Brown & Vanden Bout 1991), rendered the Cloverleaf a prime target for CO line searches. The detection of CO($J = 3 \rightarrow 2$) in the system (Barvainis et al. 1994) effectively launched the Cloverleaf into the early

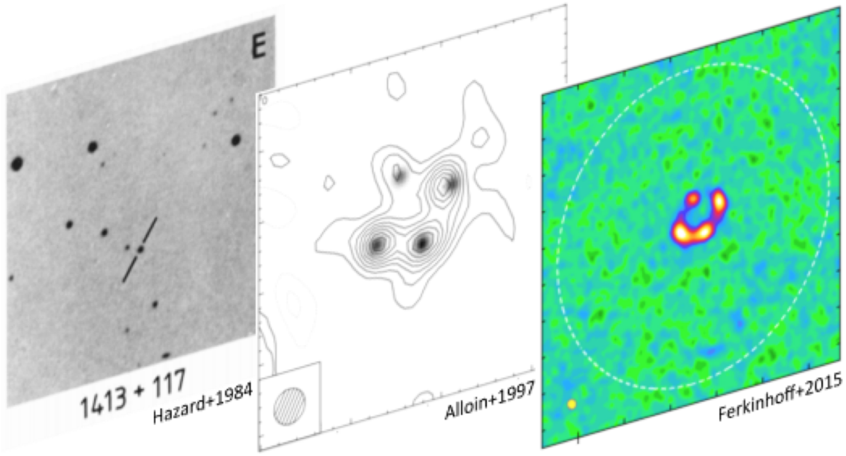

Figure 1.1

Figure 1.2: The Cloverleaf quasar imaged in three wavelengths. From left to right: optical (Hazard et al. 1984), millimeter (Alloin et al. 1997), far-infrared (Ferkinhoff et al. 2015).

stages of its longstanding role as a laboratory for high-z studies of molecular gas and SF in the environs of a powerful AGN. Since the first successful CO measurement, the Cloverleaf has been observed, to date, in numerous tracers of molecular gas, including 8 transitions of the CO ladder ($J = 1 \rightarrow 0$ (Riechers et al. 2011a), $3 \rightarrow 2$ (Barvainis et al. 1997; Weiß et al. 2003), $4 \rightarrow 3$, $5 \rightarrow 4$ (Barvainis et al. 1997), $6 \rightarrow 5$ (Bradford et al. 2009a, hereafter B09), $7 \rightarrow 6$ (Alloin et al. 1997; Barvainis et al. 1997, B09), $8 \rightarrow 7$, and $9 \rightarrow 8$ (B09)), two fine-structure (FS) transitions of [CI] ($^3P_1 \rightarrow ^3P_0$ (Weiß et al. 2005) and $^3P_2 \rightarrow ^3P_1$ (Weiß et al. 2003)), HCN ($J = 1 - 0$)(Solomon et al. 2003), and HCO$^+$ ($J = 1 \rightarrow 0$ (Riechers et al. 2006) and $4 - 3$ (Riechers et al. 2011b)), and CN (Riechers et al. 2007). Spatial extent of the molecular gas, derived from a CO($J = 7 \rightarrow 6$) map, has also been assessed, and appears to be concentrated in a disk of radius 650 pc, centered on the SMBH (Venturini & Solomon 2003, VS03). Non-LTE modeling of CO excitation with an escape probability formalism suggests that all observed transitions can be described by a single gas component (Bradford et al. 2009a; Riechers et al. 2011a), so there is no indication of significant molecular emission in the observed lines beyond the CO($J = 7 \rightarrow 6$) disk. Physical conditions inferred from the modeling point to molecular gas densities of roughly $n_{\mathrm{H}_2} = 2\text{–}3\times10^4$ cm^{-3} and high gas kinetic temperatures of 50–60 K, suggesting that the CO gas is distributed uniformly or with high areal filling factors—not in sparse clumps—in order to maintain this thermal state throughout the ~ 1 kpc-wide emitting region.

In addition to molecular spectroscopy, (sub)mm continuum measurements have provided further insight into the nature of SF in the Cloverleaf ISM. In the rest-frame IR SED compiled by Weiß et al. (2003), the Cloverleaf's continuum emission appears double-peaked, with distinct cold and warm gas components with dust temperatures of $\sim$ 50 K and $\sim$ 115 K, respectively. The starburst origin of the cold gas component is strongly supported by the detection of emission features from polycyclic aromatic hydrocarbons (PAHs) in the Cloverleaf's rest-frame mid-infrared spectrum, which were shown to follow the empirical correlation to FIR luminosity established for starbursts and composite quasar/starburst systems in the local Universe (Lutz et al. 2007). Attributing, then, the entirety of the FIR (42.5–122.5μm) luminosity, $L_{\rm FIR}$, inferred from the cold component of the SED, reveals a starburst of intrinsic $L_{\rm FIR} = 5.4 \times 10^{12}$ $L_\odot$.

Identifying the dominant heating source of the molecular gas in the Cloverleaf is essential to understanding the relationship between the SMBH and SF in the host galaxy. In this paper, we present new measurements of key diagnostic lines of atomic and ionized media to aid in the interpretation of the excitation mechanisms for the observed CO in the Cloverleaf disk. The detected lines, namely [CII]158μm, [OI]63μm, [OIII]52μm, and [SiII]35μm, provide highly complementary information to the CO spectroscopy by tracing star-forming gas in different phases of the ISM, and by providing additional means to test XDR and PDR models, which can predict bright emission in the observed atomic lines.

This article is organized as follows. First, we report in Section 1.2 the measured line fluxes from *Herschel*-SPIRE and -PACS instruments, and discuss uncertainties where necessary. With observations of the important PDR cooling lines [CII]158μm and [OI]63μm enabled by *Herschel*, we are able to infer the average densities and FUV fluxes prevalent in the Cloverleaf PDRs by employing traditional FS line ratio diagnostics, as well as to better estimate the relative contribution of the AGN and SF to producing the observed emission, which we explore in Section 1.3. There, after subtracting contributions from ionized gas in the Narrow Line Region (NLR) and HII regions, we compare measured line ratios of the FS lines and CO to predicted values from PDR and XDR models and determine their respective contributions to the observed emission. We also briefly consider shock excitation of CO as an alternative explanation for the unusual high total CO line-to-FIR continuum ratio. Finally, in Section 1.4, we place our findings for the Cloverleaf in the context of other AGN discovered at similar and lower redshifts.

1.2 Observations

Measured fluxes for the fine-structure lines obtained in this work are presented in Table 1. We supplement our measurements with published fluxes for the [NII]122μm emission, CO up to J = 1–9, and the 6.2 μm and 7.7 μm PAH emission features.

SPIRE FTS At z = 2.56—the CO redshift of this source—fine-structure line emission from [CII]158μm and [OI]63μm is redshifted to within coverage of the long wavelength (LW, 303–671 μm) and short wavelength (SW, 194–313 μm) bands of the SPIRE Fourier Transform Spectrometer (SPIRE FTS) aboard *Herschel*. Point source spectra were obtained in sparse observing mode for the Cloverleaf with a total of 320 FTS scans—160 in each forward and reverse directions—from the *Herschel* OT program `OT1_mbradfor_1` (PI: Matt Bradford). Amounting to 364.4 minutes of observing time for the source, these spectra are the deepest SPIRE spectra yet presented, to our knowledge. The continuum level is at 0.1–0.5 Jy, which is close to the continuum flux accuracy achieved on SPIRE. As such, we take care to address concerns about spurious line detections arising from random noise fluctuations in the continuum, and—once lines have been identified—to accurately quantify uncertainties in the measured line fluxes.

To reduce the probability of a spurious line detection, we perform a jackknife test for each targeted line in which the full set of 320 unapodized spectra obtained from corresponding FTS scans is first split into two subsets. The jackknife split we apply is temporal, in order to test for variations in the spectrum as a function of observing time; we simply divide the scan set into halves containing scans 1–160 and 161–320, where scan 1 denotes the beginning of the observation and 320, the end. The 160 spectra in each half are then co-added to produce two separate spectra (called A and B), and then differenced to produce a residual spectrum. In the absence of systematic error between sets A and B, the differenced spectrum will contain zero flux at all wavelengths. Figure 1.3 shows the results of the jackknife tests for the [CII]158μm, [OI]μm63, and [OIII]88μm lines in 50 GHz[1] segments centered at the rest wavelength for each line.

Line fluxes were measured from the unapodized spectrum using the SpectrumFitter in *Herschel* Interactive Processing Environment (HIPE) 12 version 1.0 (Ott 2010). We fit each emission line and 6 GHz of local continuum with a 1st order polynomial baseline and a Gaussian line profile convolved with a sinc function (i.e., "SincGauss" model in HIPE). Line centers, $(1 + z_{\rm Clover})\lambda_{\rm rest}$ were fixed, as were the widths of the Gaussian and sinc profiles. The assumed Gaussian widths are not crucial to the fit—we adopted a FWHM of 500 km/s, on the upper range of that measured by Weiß et al. (2003) in the CO lines with the Plateau de Bure interferometer. For the sinc function, we fixed the width at 0.38 GHz, which is set by the spectral resolution of the FTS (in high resolution mode). The SpectrumFitter returns the fitted parameters for the SincGauss model, which we convert to flux using the appropriate analytic formula. It also provides an associated uncertainty, which we consider as a lower limit. We proceed to generate our own estimate of the RMS noise in 50 GHz of bandwidth centered at the target frequency. In our estimate, we repeatedly fit our SincGauss model at various frequencies within this bandwidth. Because the SPIRE FTS has a spectral resolution of 1.2 GHz, there are 41 independently sampled frequencies—and thus 41 independent line flux fits—in each 50 GHz range. The uncertainty reported in Table 1.1 is the standard deviation (equal to the RMS for the zero-mean signal) of the sampled frequencies, plus a 5%

---

[1] Bandwidths are calculated in observed (vs. rest) frequency units.

calibration uncertainty for SPIRE. A histogram of the flux fits using our uncertainty estimate is displayed in the righthand panels of Figure 1.3. Note that the histograms are centered at zero, as expected for random noise. For reference, the measured flux of the target line is also shown (dashed vertical line) in the histogram plot, and is given in Table 1.1. The lines [CII]158μm and [OI]63μm are detected at levels of 3.8σ and 8.5σ, respectively. A 2σ upper limit is reported for [OIII]88μm.

PACS Point-source observations of the Cloverleaf include spectra from the blue and red channels, which cover the wavelength range corresponding to expected FS line emission from [OIII]52μm, [SiII]35μm, [SIII]33μm, [FeII]26μm, and [OIV]26μm. Spectra for [OIII]52μm and [SiII]35μm were obtained from the `OT1_mbradfor_1` observing program; [OIII]52μm, [SIII]33μm, [FeII]26μm, and [OIV]26μm spectra were obtained from the Key Program `KPGT_kmeisenh_1` (PI: Klaus Meisenheimer). The two spectra containing the [OIII]52μm line were co-added using the AverageSpectra task in HIPE. The data were reduced with the background normalization version of the chopped line scan reduction script included in HIPE. We reduced the data with $oversample = 4$, then binned by a factor of 2 in post-processing to achieve Nyquist sampling. Processed spectra with error bars and line fits (blue curves) for the targeted lines are presented in Figure 1.4. Measured fluxes and uncertainties (obtained directly from SpectrumFitter) are listed in Table 1.1. While we only report detections for [OIII]52μm (5.1σ) and [SiII]μm (7.8σ), an upper limit for [OIV]26μm is also given, and we include spectra of the other lines (namely, [FeII]26μm and [SIII]33μm) for completeness.

1.2.1 Extinction corrections

While the far-IR lines are relatively extinction-free, corrections are required for the most highly-obscured systems. In Arp 220, for example, Rangwala et al. (2011) find that the dust is optically thick at 240μm, corresponding to a column density in hydrogen, $N_{\rm H}$, of $10^{25}\,{\rm cm}^{-2}$. This extreme source demands corrections even for the submillimeter mid-J CO transitions.

The Cloverleaf has similar gas and dust masses to Arp 220, but the extinction is reduced because the size scale is larger. We estimate extinction values using both gas and dust mass, in both cases spread over the 650-pc radius disk (including the 30° inclination), with an area of $1.1\times10^{43}\,{\rm cm}^2$. For the gas mass, we take the peak of the B09 molecular gas mass likelihood of $6 \times 10^9\,{\rm M}_\odot$, which corresponds to a typical hydrogen column in the disk of $4.7 \times 10^{23}\,{\rm cm}^{-2}$. Per the mixed-dust model of Li & Draine (2001), this column creates 0.8 magnitudes of extinction at 63μm, corresponding to an optical depth, τ, of 0.73; and, the model predicts a ν^{-2} scaling with τ for wavelengths between 30μm and 1000m. A similar estimate is obtained with the estimated dust mass from Weiß et al. (2003), some $6.1 \times 10^7\,{\rm M}_\odot$. When distributed in the disk, this gives a mass column of $1.1 \times 10^{-2}\,{\rm g\,cm}^{-2}$. The

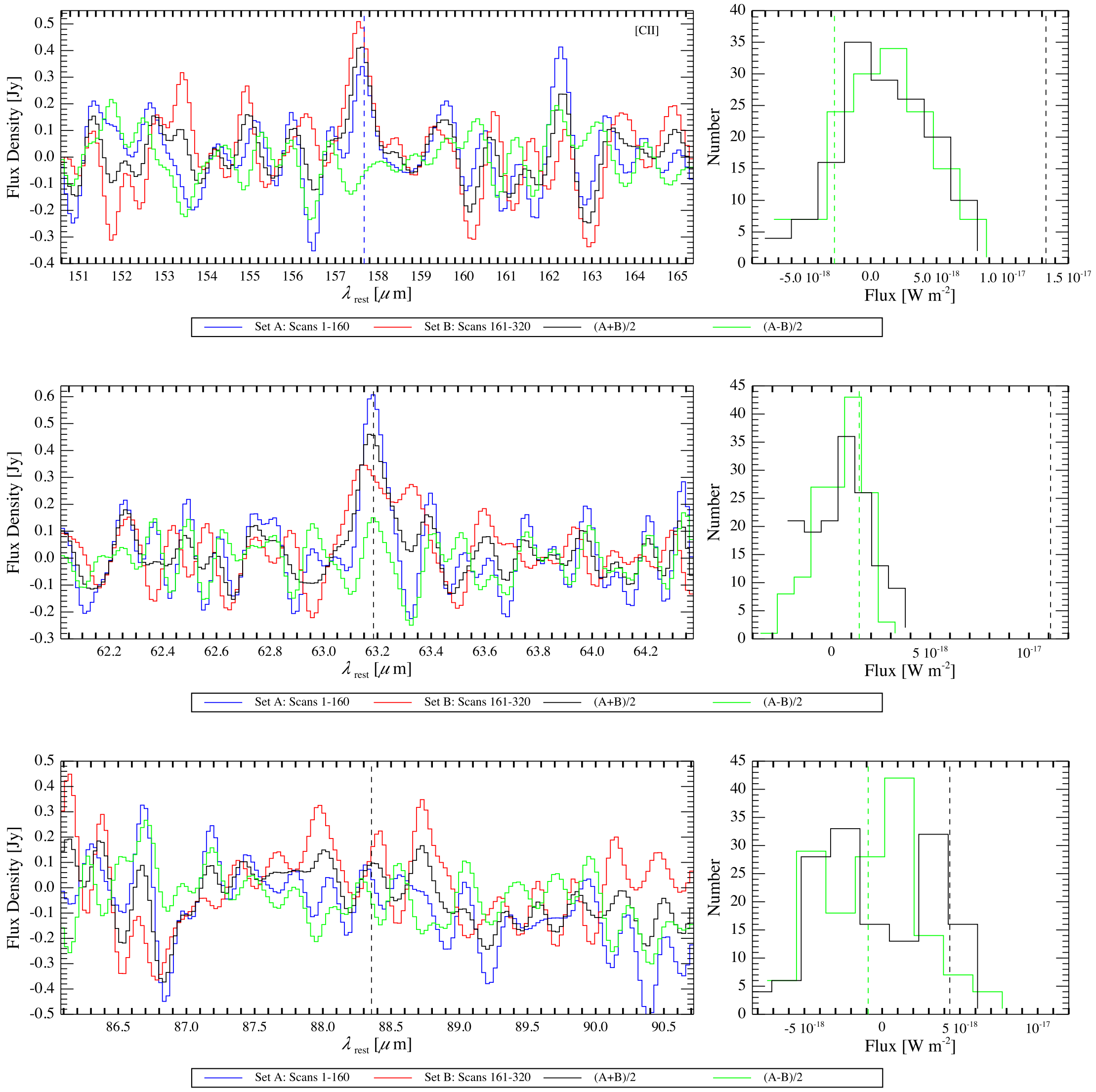

Figure 1.3: SPIRE FTS spectra for [CII]158μm, [OI]63μm, and [OIII]88μm (top to bottom panels). Each spectrum shown here spans a 50 GHz range centered at the rest wavelength for the target line. Blue and red curves denote spectra from the first half of scans (i.e., scan numbers 1 through 160) and second half of scans (scan numbers 161 through 320) in the dataset, while black and green curves correspond to the coadded and jackknifed data. Histograms at right show the flux returned by the line fit applied to each frequency position in the 50 GHz range, while avoiding the surrounding 2×FWHM line widths on each side of the target line center. Dashed vertical lines denote the fitted flux at the target line center for the coadded spectrum and the jackknifed spectrum.

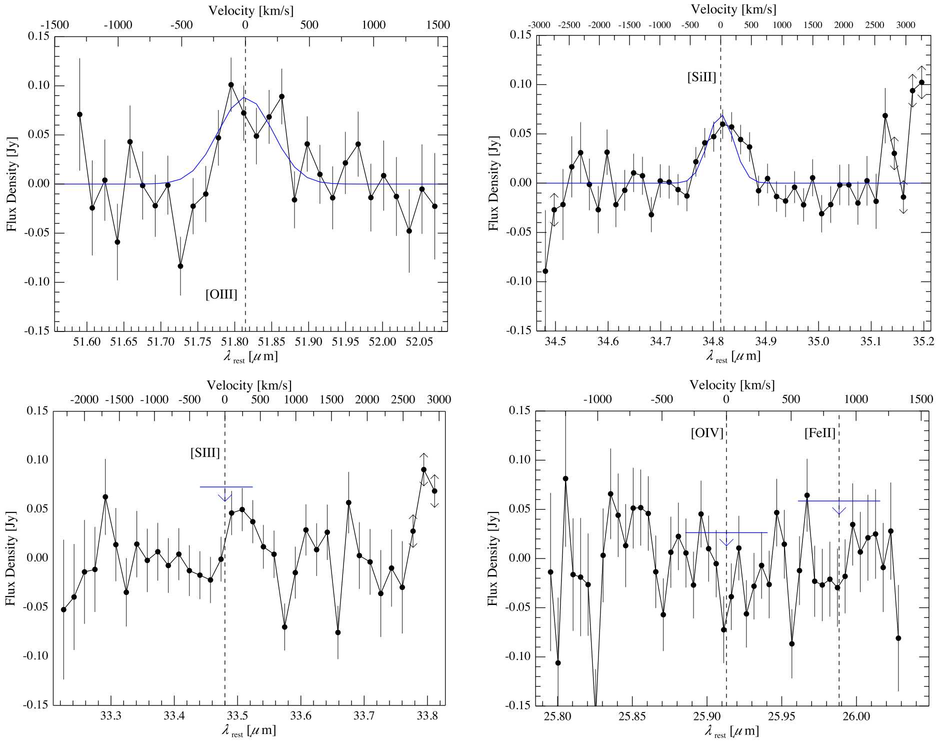

Figure 1.4: Resampled continuum-subtracted PACS spectra with error bars for [OIII]52μm, [SIII]33μm, [SiII]35μm, and [OIV]26μm and [FeII]26μm. Gaussian fits (FWHM = 500 km/s, fixed width) for spectral lines are shown as blue curves. Horizontal blue lines with downward-pointing arrows indicate a 2σ upper limit on the line flux density.

absorption coefficient in Table 6 of Li & Draine (2001)—adjusted to 63 microns—gives $\kappa_{63} = 84.7\,\mathrm{cm}^2\mathrm{g}^{-1}$, and an optical depth of 0.93. We adopt the average of these values ($\tau_{63} = 0.83$), and use a mixed dust extinction model in which the correction factor relating observed to intrinsic flux is $\tau_d/(1 - e^{-\tau_d})$. The mixed-dust model is appropriate if the emission lines originate in gas mixed approximately uniformly with the disk, as is the basic scenario for the star-forming disk material. For emission from the AGN narrow-line region (NLR), the correction could potentially be greater if the NLR gas is fully covered by the disk. On the other hand, at least some portion of the NLR material is largely unobscured, since NLR gas is visible at optical wavelengths. Given these uncertainties, the modest correction of the mixed dust model seems appropriate. The correction factor for [OI]63 is 1.47, and the other transitions are corrected similarly assuming $\tau \propto \nu^{-2}$. Line fluxes reddened according the necessary correction factors are listed in Table 1.1.

1.3 Analysis

In this section, we use the suite of CO rotational transitions (from the literature), the [NII]122μm line (Ferkinhoff et al. 2011a, F11), and the newly detected ($> 3.5\sigma$) atomic FS lines (from this work) in diagnosing the physical conditions prevalent in the ISM of the Cloverleaf system.

Although the dataset of detected lines is rich, the natural complexities of a multiphase ISM must be treated carefully, particularly given that many of the observed transitions can be excited in a variety of physical environments: photon-dominated regions (PDRs), dense stellar HII regions, diffuse ionized gas, the clouds of the NLR near the AGN, or X-ray Dominated Regions (XDRs); see Figure 1.5 for a cartoon representation of the various ISM phases and the corresponding emission lines expected from each phase. High resolution spatio-spectral imaging data for the set of observed emission lines is limited, but is helpful in partitioning ISM components when available, as in the case of CO($J = 7 \rightarrow 6$) and [NII]122μm. The FS line observations presented here are all spatially unresolved; the smallest beam sizes for *Herschel*-SPIRE and -PACS imaging spectrometers are 17” and 9”,

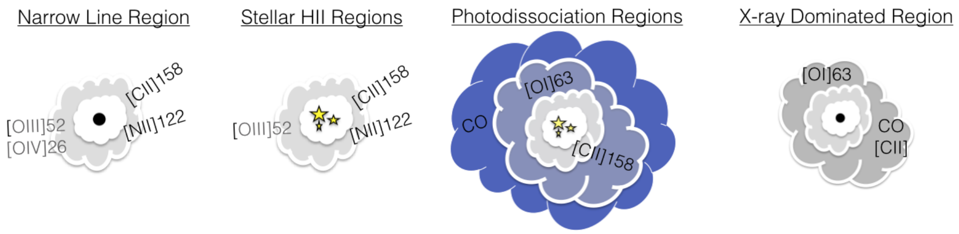

Figure 1.5: The multiple phases of the Cloverleaf ISM. Cartoons depict sources of radiation at the cloud center as a black circle to indicate an accreting BH or a cluster of stars to indicate stellar radiation. Expected emission lines are labeled in each cartoon.

respectively, compared to the on-sky diameter of 2" for the optical quasar and the interferometric CO($J = 7 \rightarrow 6$) image. We are therefore considering integrated emission from the composite source and begin by considering how the atomic line emission is partitioned among the various components.

1.3.1 [CII]158μm from non-star-forming gas

The optically thin [CII]158μm emission can be used to assess the mass of [CII]158μm-emitting atomic gas, $M_{\rm H}$, by comparing the measured [CII]158μm luminosity, $L_{\rm [CII]}$, to the expected C$^+$ cooling rate (units of erg s^{-1} per H atom). Following Hailey-Dunsheath et al. (2010b) (cf. their Equation 1), and using the PDR surface temperature $T_{\rm PDR} \sim 300$ K and density $n_{\rm H} = 3.16 \times 10^3$ cm^{-3}—see Section 1.3.2 for justification of $T_{\rm PDR}$ and $n_{\rm H}$ adopted here—we find $M_{\rm H} \sim 2 \times 10^{10}$ M$_\odot$. This value is on the high end of the Cloverleaf's molecular gas mass estimated by B09 ($M_{\rm H_2} \sim$ 0.3–3$\times 10^{10}$ M$_\odot$), indicating that the mass in PDRs comprises a substantial fraction of the total gas mass in the ISM.

With a first ionization energy (IE = 11.26 eV) lying just below 1 Rydberg, singly-ionized carbon can coexist with both neutral and ionized hydrogen. Thus, while we expect that PDRs illuminated by star-formation may be the dominant source of [CII]158μm emission, we must consider stellar HII regions (denoted in symbols with subscripts as "HII*" throughout this article) and the AGN-ionized NLR, as well. The sum of each ISM phase's contribution—expressed as the fraction, $\alpha_{{\rm [CII]},j}$, of observed flux for [CII]158μm (or generally any line i) and ISM phase j—will sum to the measured total line flux, $F_{\rm [CII]}$, so that the flux attributed to PDRs, $F_{\rm [CII],PDR}$, is written as

$$F_{\rm [CII],PDR} = (1 - \alpha_{\rm [CII],NLR} - \alpha_{\rm [CII],HII^\star}) \times F_{\rm [CII]} \qquad (1.3.1)$$

We note that F11 measured the total [NII]122μm luminosity, $L_{\rm [NII]122}$, in the Cloverleaf, and placed a lower limit on the mass of ionized gas, $M_{\rm H^+} \sim 2.1 \times 10^9$ M$_\odot$, by calculating the N$^+$ cooling rate for high ionized gas densities ($n_{\rm H^+} \gg n_{crit,{\rm e^-}}$) and temperatures at which all nitrogen exists in the singly-ionized state. Working in the same high-density, high-temperature limit, we estimate the minimum expected luminosity of [CII]158μm from their inferred ionized gas mass as $\sim 2 \times 10^9$ L$_\odot$, or, roughly $\gtrsim 10\%$ of $L_{\rm [CII]}$.

Narrow Line Region As the AGN is responsible for roughly 90% of the Cloverleaf's bolometric luminosity, we first consider the potential for [CII]158μm emission arising in the NLR associated with the immediate vicinity (of the order 10–100 pc) of the central accretion zone.

Recent Band 9 observations with ALMA (Ferkinhoff et al. 2015, F15) provide an upper limit to the contribution of the Cloverleaf NLR to the measured [NII]122μm line flux, namely, $\alpha_{\rm [NII]122,NLR} \leq 0.2$. As the authors there explain, the [NII]122μm flux detected by ALMA is only 20% of the flux previously measured with a single dish in F11, and is coincident with the quasar point source. Since the line is spatially unresolved with a synthesized beam size of ~ 0.25" (or ~ 180 pc in the source plane), they concluded that the detected emission can be ascribed to the NLR, while the undetected flux originates from a more extended area and has thus been "resolved out" by the small ALMA beam. We use this upper limit to estimate, based on theoretical models, the corresponding [CII]158μm emission for given physical conditions prevalent in the NLR by writing

$$\alpha_{\text{[CII],NLR}} = \frac{\gamma^{\text{(G04)}}_{\text{[CII],NLR}} \times F_{\text{[NII]122,NLR}}}{F_{\text{[CII]}}} \tag{1.3.2}$$

where $F_{\text{[NII]122,NLR}}$ ($= 0.2F_{\text{[NII]122}}$) is the observed NLR flux of the [NII]122μm line based on the ALMA observation. The factor $\gamma^{\text{(G04)}}_{\text{[CII],NLR}}$ is, explicitly, written as

$$\gamma^{\text{(G04)}}_{\text{[CII],NLR}} = \frac{F^{\text{(G04)}}_{\text{[CII],NLR}}}{F^{\text{(G04)}}_{\text{[NII]122,NLR}}},$$

representing the scaling between the predicted fluxes of [CII]158μm and [NII]122μm—$F^{\text{(G04)}}_{\text{[CII],NLR}}$ and $F^{\text{(G04)}}_{\text{[NII]122,NLR}}$, respectively—from a NLR theoretical model, namely, that of Groves et al. (2004, G04). We correct carbon and nitrogen abundances from solar values of adopted in G04 to match ISM values that we later use when considering the stellar HII region contribution to [CII]158μm; the ISM abundance set adopts a nitrogen abundance that is a factor of 1.3 greater than specified by the solar abundance set in G04.

Output of the G04 NLR models can be parametrized on grids of n_{H} and a dimensionless ionization parameter, $U = (\Phi_{\text{LyC}})/(n_{\text{H}}c)$, where Φ_{LyC} is the rate of Lyman continuum photons per unit area from the AGN incident on the cloud surface, and c is the speed of light. According to these grids, $\gamma^{\text{(G04)}}_{\text{[CII],NLR}}$ is relatively insensitive to U and n_{H}, so that $\gamma^{\text{(G04)}}_{\text{[CII],NLR}} = 4.6$–$7.7$ throughout the parameter space for models with intrinsic power-law ionizing continua with spectral indices of -1.7 or -2.0. Adopting this range of $\gamma_{\text{[CII],NLR}}$, we place an upper bound on the fraction of flux of [CII]158μm emerging from the NLR as $\alpha_{\text{[CII]158,NLR}} \leq 0.15$–$0.25$.

1.3.2 Star-forming ISM: PDRs and stellar HII regions

PDR diagnostics Photon dominated regions (PDRs) are broadly defined as regions of the neutral ISM where photons with energies, E_γ, in the far-ultraviolet regime (6 eV $< E_\gamma <$ 13.6 eV) are responsible for driving the local chemical and physical processes that simultaneously determine ion populations and thermal balance. The chemical structure of PDRs, depicted schematically in Figure 1.6, depends on a variety of factors, such as the level of dust attenuation in the cloud, the surrounding FUV radiation field strength, and the cloud density. For a model PDR

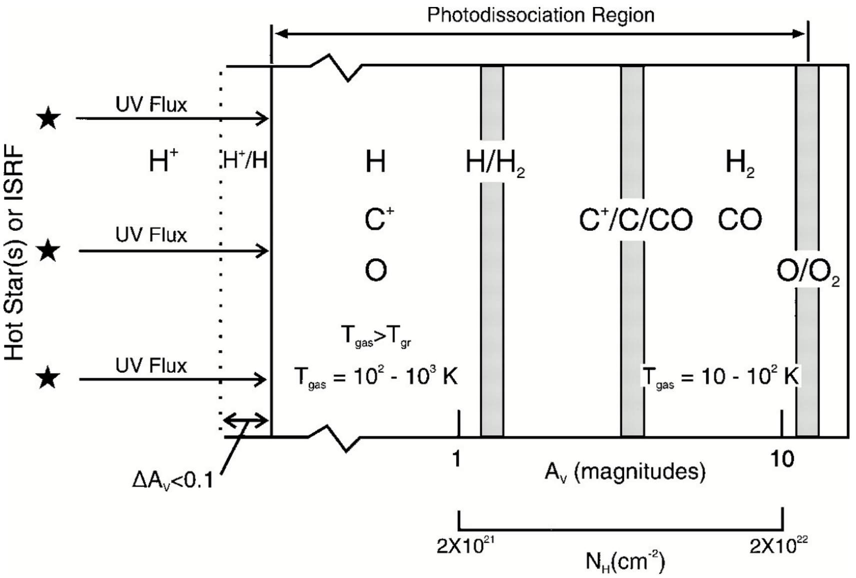

Figure 1.6: Schematic of PDR structure. Figure from Hollenbach & Tielens (1997).

represented as a uniform density slab, the warm surface layers ($A_V \leq 1-4$) are composed primarily of hydrogen and oxygen in their atomic forms, and singly ionized carbon. [CII] and [OI]63 emission primarily originate from this zone. Beyond $A_V \simeq 4$, which is a couple of magnitudes of visual extinction past the transition from atomic to molecular hydrogen, neutral oxygen persists, but carbon is no longer ionized. Instead, carbon recombines to form CO, and CO cooling dominates at these cloud depths.

Plane-parallel, semi-infinite slab models (e.g., Kaufman et al. (2006); K06) developed exclusively for PDRs can determine cloud structure and predict the emergent intensity of both lines and continuum emission by internally solving radiative transfer and thermal and chemical balance of the cloud with two parameters: incident FUV flux, G_0[2], and cloud density, $n_{\rm H} = n_{\rm H^0} + n_{\rm H_2}$. The freedom to tune G_0 and $n_{\rm H}$ over a wide range of values is an appealing feature of these models, permitting them to describe emission from a correspondingly wide range of physical conditions, and thus extending PDR predictions beyond the interpretation of photodissociation regions as existing exclusively between HII regions and molecular clouds.

The [OI]63 and [CII] lines are theoretically and empirically the dominant cooling lines in PDRs. The [OI]63 line lies much higher above the ground state than the [CII] line—228 K vs 92 K—and has a much higher critical density—3×10^5 cm^{-3} vs 3×10^3 cm^{-3}. Hence, [OI]63 emission is favored when the impinging FUV radiation (and thus gas temperature) and gas density are both high, and the flux ratio of these lines is a useful diagnostic of incident FUV flux and density. With disparate

---

[2] G_0 is normalized to the average value in the plane of the Milky Way, such that $G_0 = 1$ indicates an FUV flux of 1.6×10^{-3} erg s^{-1} cm^{-2}.

critical densities and energies above ground, their flux ratio $\frac{F_{\text{[OI]63}}}{F_{\text{[CII]}}}$ is a useful probe of the gas density and average FUV field. Similarly, $\frac{F_{\text{[CII]}}+F_{\text{[OI]63}}}{F_{\text{FIR}}}$ is another diagnostic ratio of PDR density and the impingent FUV radiation field, as this ratio of flux from from cooling lines relative to thermal dust emission essentially represents the photoelectric heating efficiency of the dust grains, which is determined by G_0/n_{H}. In this way, [CII] and [OI]63, along with the FIR continuum, have been used extensively as probes of the physical conditions in PDRs, often being presented in so-called "PDR diagnostic diagrams," wherein the observed values of line ratios are plotted as functions of G_0 and n_{H}.

To understand the star-forming ISM, we begin by incorporating the [CII]158μm and [OI]63μm fluxes, as well as the far-IR continuum, in the commonly-used framework of the PDR diagnostic diagram in Figure A.13. Here we assume that all of the measured FIR luminosity is generated from the starburst component in Cloverleaf, with negligible contamination from the AGN, as discussed in Lutz et al. (2007). According to Figure A.13, PDR models with $n_{\text{H}} \sim 2$–6×10^3 cm^{-3} and $G_0 \sim 3$–7×10^2 can generate line ratios that are compatible with observations when assuming $F_{i,\text{PDR}} = F_i$; the parameters $n_{\text{H}} = 3.16 \times 10^3$ cm^{-3} and $G_0 = 3.16 \times 10^2$ correspond to the PDR model with the lowest value of the χ^2 statistic. Note that we have not yet made any allowances for a possible contribution of observed [CII]158μm and [OI]63μm emission from ISM components distinct from PDRs. The only adjustment has been to double the measured [OI]63μm flux, as per Kaufman et al. (1999), before comparing measurements to theoretical predictions from K06. This correction is necessary because, while the intensities computed for the PDR models emerge from a single, illuminated face, the geometry of emitting regions in Cloverleaf is assumed to be such that individual PDRs are illuminated by FUV photons on all sides; optically thick [OI]63μm line emission emerging from cloud surfaces opposite the observer will not contribute to the measured flux.

Stellar HII regions We can constrain $\alpha_{\text{[CII]},\text{HII}^\star}$ in Equation 1.3.1 using the [NII]122μm flux measured in F11. With similar ionization potentials, singly-ionized nitrogen is often found in the same ionized gas as singly ionized carbon. Its slightly higher first ionization energy (IE = 14.5 eV), however, prevents the nitrogen ions from forming in neutral gas. Thus, identifying an excess in the measured flux ratio, $F_{\text{[CII]}}/F_{\text{[NII]122}}$, relative to a theoretical value predicted for exclusively ionized gas, indicates the presence of additional [CII]-emitting components, such as PDRs. While the lower-level transition corresponding to the [NII]205μm line is better-suited to assess the fraction of [CII]158μm arising in ionized gas because $F_{\text{[CII]}}/F_{\text{[NII]205}}$ is density-independent, the [NII]122μm line can be used, as well. To recover the utility of the carbon-to-nitrogen flux ratio, we model its density-dependence with the

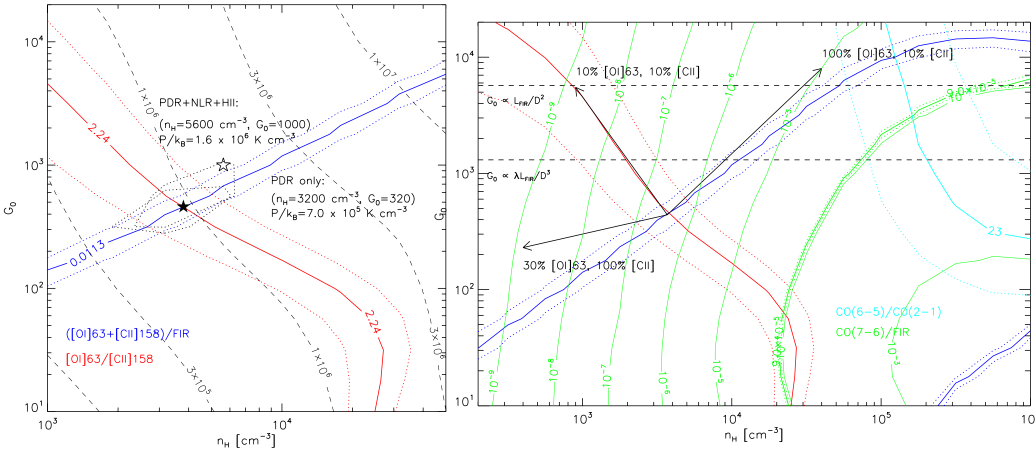

Figure 1.7: PDR diagnostic plots. Left panel: Red and blue curves denote observed values (solid) and associated uncertainties (dotted) of flux ratios $F_{\rm [OI]}/F_{\rm [CII]}$ and $\left(F_{\rm [OI]} + F_{\rm [CII]}\right)/F_{\rm FIR}$, respectively. The filled black star symbol indicates the corresponding PDR solution in $n_{\rm H}$ and G_0, which refers to the PDR model with minimum χ^2. The un-filled star represents the PDR solution with $F_{\rm [CII],PDR} = 0.6F_{\rm [CII]}$, i.e., after applying corrections for NLR and HII region contributions to the measured [CII]158μm flux. The confidence region within one standard deviation from each PDR solution is outlined by black dotted contours. Black dashed contours represent thermal pressure at the PDR surface. Right panel: Observed CO line flux ratios are shown along with the FS line ratios. The cyan curve shows $F_{{\rm CO}(J=7\rightarrow6)}/F_{{\rm CO}(J=2\rightarrow1)}$. Thick and thin magenta curves correspond to the observed and theoretical values, respectively, of $F_{{\rm CO}(J=7\rightarrow6)}/F_{\rm FIR}$. Vectors indicate the direction and magnitude of change in the PDR solution located at $n_{\rm H} = 3,160$ cm^{-3} and $G_0 = 316$, when altering the PDR contribution to [OI]63μm and [CII]158μm flux. Percentages indicated by each vector refer to the percent of the FS lines originating from the PDR.

photo-ionization code *Cloudy*[3] (Ferland et al. 1998, version 10.0); the theoretical ratio, $F^{(Cloudy)}_{\rm [CII],HII^{\star}}/F^{(Cloudy)}_{\rm [NII]122,HII^{\star}}$, is shown in Figure 1.8 as functions of U and $n_{\rm H^+}$. It is clear that the contribution of [CII]158μm from ionized gas can be large for low densities ($n_{\rm H^+} < 10$ cm^{-3}) and low ionization parameters ($U \sim 10^{-4}$). Note that the common ionized gas density probe, the [OIII]88μm-to-[OIII]52μm flux ratio $F^{(Cloudy)}_{\rm [OIII]88,HII^{\star}}/F^{(Cloudy)}_{\rm [OIII]52,HII^{\star}}$, is predicted to be less than 1.8 for all considered densities, 1 cm^{-3}< $n_{\rm H^+} < 10^4$ cm^{-3}. This value is below the ratio (< 2.3) derived from the upper limit on $F_{\rm [OIII]88}$ and the detection of $F_{\rm [OIII]52}$, so we must use an alternative means of estimating an average gas density in the Cloverleaf's stellar HII regions. If we assume that the HII regions are physically adjoined to PDRs, then we can impose thermal pressure equilibrium at the boundary between the two ISM phases, and rule out $n_{\rm H^+} \lesssim 10$ cm^{-3}, since these diffuse HII regions have thermal pressures, $P_{th}/k_{\rm B}$, in the range of $\sim 10^4$–10^5 K cm^{-3}, as calculated internally by *Cloudy*; such

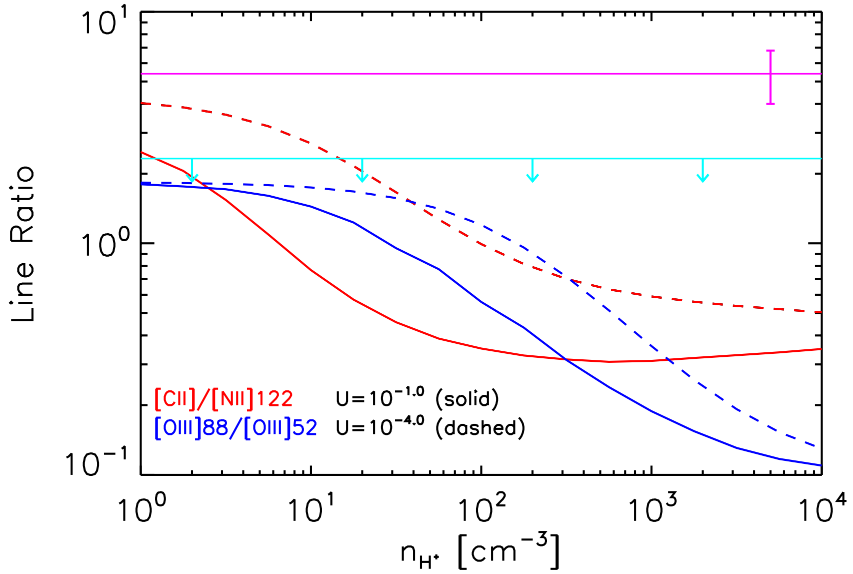

Figure 1.8: Theoretical line flux ratios $F^{(Cloudy)}_{\rm [CII],HII^{\star}}/F^{(Cloudy)}_{\rm [NII]122,HII^{\star}}$ and $F^{(Cloudy)}_{\rm [OIII]88,HII^{\star}}/F^{(Cloudy)}_{\rm [OIII]52,HII^{\star}}$ (red and blue curves, respectively) as a function of ionized gas density and computed for different ionization parameters ($U = -4.0$, dashed curves; $U = -1.0$, solid curves), computed for the HII region only. Magenta and cyan horizontal lines denote the measured value and upper limit of the respective ratios in the Cloverleaf. Measured fluxes of [CII]158μm and [NII]122μm have been corrected for NLR contributions according to $\alpha_{\rm [CII],NLR} \leq 0.2$ and $\alpha_{\rm [NII]122,NLR} \leq 0.2$, as discussed in Section 1.3.1. Error bar indicates the range of uncertainty in the ratio after propagating uncertainties on the [CII]158μm and [NII]122μm fluxes. Downward pointing arrows indicate that the [OIII]88μm/[OIII]52μm ratio represents an upper limit, having used the 2σ upper limit reported for [OIII]88μm.

---

[3] We have used a plane-parallel geometry with ionizing spectrum from *CoStar* stellar atmosphere model of Schaerer & de Koter (1997).

thermal pressures are too low to be in equilibrium with the K06 PDR models, which have at least 10^6 cm^{-3} K. In fact, the pressure in the PDR increases when the PDR contribution of [CII]158μm is reduced, leading to more tension with very low density HII region models. Pressure-matching[4] with the K06 PDRs favors HII region models with $n_{\mathrm{H}^+} = 0.56$–3.2×10^2 cm^{-3}, corresponding to $\alpha_{\mathrm{[CII],HII}^\star} = 0.23$–$0.08$.

While pressure equilibrium between the HII regions and PDRs may be an overly idealized assumption, observations in star-forming regions, individual galaxies, and statistical samples of galaxies (cf. Oberst et al. (2006), Rangwala et al. (2011), and Vasta et al. (2010) for examples of each) indicate $\alpha_{\mathrm{[CII],HII}^\star} < 0.3$. Thus, we adopt the upper value derived from the pressure-matched solution, $\alpha_{\mathrm{[CII],HII}^\star} = 0.2$, and correspondingly subtract the HII region component from the measured flux. We find that the corrected diagnostic ratios favor $n_{\mathrm{H}} = 5.6 \times 10^3$ cm^{-3} and $G_0 = 5.6 \times 10^2$. If we correct $F_{\mathrm{[CII]}}$ with the combined contributions from the NLR and HII regions, as in Equation 1.3.1, we find that the only change in the preferred PDR solution is an increase in G_0 to 10^3.

Geometric considerations

Following Stacey et al. (2010a) and authors thereafter, it is useful to compare the value of G_0 predicted from the PDR models with the value estimated solely from geometric considerations. As described in Wolfire et al. (1990), if PDR surfaces and the sources of radiation are randomly distributed—such as in the case of stellar populations—within a region of diameter D, then the photons in this region will likely be absorbed by a PDR cloud before traveling a distance D so that the impingent FUV flux on cloud surfaces in the emitting region is simply related to the surrounding volume density of FUV photons, $G_0 \propto (\lambda L_{\mathrm{FIR}})/D^3$, where λ is the mean-free path of FUV photons. However, if FUV photons can travel large distances (compared to D) until being absorbed, then the FUV flux will vary as the surface flux of FUV photons, $G_0 \propto L_{\mathrm{FIR}}/D^2$. The constants of proportionality can be determined by calibrating to known values[5] of G_0, L_{FIR}, and D for M82 (as in, for example, Stacey et al. (2010a)). These two scenarios, set apart by different assumptions regarding λ, represent limiting cases for which we can calculate the expected G_0, given D and L_{FIR} for the Cloverleaf.

To make this comparison, we adopt the source size inferred from gravitational lens modeling (VS03) of spatially resolved CO(7-6) flux, implicitly assuming that the CO(7-6) line emission is co-spatial with the FIR continuum. For the Cloverleaf, there exists spatially resolved continuum data (F15) in the rest-frame FIR (122μm) that would—barring significant contribution at this wavelength from the AGN as

---

[4] Given the discrepancies in the internal radiative transfer, adopted microphysics, etc., we consider pressures between the HII region and the PDR models to be in equilibrium as long as the values agree within a factor of 2.

[5] For M82, $G_0 = 10^{2.8}$ and $L_{\mathrm{FIR}} = 3.2 \times 10^{10}$ (Colbert et al. 1999a), and $D = 300$ pc (Joy et al. 1987)

inferred from the double-peaked SED in Weiß et al. (2003)— enable a direct measurement of the extent of the FIR-emitting region in the context of a gravitational lens model that relates the observed surface brightness distribution to a physical size in the source plane. A comparison between the 122μm continuum and CO(7-6) maps shows that the two tracers peak at the same locations the four lensed quasar images, supporting our claim that the two emission regions overlap. Setting D = 1.3 kpc, then, we estimate $G_0 \sim$ 1.3–5.7$\times 10^3$ using the two relations with different assumptions about the mean-free path of FUV photons in the Cloverleaf disk.

This inferred G_0 value is above the range predicted by the PDR diagnostic line ratios when assuming all observed [CII]158μm and [OI]63μm is produced in PDRs. Broadly, larger values of $F_{\rm [OI],PDR}/F_{\rm [CII],PDR}$ tend to implicate higher values of G_0. It is important to note that we do not consider increasing the [OI]63μm flux beyond the extinction and optical depth correction factors already discussed, as there is no evidence of self-absorption in the spectrally resolved [OI]63μm line profile. Simultaneous decreases in $F_{\rm [OI],PDR}$ and $F_{\rm [CII],PDR}$, which increases the FIR continuum flux relative to the total FS line cooling, points to higher G_0, as well (cf. Figure A.13). The effects on the derived PDR parameters of reducing the PDR contribution of [CII]158μm while keeping the [OI]63μm flux constant, of reducing the PDR contribution while keeping the [CII]158μm flux fixed, and of decreasing by equal amounts the PDR contributions of [OI]63μm and [CII]158μm are illustrated by vectors drawn in the righthand panel of Figure A.13.

CO from PDR models

Next we compare the PDR diagnostic diagram constructed with FS line ratios to previous attempts at interpreting CO emission in the Cloverleaf using the PDR paradigm. In B09, the authors found that line ratios from K06 PDR models with densities and FUV fields in the range of $n_{\rm H}$ = 1–4$\times 10^5$ cm^{-3} and G_0 =1–5$\times 10^3$ provided a suitable match to the measured CO line ratios $F_{{\rm CO}(J=7\rightarrow 6)}/F_{\rm FIR}$ and $F_{{\rm CO}(J=6\rightarrow 5)}/F_{{\rm CO}(J=2\rightarrow 1)}$. ($F_{{\rm CO}(J=2\rightarrow 1)}$ used here is the flux expected if the line is thermalized at the same temperature as the observed CO(J = 3 $\rightarrow$ 2) line.) In the righthand panel of Figure A.13, we supplement the analysis in B09 with the observed, extinction-corrected [OI]63μm and [CII]158μm fluxes. For consistency, we show the same pair of CO diagnostic ratios used in B09, and find that the FS line ratio diagnostics favor lower $n_{\rm H}$ and G_0 than the CO diagnostics. Notably, if the origin of observed CO transitions could indeed be traced to PDRs with densities of order $\sim 10^5$ cm^{-3}, we would have expected this emission to be accompanied by concomitantly high [OI]63μm flux. Instead, the high density solution inferred from these mid-J CO line ratios overproduces and underproduces [OI]63μm and [CII]158μm, respectively; or, equivalently, the low density solution suggested by the FS lines under-predicts the observed $F_{{\rm CO}(J=7\rightarrow 6)}$ by factors of 10–100. For illustrative purposes, we have drawn vectors which show the direction and magnitude of change in $n_{\rm H}$ and G_0, corresponding to different assumptions of $\alpha_{\rm [CII],PDR}$ and $\alpha_{\rm [OI],PDR}$. *Importantly, we find that there exists no combination of* $\alpha_{\rm [CII],PDR}$ *and* $\alpha_{\rm [OI],PDR}$ *that can eliminate the discrepancy in mid-J CO- and FS line-derived PDR conditions, leading us to conclude that PDR conditions inferred from [OI]63μm and [CII]158μm fluxes fail to describe the observed mid-J CO emission.*

Furthermore, the high fluxes of the mid-J CO transitions relative to the FIR continuum flux observed in the Cloverleaf were noted in B09 as being anomalously high compared to typical fluxes observed in nearby ($z \sim 0$) starbursts. In Figure 1.9, we show a comparison to 27 local Luminous Infrared Galaxies (LIRGs; $L_{\rm IR} \geq 10^{11}$ L$_\odot$) and Ultra Luminous Infrared Galaxies (ULIRGs; $L_{\rm IR} > 10^{12}$ L$_\odot$) in the *Herschel* Comprehensive ULIRG Emission Survey (HerCULES) sample (Rosenberg et al. 2015)[6]. It is clear that the Cloverleaf exhibits both unusually high CO line-to-FIR continuum luminosity ratios for transitions $J > 6$, and a higher level of excitation in its spectral line energy distribution (SLED) than most of the galaxies—including 12 starbursts, 3 AGN, and 11 composite starburst/AGN systems. A notable exception is the known merger remnant and starburst/AGN composite system, NGC 6240. Quantitatively, the sum of FIR-normalized CO luminosities from $J = 5$ to $J = 9$, $\sum_{J=5}^{J=9} L_{{\rm CO}(J\rightarrow J-1)}/L_{\rm FIR}$, is, on average, equal to 1.5×10^{-4} for the HerCULES galaxies, and 3.7×10^{-4} for the Cloverleaf. We reach the same conclusion when comparing the Cloverleaf's CO emission to a more comprehensive compilation of CO SLEDs in Greve et al. (2014), which includes 20 purely star-forming galaxies from the HerCULES sample, as well as additional star-forming local (U)LIRGs, and a statistically significant sample of high redshift ($0.1 < z < 6$) starbursts. We note that authors in both Greve et al. (2014) and Rosenberg et al. (2015) similarly disfavor far-UV heating from SF as the sole excitation mechanism for CO in the majority of the galaxies studied, given their elevated CO-to-FIR ratios and high excitation levels compared to the Milky Way or M 82, citing mechanical heating deposited to the gas from supernovae-driven turbulence or cosmic-rays, for example, as possible alternatives in sources with little or no contribution from AGN. In Section 1.3.4, we consider the possibility of cosmic-ray- and shock-heating in the Cloverleaf.

1.3.3 X-ray dominated region

X-ray energy released from an accreting SMBH was proposed in B09 as an alternate source of gas heating responsible for the observed level of CO emission, since the close proximity of dense molecular gas in the Cloverleaf disk to the central AGN could result in conditions favorable to the formation of X-ray Dominated Regions (XDRs). When the neutral ISM is exposed to hard ($E_\gamma > 1$ keV) X-rays, gas heat-

---

[6] The full HerCULES sample includes 29 galaxies. We have excluded 2 galaxies with spectra containing [OI]63μm in absorption.

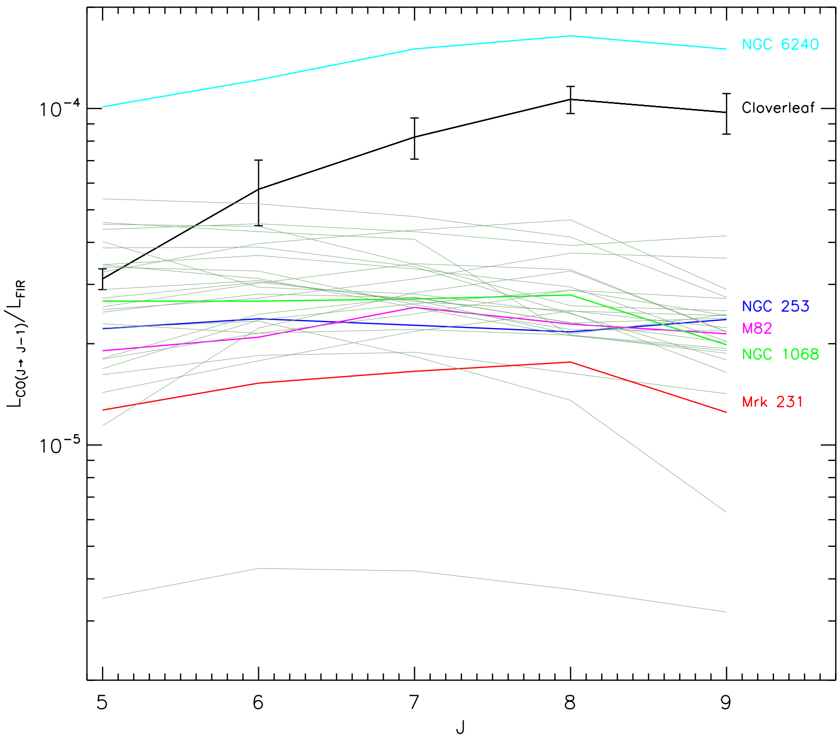

Figure 1.9: Cloverleaf CO SLED, normalized to L_{FIR}, compared to local (U)LIRGs (grey curves) of the HerCULES sample (Rosenberg et al. 2015). CO SLEDs for HerCULES galaxies NGC 253, NGC 1068, NGC 6240, and Mrk 231 are highlighted in blue, green, red, and cyan, respectively. M 82 (magenta curve) is also included here with data from Panuzzo et al. (2010).

ing is dominated by Coulomb interactions between thermal electrons and electrons released from the ionization of H or H_2. Ionizations can occur directly by an X-ray, or by secondary electrons if primary X-ray photon energy is sufficiently high; the ionization state (characterized by the electron fraction x_e) determines which ionization method dominates the gas heating. The rate of energy deposited in the gas by X-rays, called H_{X}, divided by the gas density, n, is an important parameter in determining the thermal and chemical structure of an XDR. Figure 1.10 depicts the variation of temperature and chemical abundances as a function of H_{X}/n. The decreasing value of H_{X}/n from left to right in the figure can be representative of the attenuation of X-ray flux with increasing depth into the cloud.

XDRs can produce strong emission, as in PDRs, from electronic transitions of trace metals like O^0, C^+, and CO, because the attenuation of X-ray flux is much slower in XDRs and the gas heating more efficient—compare up to 100% efficiencies for X-ray heating via direct ionization to $\sim 30\%$ efficiencies for photoelectric heating of dust grains in PDRs. These properties often lead to higher emergent intensities of these spectral lines from XDR cloud surfaces and larger line-to-L_{FIR} ratios. The relative importance of each line transition in the gas cooling depends mainly on the

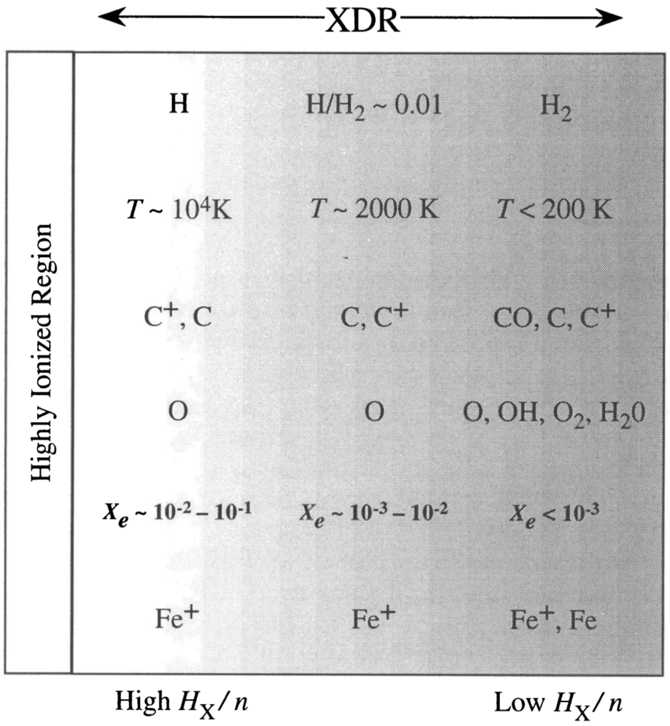

Figure 1.10: Schematic diagram for the thermal and chemical structure of a typical XDR. Figure from Maloney et al. (1996).

X-ray flux and gas density.

Considering only the total CO cooling, B09 identified a region in the parameter space of radial distance, R, from the AGN and gas density, namely, 500 pc $< R <$ 1500 pc and $n_{\rm H} > 3 \times 10^4$ cm^{-3} for which the resulting CO surface brightness from corresponding XDR models, $S^{\rm (B09)}_{\rm CO,XDR}$ (units of erg s^{-1} cm^{-2}), matched the observed CO surface brightness, $S_{\rm CO}$, in the Cloverleaf disk for a range of areal filling factors, $\phi_{\rm ff}$. Note that R is a proxy for the X-ray flux, $F_{\rm X}$, when assuming, as in B09, fixed values of the hard (2–10 keV) X-ray luminosity, $L_{\rm X}$, and attenuating column of foreground hydrogen, $N_{\rm H_{att}}$. For reference, an X-ray luminosity of 10^{46} erg s^{-1} and attenuating hydrogen column of 3×10^{23} cm^{-2} translates to an X-ray flux of 10 erg s^{-1} cm^{-2} at $R = 600$ pc. We note that in this framework, a larger distance is equivalent to a model with a larger attenuating column and/or lower $L_{\rm X}$ than the fiducial model considered here.

In this section, we examine whether the predicted [CII]158μm and [OI]63μm surface brightnesses, $S^{\rm (B09)}_{\rm [CII],XDR}$ and $S^{\rm (B09)}_{\rm [OI],XDR}$, associated with the corresponding CO-constrained XDR models from B09 are consistent with observations. Furthermore, we determine the relative importance of X-ray versus stellar UV heating in producing the observed FS line cooling. We make use of the same grid of theoretical XDR models presented in B09, which are based on improved models of Maloney et al. (1996), to determine $\alpha_{i,\mathrm{XDR}}$. If we express $S^{(\mathrm{B09})}_{[\mathrm{CII}],\mathrm{XDR}}$ and $S^{(\mathrm{B09})}_{[\mathrm{OI}],\mathrm{XDR}}$ in terms of the observed XDR flux of CO, $F_{\mathrm{CO,XDR}}$, then we can write the respective fractions $\alpha_{[\mathrm{OI}],\mathrm{XDR}}$ and $\alpha_{[\mathrm{CII}],\mathrm{XDR}}$ as

$$\alpha_{[\mathrm{OI}],\mathrm{XDR}} = \frac{\gamma^{(\mathrm{B09})}_{[\mathrm{OI}],\mathrm{XDR}} \times F_{\mathrm{CO,XDR}}}{F_{[\mathrm{OI}]}} \tag{1.3.3}$$

$$\alpha_{[\mathrm{CII}],\mathrm{XDR}} = \frac{\gamma^{(\mathrm{B09})}_{[\mathrm{CII}],\mathrm{XDR}} \times F_{\mathrm{CO,XDR}}}{F_{[\mathrm{CII}]}}, \tag{1.3.4}$$

where

$$\gamma^{(\mathrm{B09})}_{[\mathrm{OI}],\mathrm{XDR}} = \frac{S^{(\mathrm{B09})}_{[\mathrm{OI}],\mathrm{XDR}}}{S^{(\mathrm{B09})}_{\mathrm{CO,XDR}}}$$

$$\gamma^{(\mathrm{B09})}_{[\mathrm{CII}],\mathrm{XDR}} = \frac{S^{(\mathrm{B09})}_{[\mathrm{CII}],\mathrm{XDR}}}{S^{(\mathrm{B09})}_{\mathrm{CO,XDR}}}$$

Equations 1.3.3 and 1.3.4 implicitly assume that the [CII]158μm, [OI]63μm, and CO emission arise from the same XDR component characterized by a single areal filling factor ϕ_{ff}.

The precise value of $F_{\mathrm{CO,XDR}}$ depends on what fraction of F_{CO} is attributed to the XDR. While B09 found successful XDR models assuming $F_{\mathrm{CO,XDR}} = F_{\mathrm{CO}}$, here we include the possibility of a star-formation component for the CO emission. We know from observations of a pure starburst like M 82, for instance, that PDR models under-predict the observed mid-J CO emission (Kamenetzky et al. 2012), as found in this work. Thus, we consider two limiting cases where 1) the starburst contribution to CO is minimal and we can attribute all of the observed CO to an XDR such that $F_{\mathrm{CO,XDR}} = F_{\mathrm{CO}}$ and 2) the starburst contribution to CO is "M 82-like" and amounts to 2×10^{-4} of the observed FIR luminosity, as per M 82 (Kamenetzky et al. 2014), leading to $F_{\mathrm{CO,XDR}} = 0.7F_{\mathrm{CO}}$. Note that M 82 is a good reference source given the similarity of its SLED to the sample of CO SLEDs in local (U)LIRGs displayed in Figure 1.9.

Figure 1.11 shows the expected surface brightness (red contours) for [OI]63μm and [CII]158μm, denoted $S^{(\mathrm{B09})}_{[\mathrm{OI}],\mathrm{XDR}}$ and $S^{(\mathrm{B09})}_{[\mathrm{CII}],\mathrm{XDR}}$, produced in the B09 XDR model grid as functions of radius and density. Contours for $S^{(\mathrm{B09})}_{\mathrm{CO,XDR}}$ indicating 0.6 and 0.2 erg s^{-1} cm^{-2} are redrawn here from B09 (cf. their Figure 7) to facilitate comparison with results for the FS lines. These values represent partial ($\phi_{\mathrm{ff}} = 1/3$) and complete ($\phi_{\mathrm{ff}} = 1$) areal coverage, respectively, of the observed total CO luminosity ($= 3.3 \times 10^9$ L$_\odot$) distributed over the surface of the disk, and bound the allowed parameter space of R and n_{H} for the XDR models which successfully describe the observed CO emission in the case where $F_{\mathrm{CO,XDR}} = F_{\mathrm{CO}}$. Also shown are a pair of surface brightness contours ($S^{(\mathrm{B09})}_{\mathrm{CO,XDR}} = 0.42$ and 0.14 erg s^{-1} cm^{-2}) for the same

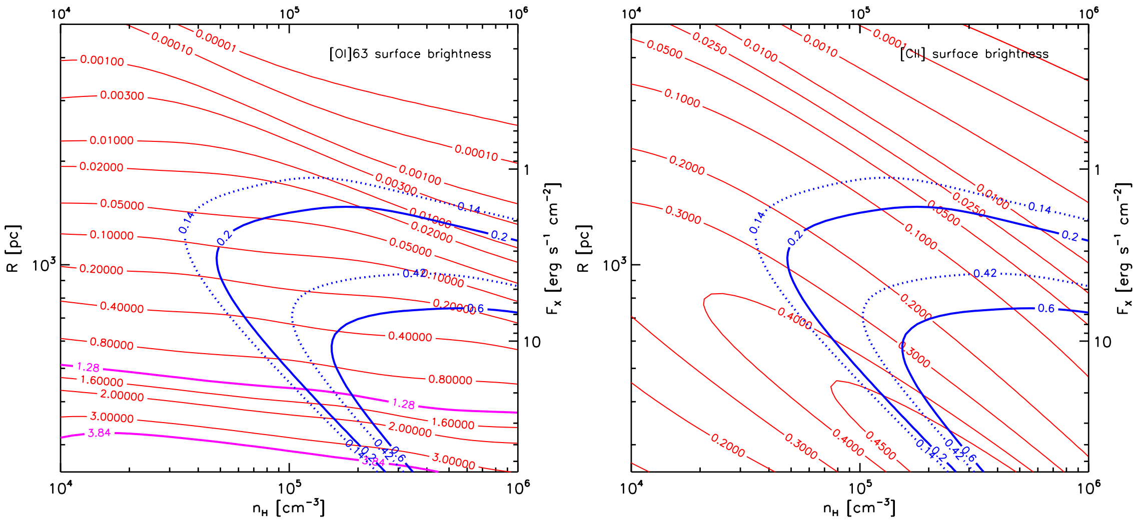

Figure 1.11: XDR predictions for [OI]63 (*left panel*) and [CII] (*right panel*) surface brightness, computed as a function of distance, R, from the AGN and density, $n_{\rm H}$ for a model grid with $N_{\rm H,att} = 3\times10^{23}$ cm^{-2} and $L_{\rm X} = 10^{46}$ erg s^{-2}. Thick magenta curves indicate observed FS line surface brightness, assuming area filling factors of 1 and 1/3. Thick blue curves denote CO surface brightness for the case $S^{\rm XDR}_{\rm CO,tot} = S_{\rm CO,tot}$, with filling factors of unity and 1/3. Thin dotted blue contours represent the case where $S^{\rm XDR}_{\rm CO,tot} = 0.7 S_{\rm CO,tot}$ for the same two filling factors.

area filling factors $\phi_{\rm ff} = 1/3$ and 1, computed for the case where $F_{\rm CO,XDR} = 0.7F_{\rm CO}$, described above. Thick red contours on the [OI]63μm surface brightness map indicate the observed surface brightness for [OI]63μm for $\phi_{\rm ff} = 1$ and 1/3, namely, 1.28 and 3.84 erg s^{-1} cm^{-2}, respectively; the [CII]158μm surface brightness predicted from the B09 XDR model never reaches the observed values for the filling factors considered.

For [OI]63μm, models at radii less than the VS03 disk radius of 650 pc predict line surface brightness comparable to or larger than the corresponding CO surface brightness. At the smallest radii in the model grid, it can be as much as ∼6–20 times brighter than the observed CO, depending on filling factor: $\left(S_{\rm [OI]63,XDR}\right)_{\rm B09}$ and $(S_{\rm CO,XDR})_{\rm B09}$ are roughly orthogonal in this regime, so we can keep the predicted CO surface brightness fixed while rapidly increasing the [OI]63μm surface brightness. These large [OI]63μm surface brightnesses, when converted to luminosities via their respective area filling factors, amount to luminosities that are greater than the measured $L_{\rm [OI]}$, i.e., correspond to models with $\alpha_{\rm [OI],XDR} > 1$. We can then use the observed [OI]63 luminosity to identify a minimum distance, R_{min}, for XDR models that satisfy constraints by both FS line and CO emission. This bound occurs at higher radii (R_{min} = 450 pc) for models with $\phi_{\rm ff}$ close to unity than for models with smaller values of $\phi_{\rm ff}$, which begin to produce unrealistically high [OI]63μm luminosities at $R_{min} \leq 250$ pc. The choice of a minimal or M82-like starburst paradigm has negligible effect on deriving R_{min}, as the contours of $S^{\rm (B09)}_{\rm CO,XDR}$ are very tightly spaced at $R < 650$ pc.

At larger radii, $S^{(\mathrm{B09})}_{[\mathrm{OI}],\mathrm{XDR}}$ can be less than the observed CO surface brightness, with the XDR models contributing at most 30% of the measured [OI]63μm flux at $R > 650$ pc. At such radii and high densities, $S^{(\mathrm{B09})}_{[\mathrm{OI}],\mathrm{XDR}}$ is ~ 2 orders of magnitude below $S^{(\mathrm{B09})}_{\mathrm{CO},\mathrm{XDR}}$, and $\alpha_{[\mathrm{OI}],\mathrm{XDR}}$ is of order $\sim 1\%$ in this regime.

For [CII]158μm, unless $\phi_{\mathrm{ff}} > 1$, there are no XDR models tested which can account for all of the measured luminosity, which agrees with the expectation that [CII]158μm traces primarily the star-formation process. At most, for each assumption about the starburst contribution to CO luminosity, $S^{(\mathrm{B09})}_{[\mathrm{CII}],\mathrm{XDR}}$ can be twice and three times as much, respectively, as $S^{(\mathrm{B09})}_{\mathrm{CO},\mathrm{XDR}}$ in the acceptable parameter space at $R < 650$ pc and $n_{\mathrm{H}} > 3 \times 10^4$ cm^{-3}. Like $S^{(\mathrm{B09})}_{[\mathrm{OI}],\mathrm{XDR}}$, $S^{(\mathrm{B09})}_{[\mathrm{CII}],\mathrm{XDR}}$ is small compared to $S^{(\mathrm{B09})}_{\mathrm{CO},\mathrm{XDR}}$ for large radii ($R \gtrsim 1000$ pc) and high densities ($n_{\mathrm{H}} \gtrsim 10^5$ cm^{-3}), and $\alpha_{[\mathrm{CII}],\mathrm{XDR}} \sim 1\%$ here.

It is clear from Figure 1.11 that $\alpha_{i,\mathrm{XDR}}$ varies widely throughout the allowable parameter space. Figure 1.12 depicts $\alpha_{[\mathrm{OI}],\mathrm{XDR}}$ and $\alpha_{[\mathrm{CII}],\mathrm{XDR}}$ as a functions of R and n_{H} for the CO-constrained models with $1 < \phi_{\mathrm{ff}} < 1/3$. (Recall that, for the minimal and M 82-like starbursts, respectively, area filling factors $\phi_{\mathrm{ff}} = 1$–$1/3$ correspond to $S^{(\mathrm{B09})}_{\mathrm{CO},\mathrm{XDR}} = 0.2$–$0.6$ erg s^{-1} cm^{-2} and 0.14–0.42 erg s^{-1} cm^{-2}.) In this figure, $\alpha_{i,\mathrm{XDR}}$ has been computed at each locus in R and n_{H} according to Equations 1.3.3 and 1.3.4. Again, we have assumed identical filling factors for CO and FS line emission.

Lacking additional constraints to guide us to fiducial values of R and n_{H}, we partition the available parameter space of the XDR model grid into qualitatively distinct regions of R and n_{H} to provide a comprehensive summary of expected contributions to the FS lines from the CO-constrained XDR. The various regimes considered are:

I: Moderate radius/moderate density ($R = 600$ pc and $n_{\mathrm{H}} = 10^5$ cm^{-3})

II: Large radius/low density ($R = 1000$ pc and $n_{\mathrm{H}} = 5 \times 10^4$ cm^{-3})

III: Small radius/moderate density ($R = 500$ pc and $n_{\mathrm{H}} = 10^5$ cm^{-3})

IV: Small radius/high density ($R = 350$ pc and $n_{\mathrm{H}} = 2 \times 10^5$ cm^{-3})

V: Large radius/high density ($R = 1430$ pc and $n_{\mathrm{H}} = 2 \times 10^4$ cm^{-3})

Each case is marked on Figure 1.12, and is associated with a particular value of $\alpha_{[\mathrm{OI}],\mathrm{XDR}}$ and $\alpha_{[\mathrm{CII}],\mathrm{XDR}}$, which is recorded in Table 1.2. Broadly, we find that the CO-constrained XDRs are capable of producing between 20–40% of observed [CII]158μm and 5–20% of [OI]63μm for moderate X-ray fluxes, F_{X} of order ~ 1.6–10 erg s^{-1} cm^{-2}, and densities $n_{\mathrm{H}} = 0.5$–1×10^5 cm^{-3} (Cases I and II). For higher F_{X} and n_{H}, namely, $F_{\mathrm{X}} \sim 10$–30 erg s^{-1} cm^{-2}, $n_{\mathrm{H}} = 1$–2×10^5 cm^{-3}, the contributions increase for both FS lines, and X-ray heating can provide the main source of gas heating for the observed [OI]63μm emission: $\alpha_{\text{[CII],XDR}} = 0.2$–$0.4$ and $\alpha_{\text{[OI]63,XDR}} = 0.7$–$0.8$ (Case III and IV). For the case of high densities and low fluxes, however, there is negligible ($< 5\%$) contribution to the FS lines (Case V), and stellar UV heating in PDRs clearly dominates as the mechanism responsible for producing the observed FS line cooling in this regime.

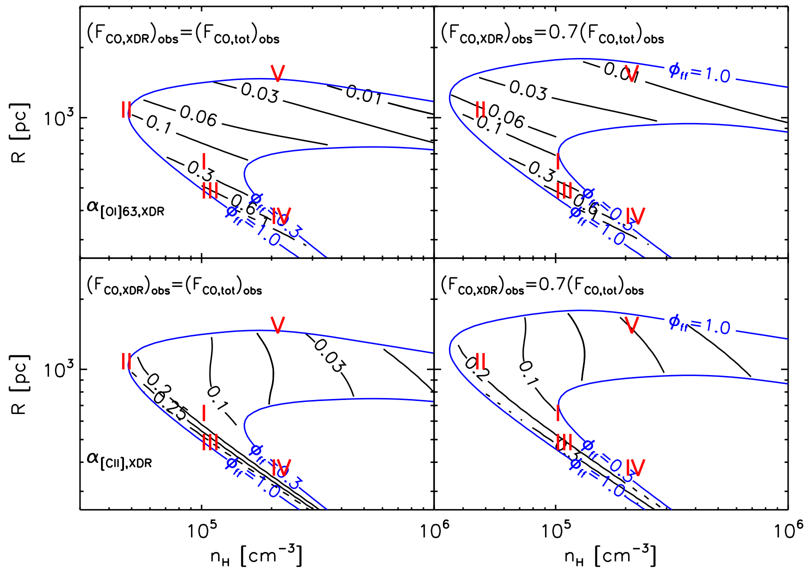

Figure 1.12: Contours of constant $\alpha_{\text{[OI],XDR}}$ (top panel) and $\alpha_{\text{[CII],XDR}}$ for XDR models that reproduce the observed CO surface brightness with area filling factors between $\phi_{\text{ff}} = 0.3$ and 1, according to the minimal and M 82-like starburst paradigms. Roman numerals "I", "II", "III", "IV", and "V" highlight positions in the R-n_{H} plane that we consider as representative cases of various qualitatively distinct regimes in the allowed parameter space..

Implications for PDR modeling Having determined the level of contribution to [CII]158μm and [OI]63μm fluxes from a range of XDRs capable of producing the observed CO emission, we can now examine the physical consequences of introducing these XDR contributions in the context of a composite ISM model where the gas is heated from both AGN activity and star formation. In particular, we would like to determine the effects of the X-ray component on physical parameters determined for the PDR gas by correcting the attributed PDR flux according to the following equations:

$$F_{\text{[OI],PDR}} = (1 - \alpha_{\text{[OI],XDR}}) \times F_{\text{[OI]}} \tag{1.3.5}$$

$$\begin{aligned} F_{\text{[CII],PDR}} = (1 - \alpha_{\text{[CII],NLR}} - \alpha_{\text{[CII],HII}^\star} \\ - \alpha_{\text{[CII],XDR}}) \times F_{\text{[CII]}} \end{aligned} \tag{1.3.6}$$

Figure 1.13 shows the resulting PDR diagnostic plots for each assumed starburst template, after contributions from XDR (Cases I–V) , NLR, and stellar HII

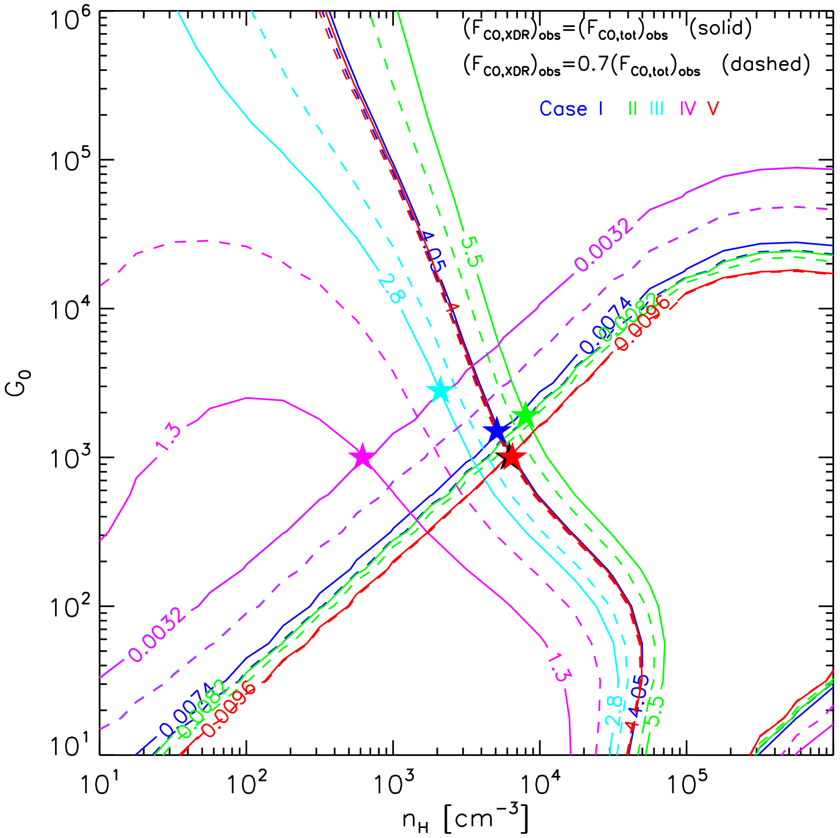

Figure 1.13: PDR diagnostics for ISM models including a contribution from the CO-constrained XDR. Diagnostic ratios plotted are the same as in Figure A.13: $F_{\rm [OI],PDR}/F_{\rm [CII],PDR}$ and $(F_{\rm [OI],PDR} + F_{\rm [CII],PDR})/F_{\rm FIR}$. (Recall that the curves for $(F_{\rm [OI],PDR} + F_{\rm [CII],PDR})/F_{\rm FIR}$ run from the lower-left to upper-right region of the plot, and the $F_{\rm [OI],PDR}/F_{\rm [CII],PDR}$ contours run from the upper-left to lower-right region.) Black star symbol at $G_0 = 10^3$ and $n_{\rm H} = 5.2 \times 10^3$ cm^{-3} indicates the PDR solution for the NLR+HII+PDR model (i.e., excluding an XDR contribution). Colored star symbols indicate PDR solutions for the corresponding Cases of the same color defined in the legend.

region components have been subtracted from the measured line fluxes; the FIR continuum is unchanged because we do not expect significant contribution from ISM components other than PDRs. The ISM model with only NLR and HII region contributions ("NLR+HII+PDR"; indicated in Figure 1.13 as the star symbol at $G_0 = 10^3$ and $n_{\rm H} = 6 \times 10^3$ cm^{-3}) serves as a reference point for assessing the effect of the CO-bright XDR on the derived PDR conditions. We find that, in general, the value of G_0 ($\sim 10^3$) determined from the PDR models remains fairly robust to changes in the input $F_{\rm [CII],PDR}$ and $F_{\rm [OI],PDR}$ introduced by the CO-constrained XDR models, never falling outside the range of $G_0 = 1$–3×10^3. In fact, G_0 only changes with respect to the NLR+HII+PDR model for XDR models with the lowest densities and large radii (i.e., low X-ray fluxes; e.g., Case II), where the [OI]63μm production in the corresponding XDRs are negligible but $\alpha_{\mathrm{[CII],XDR}} \sim 0.3$. This result is in line with the analytic estimate for G_0 from Section 1.3.2, and suggests that the FS line emission is indeed being produced in a region with spatial extent $D = 1.3$ kpc. The PDR density is more sensitive to the given XDR model, with n_{H} spanning the range of $\sim$ 7–100$\times10^2$ cm^{-3} for the Cases considered. The largest change to the PDR density—where n_{H} decreases to $\sim$ 700 cm^{-3}—on the other hand, occurs when adopting XDR models with small radii and high densities (Case IV), where the majority ($\sim$ 55–80%, depending on the starburst template) of [OI]63μm flux is removed from the PDR and attributed to the XDR component.

1.3.4 Alternative heating sources

Shocks Molecular gas excited by interstellar shock waves can also exhibit the high CO line-to-FIR continuum luminosity ratios characteristic of X-ray irradiated gas, due to the greater efficiency of gas heating relative to dust heating in the shock process. Among the HerCULES CO SLEDs plotted in Figure 1.9, for example, NGC 6240—a known galaxy-galaxy merger with strong evidence for shock-excited CO (Meijerink et al. 2013)—is a clear outlier in terms of its observed CO-to-FIR continuum luminosity ratio—any given rotational transition above $J = 5$ carries on the order of $\sim 10^{-4}$ of the system's FIR luminosity—and CO SLED shape. X-ray heating as a gas heating mechanism is disfavored in NGC 6240 because the CO emission does not originate close to either of the two AGN nuclei in the system, so that the incident X-ray flux on the 500-pc wide (Tacconi et al. 1999) CO cloud is $\lesssim 1$ erg s^{-1} cm^{-2} (Komossa et al. 2003). While there is no evidence, e.g. a disturbed morphology, to support an active merger in the Cloverleaf, there is no obvious reason to rule out shock excitation of CO in this case as interstellar shock waves can arise from phenomena related to the Cloverleaf's starburst and AGN, which are ample sources of mechanical energy. The total CO cooling is only 0.0049% and 0.063% of the total AGN bolometric power output and the starburst power output, respectively, while observations suggest that up to 5% (Cicone et al. 2014) of the total energy can go into mechanical processes.This means that if $\gtrsim 0.1\%$ (or $\gtrsim 1\%$) of the kinetic power from mechanical processes is converted to power radiated in CO, then the requisite mechanical energy to power the observed CO cooling from the AGN (or starburst) is readily achieved.

First we compare the CO excitation in the Cloverleaf to the predicted excitation from the shock models of Flower & Pineau Des Forêts (2010). Figure 1.14 shows the CO SLEDs for models of C-type shocks with pre-shock densities of $n_{\mathrm{H}} = 2\times10^4$ cm^{-3} and 2×10^5 cm^{-3}, and velocities, v_{shock}, ranging from 10–40 km s^{-1}. Note that the CO SLEDs have been normalized to the luminosity of the $J = 8 \rightarrow 7$ transition in the Cloverleaf. While it appears that there is no single shock model that reproduces the shape of the CO SLED for all measured transitions down to $J = 1$, models with $n_{\mathrm{H}} = 2\times10^4$ cm^{-3} and velocities 30 km s^{-1} or 40 km s^{-1}

provide a reasonable fit to the observed CO excitation for the transitions $J \geq 5$. While B09 and Riechers et al. (2011a) were able to reproduce the fluxes in all of the observed CO transitions down to $J = 3$ and $J = 1$, respectively, with single-component models, this fact alone does not rule out the scenario in which a range of physical conditions—such as multiple kinds of shocks with distinct velocities or multiple gas components with distinct densities—will contribute to the observed SLED. Therefore, we do not rule out shocks as a mechanism for CO excitation based solely on the inability of a model characterized by a single $n_{\rm H}$ and v_{shock} to match the CO spectrum at $J < 5$.

Another approach is to compare the total observed CO surface brightness, 0.2 erg $\rm s^{-1}$ $\rm cm^{-2}$, to the surface brightness produced in the shock models. According to Flower & Pineau Des Forêts (2010), the surface brightnesses for the CO—where we have summed surface brightnesses reported for transitions J = 1-17 to represent the total emission—produced in the model shocks with $n_{\rm H} = 2 \times 10^4$ $\rm cm^{-3}$ and shock speeds of 10, 20, 30, and 40 km $\rm s^{-2}$ are 4.0×10^{-3}, 9.1×10^{-3}, 1.3×10^{-2}, and 1.7×10^{-2} erg $\rm s^{-1}$ $\rm cm^{-2}$, respectively. Based on the incompatibility between the observed and predicted CO SLED shapes shown in Figure 1.14, we do not consider models with pre-shock densities of 2×10^5 $\rm cm^{-3}$, but note that the surface brightness is increased for these models, up to 9.2×10^{-2} erg $\rm s^{-1}$ $\rm cm^{-2}$ for $v_{shock} = 40$ km $\rm s^{-1}$. Thus, the lower density shock models can only reproduce 2.0-8.5% of the observed surface brightness, or smaller percentages for $\phi_{\rm ff} < 1$. If, however, $\phi_{\rm ff} > 1$ in the Cloverleaf, then it may be possible to have a superposition of shocks in the same line-of-sight, thus increasing the resulting surface area of CO-emitting gas. For example, a total number of 8 million molecular gas clumps with average density $n_{\rm H} = 2 \times 10^4$ $\rm cm^{-3}$ and radius $r_{\rm clump} = 0.8$ pc reproduces the observed molecular gas mass of $M_{\rm H_2} \sim 8.5 \times 10^8$ $\rm M_\odot$—where the value of $M_{\rm H_2}$ quoted here is the geometric mean of the ranges allowed by the likelihood analysis from B09—and yields a combined surface area of 6×10^{44} $\rm cm^2$. When distributed over a disk which has inner and outer radii of 180 pc (for the NLR radius inferred from F15) and 650 pc, this number and size of clumps gives an area filling factor of $\phi_{\rm ff} \sim 10$. In that case, a single shock with velocity $v_{shock} = 40$ km $\rm s^{-1}$ propagating through a disk with ~ 10 sharing a single line-of-sight would produce a CO luminosity comparable to the observed value of $\sim 1.3 \times 10^{43}$ erg $\rm s^{-1}$.

We point out that for NGC 6240, multiple shock fronts along the line-of-sight are not required to reproduce the observed surface brightness of ~ 0.06 erg $\rm s^{-1}$ $\rm cm^{-2}$ (including transitions up to $J = 13 \rightarrow 12$). Indeed, the evidence for shock-heating is supported by both a good fit to the observed CO SLED and measured line fluxes using a model with pre-shock density $n_{\rm H} = 5 \times 10^4$ $\rm cm^{-3}$ and $v_{shock} = 10$ km $\rm s^{-1}$ (Meijerink et al. 2013).

In addition to the shock models, we can consider the basic energetics of mechanical energy dissipation. In a turbulent medium where a large number of shocks supply sufficient mechanical energy to heat the molecular gas and drive its cooling, we can use the expression from Bradford et al. (2005), namely, $L/M = 1.10 \times (v_{turb}/25 \text{ km s}^{-1})^3 \times (1 \text{ pc}/\Lambda)$, to estimate the total molecular gas cooling provided by turbulent motions in the Cloverleaf ISM. In this expression, L and M are the total luminosity and mass in molecular gas, v_{turb} is the velocity of turbulent motions, and Λ is the physical dimension over which turbulence occurs, e.g, the molecular clump size. Lacking observations of the molecular line emission from H_2, the total luminosity of molecular line emission L in the Cloverleaf is unknown, so we use instead the value of luminosity that is appropriate for CO, namely, $L_{\rm CO}$. This will underestimate the actual total molecular gas cooling per mass, but we note that for gas kinetic temperatures of 50–60 K, cooling via H_2 will be subdominant to CO. In that case, the total CO luminosity of 3.3×10^9 $L_\odot$ and molecular gas mass of $M_{\rm H_2} \sim 8.5 \times 10^9$ $M_\odot$ yield a specific luminosity of ~ 0.39 $L_\odot$ $M_\odot^{-1}$. We set $v_{turb} = v_{shock} = 30$ and 40 km s^{-1} based on the SLED analysis above, and determine the size scale, Λ, that reproduces the observed cooling to be 5 pc and 10 pc, respectively, for $v_{turb} = 30$ km s^{-1} and 40 km s^{-1}. We note that a total number of 33,000 (4,100) molecular gas clumps with an average density of $n_{\rm H} = 2.0 \times 10^4$ cm^{-3} and typical radius of 5 pc (10 pc) in the Cloverleaf disk would amount to the measured molecular mass and have a column density, in each clump, of $N_{\rm H} = 3.09 \times 10^{23}$ cm^{-2} (6.2×10^{23} cm^{-2}), corresponding to $A_{\rm V} = 150$ (300). With the same geometry considered above, this distribution of molecular clouds gives an area filling factor of $\phi_{\rm ff} = 2.1$ (1.1).

Cosmic-rays Enhanced ionization rates of molecular hydrogen by cosmic-ray particles produced in supernovae may play a role in heating of molecular gas in starburst galaxies (e.g., Bradford et al. (2003) and Meijerink et al. (2011)), and we explore this possibility in the Cloverleaf. As outlined in Suchkov et al. (1993), if one assumes that the rate of supernovae is proportional to a galaxy's SFR, it follows that the number density of cosmic-rays in a star-forming region, $n_{\rm CR}$, scales with the local SFR density. Assuming that the cosmic-ray ionization rate, $\xi_{\rm CR}$, is proportional to the cosmic-ray particle number density, then $\xi_{\rm CR} \propto n_{\rm CR} \propto \left(\frac{\rm SFR}{D^2}\right)$, and the ratio of cosmic-ray ionization rates for two starburst galaxies is equivalent to the ratio of their star formation rate surface densities. We then solve for the expected cosmic-ray ionization rate in the Cloverleaf, $\xi_{\rm CR}^{\rm clover}$, by scaling from the estimated ionization rate in M 82, $\xi_{\rm CR}^{\rm M82}$:

$$\xi_{\rm CR}^{\rm clover} = \xi_{\rm CR}^{\rm M82} \left(\frac{D_{\rm M82}}{D_{\rm clover}}\right)^2 \left(\frac{\rm SFR_{clover}}{\rm SFR_{M82}}\right) \qquad (1.3.7)$$

The cosmic-ray density in M 82 has been measured as ~ 500 times the density in the Galaxy (VERITAS Collaboration et al. 2009), so we scale $\xi_{\rm CR}^{\rm M82}$ by the same amount, such that $\xi_{\rm CR}^{\rm M82} = 500\times$ (2–7 $\times 10^{-17}$ s^{-1}) = 1–4$\times 10^{-14}$ s^{-1}. The lower and upper bounds in the allowable range indicate the Galactic cosmic-ray ionization rates as measured by Goldsmith & Langer (1978) and van Dishoeck & Black

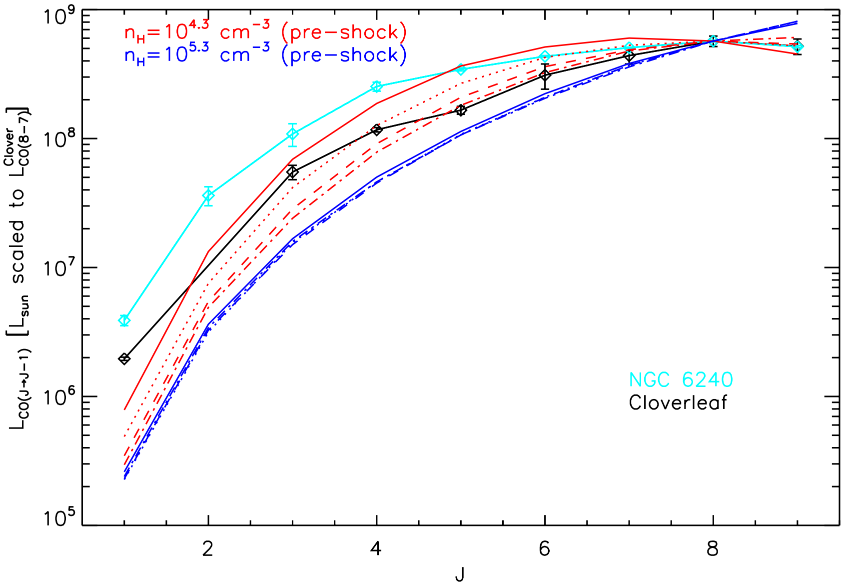

Figure 1.14: Predicted CO SLEDs for C-type shock models (Flower & Pineau Des Forêts 2010) and observed CO SLED for the Cloverleaf (black curve). Red and blue curves correspond to pre-shock densities of $n_{\rm H} = 2 \times 10^4$ cm^{-3} and 2×10^5 cm^{-3}, respectively. Different linestyles indicate shock velocities of 10 km s^{-1} (*solid*), 20 km s^{-1} (*dotted*), 30 km s^{-1} (*dashed*), and 40 km s^{-1} (*dot-dashed*). Models are normalized such that luminosities of the $J = 8 \rightarrow 7$ transition match the observed luminosity for that transition in the Cloverleaf. For reference, the measured CO SLED for NGC 6240 (cyan curve)—which was reproduced in Meijerink et al. (2013) using a C-type shock model (not shown) with $n_{\rm H} = 5 \times 10^4$ cm^{-3} and $v_{shock} = 10$ km s^{-1}—is also plotted.

(1986), respectively. Cosmic-ray particles deposit roughly 20 eV of energy per H_2 ionization, so the amount of energy deposited into the molecular gas in M 82 is 3–10$\times 10^{-25}$ erg s^{-1} per H_2 ionization.

After comparing the star-formation rate surface densities for M 82 and the Cloverleaf, and applying Equation 1.3.7, we find that the cosmic-ray ionization rate is roughly 9 times greater in the Cloverleaf than in M 82. The energy deposition rate per H_2 ionization is then 3–9$\times 10^{-24}$ erg s^{-1} for the Cloverleaf. The observed CO cooling implies that a supply of 8.5×10^9 $M_\odot$ ($\approx 5 \times 10^{66}$ H_2 molecules) of molecular gas radiates 1.3×10^{43} erg s^{-1}, which equals 3×10^{-24} erg s^{-1} per H_2 molecule, so we conclude that cosmic-ray ionization could provide sufficient heating for the molecular gas in the Cloverleaf disk.

1.4 Discussion

1.4.1 Molecular clump sizes and spatial distribution

We have argued in Section 1.3.3 that the PDR gas and the CO-bright XDR gas are roughly coextensive in a ~ 1.3 kpc-wide disk based on (1) the ability of predicted

CO, [CII]158μm, [OI]63μm surface brightnesses from theoretical XDR and PDR models to reproduce observed fluxes, and (2) similar distributions of the spatially resolved CO(7-6) and 122μm continuum maps (with assumption that the 122μm continuum is produced by SF). This scenario implies that the SF, which provides UV-heating for the PDRs, is not inhibited by exposure to strong X-ray fluxes. It is important to note, however, that the *Herschel* line fluxes represent aggregate emission across the Cloverleaf system, and thus do not preclude the possibility that the CO-bright XDR gas is actually at smaller radius—which would imply that it is illuminated by stronger X-ray fields than the PDRs. While the construction of a more detailed model of the disk structure is not justified given the limitation of the current dataset, there are plausible scenarios that would allow for SF to occur in gas exposed to moderate to high X-ray fluxes, which we now examine.

For instance, it is possible that SF is occurring in regions which are more highly shielded than the CO-bright XDR, as may occur, for example, in an azimuthally non-uniform X-ray field. Alternatively, the star-forming regions could be shielded by local gas, such as in a dense envelope of molecular gas. The hydrogen gas density required to attenuate X-ray flux by a factor of 22 or more is readily achieved by the gas densities indicated by CO observations, which are in excess of 10^4 cm^{-3}, and possibly as high as 10^5 cm^{-3}. If we let $n_{\rm H} = 3 \times 10^4$ cm^{-3}, then a spherical molecular gas clump that could potentially host SF would have a column of attenuating hydrogen of $N_{\rm H,att} = 6.5 \times 10^{23}$ cm^{-2} at a clump radius of 7 pc. The presence of $\approx 7,900$ such clumps would total the observed molecular gas mass of the Cloverleaf, namely, $M_{\rm H_2} \sim 8.5 \times 10^9$ M$_\odot$, and gives rise to $\phi_{\rm ff} = 1$ when distributed in the disk of outer radius 650 pc and inner radius 180 pc. While the area filling factor may be high for this clump distribution, the volume filling factor would be only $\sim 6\%$, providing a relatively unobstructed path for X-rays to reach each molecular clump once it leaves the foreground screen in front of the AGN. Smaller (larger) clumps have sub- (greater than) unity area filling factors, which lead to insufficient (excessive) X-ray illuminated gas to produce the observed CO, at least in the existing model.

1.4.2 Comparison with high-redshift and local systems

Co-spatial SF and SMBH accretion at sub-kpc scales has been suggested for another molecular gas-rich quasar at higher redshift, namely, APM 08279+5255 ($z = 3.9$). In that system, the CO gas is also spatially resolved to be concentrated within a short distance of the AGN—$R = 550$ pc—and similarly emits a large CO surface brightness that is best-matched to an XDR component of comparable size to the full extent of the molecular disk (Bradford et al. 2011). Observations of high-order rotational transitions of water molecules in APM 08279, coupled with high dust temperatures throughout the disk that are uncharacteristic of XDRs, suggest that SF is ongoing in the XDR, as well, if radiative pumping from FIR photons of re-processed starlight from dust is responsible for exciting the water as suggested by Bradford et al. (2011) and van der Werf et al. (2011).

At lower redshift, the local ULIRG Markarian 231 most closely resembles the Cloverleaf in terms of its FIR luminosity and the dominance of the AGN in its overall energetics. Mrk 231 also exhibits an XDR contribution to the CO emission, but, unlike the Cloverleaf, this XDR is more centrally concentrated to the inner ~ 160 pc of the 550 pc molecular disk; the majority of the CO emission is emitted in spatially extended PDR components at $R > 160$ pc (van der Werf et al. 2010). The LIRG and composite starburst/AGN NGC 1068 is another local example where XDRs have been identified as the excitation mechanism for CO-emitting molecular gas (Hailey-Dunsheath et al. 2012; Spinoglio et al. 2012b), although the starburst component in that galaxy is modeled as being distributed in a ring at larger radius than the CO-bright XDR, which is distributed in a circumnuclear disk. With X-ray luminosities of $L_{\rm X}$(2–10 keV)$= 6 \times 10^{43}$ erg s^{-1} (Braito et al. 2004) for Mrk 231 and $L_{\rm X}$(2-10 keV)$= 10^{43} - 10^{43.5}$ erg s^{-1} (Colbert et al. 2002) for NGC 1068, the ratio of total CO-to-X-ray luminosity in each of these respective sources is 1×10^{-2} $(= \sum_{J=1}^{J=13} L_{\rm CO(J\rightarrow J-1)}/L_{\rm X})$ and $2 - 6 \times 10^{-3}$ $(= \sum_{J=1}^{J=22} L_{\rm CO(J\rightarrow J-1)}/L_{\rm X})$; while for the Cloverleaf, this ratio is 1.2×10^{-3}.

Additionally, we note that the measured [CII]-to-FIR continuum luminosity ratio of 3×10^{-3} in the Cloverleaf is consistent with observations of this ratio in a sample of quasars and submm galaxies with $L_{\rm FIR} > 10^{12}$ L$_\odot$ at $z \sim$ 1–3 as compiled, e.g., in Carilli & Walter (2013) (cf. their Figure 6). The observed ratios at this redshift range are consistent with moderate FUV fluxes of order $G_0 \sim 10^3$, characteristic of kpc-scale star formation.

1.5 Conclusions

Observations of the dominant PDR cooling lines [CII]158μm and [OI]63μm have allowed us to assess the physical conditions—parametrized by their gas density and the impingent FUV flux—prevalent in atomic gas heated by stellar populations in the Cloverleaf. After subtracting expected contributions to the measured [CII]158μm flux from the NLR and stellar HII regions, we find that K06 PDR models with $n_{\rm H} = 5.6 \times 10^3$ cm^{-3} and $G_0 = 10^3$ reproduce the observed diagnostic flux ratios $F_{\rm [OI]}/F_{\rm [CII]}$ and $\left(F_{\rm [CII]} + F_{\rm [OI]}\right)/F_{\rm FIR}$. These moderate conditions, however, contradict the findings from PDR models derived exclusively from CO diagnostic ratios, which instead favor gas densities $n_{\rm H} > 10^5$ cm^{-3} and imply greater emission in [OI]63μm and less emission in [CII]158μm than what is seen in the Cloverleaf. Thus, we conclude that UV heating from local star formation is not sufficient to explain both the observed atomic line and CO luminosities, and suggest that an additional X-ray heating component from the AGN is required to account for a complete census of measured line emission.

Based on predicted [CII]158μm and [OI]63μm XDR surface brightnesses for a range of XDR models that reproduce the measured CO surface brightness, we have identified a set of viable XDR models which do not overproduce the observed [OI]63μm or [CII]158μm fluxes, and which can be combined with PDR models to inform global ISM conditions in the Cloverleaf molecular disk. Due to broad likelihood distributions of the derived molecular gas densities, temperatures, and thermal pressures from previously published results of CO modeling, as well as uncertainties in the area filling factor of the gas and the precise contribution of the Cloverleaf starburst to the total CO emission, we have considered a correspondingly expansive parameter space of combined XDR and PDR models in our analysis.

The general picture of the Cloverleaf ISM that emerges from our composite model is one where the [CII]158μm and [OI]63μm line emission is produced primarily within PDRs and HII regions of a 1.3-kpc wide starburst, which is embedded in a denser XDR component that is the dominant source of heating for the CO gas. (We note, however, that if densities and X-ray fluxes in the CO-constrained XDR are large, then this component can provide the majority (up to 70-80%) of observed [OI]63μm, but is still subdominant in terms of [CII]158μm emission relative to PDRs.) The fact that the star-forming PDR and HII region gas is co-spatial with the XDR—and within ~ 650 pc of the SMBH—provides strong evidence that star formation is ongoing while immersed in a strong X-ray radiation field provided by the nearby AGN.

Table 1.1: Line fluxes and luminosities for the Cloverleaf

Line Transition	$\lambda_{\rm rest}$ [μm]	Observed Flux [10^{-18} W m^{-2}]	Error [10^{-18} W m^{-2}]	Corrected Flux[a] [10^{-18} W m^{-2}]	Intrinsic Luminosity[b] [10^{9} L$_\odot$]	Reference[c]
[CII] ^{2}P$_{3/2}$ $\rightarrow$^{2}P$_{1/2}$	157.7	13.3	3.51	14.6	18.9	U16
[OI] ^{3}P$_1$ $\rightarrow$^{3}P$_2$	63.2	11.1	1.30	16.3	21.2	U16
[OIII] ^{3}P$_1$ $\rightarrow$^{3}P$_0$	88.4	$<$ 10.8 (95% CL)	-	-	$<$ 13.9	U16
[OIII] ^{3}P$_2$ $\rightarrow$^{3}P$_1$	51.8	2.67	0.521	4.65	6.00	U16
[SiII] ^{2}P$_{3/2}$ $\rightarrow$^{2}P$_{1/2}$	34.8	3.18	0.421	9.29	12.0	U16
[OIV] ^{2}P$_{3/2}$ $\rightarrow$^{2}P$_{1/2}$	25.9	$<$ 4.05 (95% CL)	-	-	$<$ 5.23	U16
[SIII] ^{3}P$_1$ $\rightarrow$^{3}P$_0$	33.5	$<$ 3.25 (95% CL)	-	-	$<$ 4.20	U16
[FeII] ^{6}D$_{7/2}$ $\rightarrow$^{6}D$_{9/2}$	26.0	$<$ 3.36 (95% CL)	-	-	$<$ 4.34	U16
[NII] ^{3}P$_2$ $\rightarrow$^{3}P$_1$	121.8	2.4	0.40	2.70	3.49	F11
CO $J = 1 \rightarrow 0$	2602.17	0.00150	0.0000432	-	0.00196	R11
CO $J = 3 \rightarrow 2$	866.98	0.043	0.0055	-	0.055	W03
CO $J = 4 \rightarrow 3$	650.25	0.0912	0.0035	-	0.117	Ba97
CO $J = 5 \rightarrow 4$	520.24	0.130	0.0092	-	0.166	Ba97
CO $J = 6 \rightarrow 5$	433.57	0.240	0.053	-	0.31	B09
CO $J = 7 \rightarrow 6$	371.66	0.343	0.048	-	0.44	B09
CO $J = 8 \rightarrow 7$	325.23	0.444	0.041	-	0.57	B09
CO $J = 9 \rightarrow 8$	289.13	0.406	0.056	-	0.52	B09
PAH	6.2	1.36	-	-	19.4	L07
PAH	7.7	5.54	-	-	78.8	L07
$L_{\rm FIR}$(40μm-120μm) [10^{13} L$_\odot$]				0.54	W03	
$L_{\rm Bol}$ [10^{13} L$_\odot$]				7.0	L07	
$L_{\rm CO}/M_{\rm H_2}$ [L$_\odot$ M$_\odot$$^{-1}$]				0.39	B09	

---

[a] Line fluxes (excluding upper limits) have been corrected for extinction according to the mixed dust model from Li & Draine (2001), as described in the main text.

[b] Luminosities reported here have been downscaled with the appropriate lensing magnification factor, $\mu = 11$.

[c] Abbreviated references include this work (denoted as U16), Ferkinhoff et al. (2011a) (F11), Riechers et al. (2011a) (R11), Weiß et al. (2003) (W03), Barvainis et al. (1997) (Ba97), Bradford et al. (2009a) (B09), and Lutz et al. (2007) (L07).

Table 1.2: ISM partitioning of measured line fluxes

Line i	$L_i/L_{\rm FIR}$	$L_i^{\rm M82}/L_{\rm FIR}^{\rm M82}$	$\alpha_{i,\rm HII}$	$\alpha_{i,\rm NLR}$	$\alpha_{i,\rm XDR}$					$\alpha_{i,\rm PDR}$				
					Case I[a]	Case II[b]	Case III[c]	Case IV[d]	Case V[e]	Case I	Case II	Case III	Case IV	Case V
[CII]	3.5×10^{-3}	3.2×10^{-3}	0.20	0.20	0.18 (0.13)[f]	0.24 (0.17)	0.36 (0.26)	0.20 (0.14)	0.050 (0.035)	0.42 (0.47)	0.27 (0.36)	0.24 (0.34)	0.40 (0.46)	0.55 (0.57)
[OI]63	3.9×10^{-3}	2.7×10^{-3}	–	–	0.24 (0.17)	0.11 (0.08)	0.70 (0.51)	0.77 (0.56)	0.018 (0.013)	0.76 (0.83)	0.94 (0.96)	0.30 (0.49)	0.24 (0.17)	0.98 (0.99)
[NII]122	6.4×10^{-4}	5.7×10^{-4}	0.80	0.20	–	–	–	–	–	–	–	–	–	–
[OIII]52	1.1×10^{-3}	9.7×10^{-4}	0.87	0.13	–	–	–	–	–	–	–	–	–	–
PAH 6.2μm	3.6×10^{-3}	5.4×10^{-4}	–	–	–	–	–	–	–	–	–	–	–	–
PAH 7.7μm	0.015	0.014	–	–	–	–	–	–	–	–	–	–	–	–

---

[a] $n_{\rm H} = 10^5$ cm^{-3}, $R = 600$ pc
[b] $n_{\rm H} = 5 \times 10^4$ cm^{-3}, $R = 1000$ pc
[c] $n_{\rm H} = 10^5$ cm^{-3}, $R = 500$ pc
[d] $n_{\rm H} = 2 \times 10^5$ cm^{-3}, $R = 350$ pc
[e] $n_{\rm H} = 2 \times 10^5$ cm $^{-3}$, $R = 1430$ pc
[f] Parenthetical values have been calculated with the assumption of an M82-like starburst.

Chapter 2

Measuring galaxy clustering and the evolution of [CII] mean intensity with Far-IR line intensity mapping during $0.5 < z < 1.5$

2.1 Introduction

Charting the history throughout cosmic time of star formation, black hole growth, and the properties of the galaxies that host these activities is at the root of many astronomical measurements currently underway. A fundamental limitation of most galaxy surveys—both photometric and spectroscopic—is that they are flux-limited, translating to a threshold luminosity below which galaxies are not included in the observations. This incompleteness is particularly true in the far-infrared/submillimeter wavelengths, which seem to have dominated the historical energy output of galaxies (Planck Collaboration et al. 2013). With the exception of ALMA, which is not well-suited to large surveys, telescopes remain sensitivity-challenged in this regime.

Intensity mapping by its nature probes all sources of emission, whether point-like or diffuse, luminous or faint. We focus here on three-dimensional (3-D) line intensity mapping, also known as tomographic mapping, using the spatial and spectral dimensions. A 3-D intensity mapping survey targeting a spectral line at a range of frequencies naturally produces a data cube in which redshift, thus line-of-sight distance is automatically encoded. The 3-D fluctuations in line emission are then studied in Fourier space with the power spectrum. This approach expands upon recent works that utilize the fluctuations in emission (rather than individually detected galaxies with luminosities down to a survey's flux limit) to study the properties of dusty, star-forming galaxies (DSFGs) with continuum data. These studies, using *P(D)* (Glenn et al. 2010; Béthermin et al. 2011) or a 2-D power spectrum (Viero et al. 2012; Planck Collaboration et al. 2013) analysis, have already shed light on some aspects (such as galaxy number counts, spatial clustering, and cosmic evolution of IR luminosity density) of the bulk of these systems during the peak of cosmic star formation, but they are limited by source confusion or uncertainties associated with the lack of redshift information. Redshift ambiguities can be removed to some extent with galaxy-by-galaxy observations with the interferometers ALMA or NOEMA, or with an instrument like X-Spec, a proposed multi-object spectrometer for CCAT. However, the interferometer surveys will be expensive and will cover very little sky, and the CCAT surveys, though faster, will not reach the faintest galaxies in the luminosity function (Bradford et al. 2009b). Power spectrum treatment of the 3-D datasets naturally combines the redshift precision of spectral measurements, while including all sources of emission, and can be carried out with an instrument that does not require exquisite point-source sensitivity.

Atomic (Gong et al. 2012; Visbal et al. 2011; Suginohara et al. 1999) and molecular (Lidz et al. 2011a; Gong et al. 2011) transitions—such as the 21-cm spin flip transition from H^o, CO rotational lines, and [CII]158μm—have been investigated as candidates for intensity mapping experiments during the Epoch of Reionization (EoR) and afterward (Pullen et al. 2013a,b; Breysse et al. 2014, for CO lines and Lyα). Of these, the neutral hydrogen case is undoubtedly the most developed in terms of its standing in the literature (cf. Morales & Wyithe (2010) for a review) and in the experimental arena (e.g., PAPER (Parsons et al. 2013), MWA (Tingay et al. 2013)) because intensity mapping is the only means of studying the intergalactic HI light. [CII] later emerged as an EoR intensity mapping candidate since it both offers a way to probe the clustering of sources from the faint-end of the luminosity function, and provides an opportunity for cross-correlation with the HI datasets (Gong et al. 2012).

In addition to tracing large-scale structure, [CII] also contains astrophysical information about the conditions in star-forming galaxies. With an ionization potential of 11.6 eV, it arises in both ionized and neutral atomic gas. Empirically, it is an important coolant, often the brightest single line in the spectrum of a star-forming galaxy, emitting as much as 0.5–1% of the total far-IR luminosity (Malhotra et al. 1997; Luhman et al. 1998; Stacey et al. 2010b; Graciá-Carpio et al. 2011). The ratio of the [CII] luminosity to the total bolometric luminosity can be used as a diagnostic tool that provides: (1) a measure of the star-formation activity, (2) a measure of the spatial extent (or “mode”) of star formation, and (3) an AGN/starburst discriminant (Hailey-Dunsheath et al. 2010a; Stacey et al. 2010b; Graciá-Carpio et al. 2011; Sargsyan et al. 2012; Díaz-Santos et al. 2013).

The broader suite of far-IR lines probes all phases of the interstellar medium, and the negligible optical depth of galaxies at far-IR wavelengths ensures that even the most heavily embedded regions where stars form and black holes grow are revealed. For the atomic and ionized medium, the key far-infrared emission lines are those of C, N, & O (e.g., [OI]63μm, 146μm, [CII]158μm, [OIII]52μm, 88μm, [NIII]57μm, and [NII]122μm, 205μm). The emitting species cover more than an order of magnitude in ionization potential and they strongly constrain the density and temperature of the ionized and neutral gas, and the strength and hardness of the interstellar radiation field. These physical parameters then reveal the relative importance of the black hole vs. the hot young stars to the overall energy budget, and constrain the stellar effective temperatures (Rubin 1985; Dale et al. 2004; Colbert et al. 1999b; Malhotra et al. 2001; Ferkinhoff et al. 2011b; Lebouteiller et al. 2012, e.g.). The suite of carbon, oxygen and nitrogen transitions also measure abundances (Garnett et al. 2004; Lester et al. 1987; Nagao et al. 2011).

Line intensity mapping experiments targeting the fine-structure metal lines at post-Reionization redshifts can offer a proof of principle of the approach, similar to measurements of the HI autocorrelation power spectrum at $z \sim 0.8$ (Chang et al. 2010; Switzer et al. 2013), and provide a complete census of galaxies during an important phase in the star formation history of the Universe. While the redshifted far-IR lines are not accessible from the ground in this redshift range, a balloon- or space-borne intensity mapping experiment with broad wavelength coverage can in principle measure the mean intensities of these lines through cosmic time, thereby charting the evolution of the star-formation conditions in galaxies in an absolute, aggregate sense. Here we consider a first step in this direction: a measurement of [CII] autocorrelation in multiple bins through the $0.5 < z < 1.5$ epoch. [CII] and far-IR lines in general ought to be particularly well-suited to this time frame, as $z \sim 1.5$ is believed to be the peak in the dust attenuation in galaxies, when roughly 80% of the cosmic star formation rate density is obscured and captured only in the infrared emission of re-processed starlight by dust grains (Burgarella et al. 2013b). From a practical standpoint, [CII] in this epoch is relatively free of interloper lines, as will be shown.

The organization of this paper is as follows. We have estimated the mean intensity for a suite of fine-structure IR emission lines, including the [CII] line, based on empirical IR luminosity functions and line-to-IR luminosity correlations, and present these results in the context of a power spectrum model in Section 2. In Section 3, we envision suitable platforms for conducting the [CII] intensity mapping experiment and discuss the feasibility of detecting the [CII] power spectra in terms of the signal-to-noise ratio (SNR). From the predicted power spectra, we provide estimates for accuracy in measuring the mean [CII] intensity as a function of redshift. To better assess the value of intensity mapping studies in the case of [CII] at moderate redshifts, and of intensity mapping experiments in general, we compare in Section 4 the performance of the intensity mapping approach against spectroscopic galaxy surveys that rely on individual detections of sources to measure the total emission and power spectrum. In particular, we examine the effects of variations in luminosity function shape, aperture diameter (and, consequently, voxel size), and experimental noise on the ability of each observational method to measure the power spectrum and provide a complete view of the galaxy population.

2.2 Predictions for Far-IR Line Power Spectra

2.2.1 Relationship Between Galaxy Populations and Fluctuation Power

The complete autocorrelation power spectrum of a given far-IR fine-structure line i as a function of wavenumber k, $P_{i,i}(k,z)$, can be separated into power from the clustering of galaxies, $P^{clust}_{i,i}(k,z)$ and a Poisson term arising from their discrete nature, $P^{shot}_{i,i}(z)$. We compute the full nonlinear matter power spectrum, $P_{\delta,\delta}(k,z)$, using the publicly available code HALOFIT+ (http://camb.info), which has been the standard tool for predicting matter power spectra upon its success in fitting state-of-the-art dark matter simulations over a decade ago (Smith et al. 2003). The clustering component of the line power spectrum is then written as (Visbal & Loeb 2010)

$$P^{clust}_{i,i}(k,z) = \bar{S}_i^2(z)\bar{b_i}^2(z)P_{\delta\delta}(k,z). \tag{2.2.1}$$

Here we implicitly assume that the fluctuations in line emission trace the matter power spectrum with some linear bias, $\bar{b}_i(z)$, but note that we use the full nonlinear matter power spectrum. This should be an adequate approximation for our study, since the Poisson term (see Equation 2.2.3) will dominate on small-scales where the non-linearities become significant. Figure 2.1 compares the nonlinear $z = 0$ dark matter power spectrum to the linear power spectrum, and also shows the contributions to non-linear clustering power from correlations between and within dark matter halos, i.e., the so-called 2-halo and 1-halo terms. For our target redshift range and likely [CII] emitters, $\bar{b}_i$ is reasonably well-constrained to be between 2 and 3 (Cooray et al. 2010; Jullo et al. 2012), so we have assumed a single bias at each redshift. A more sophisticated model would allow for variation of the source bias with the host halo mass—as shown in Figure 2.2—and, thus, line luminosity after adopting a relation between halo mass and line luminosity. It should be straightforward to be rescale the results for other assumptions about bias.

The mean line intensity, $\bar{S}_i(z)$, in units of Jy sr^{-1}, can be calculated as

$$\bar{S}_i(z) = \int \mathrm{d}n_i \frac{L_i}{4\pi D_L^2} y_i D_{A,co}^2, \tag{2.2.2}$$

where the integration is taken with respect to n_i, the number of galactic line emitters per cosmological comoving volume element. The factor y_i is the derivative of the comoving radial distance with respect to the observed frequency, i.e. $y = d\chi/d\nu = \lambda_{i,rest}(1+z)^2/H(z)$, and $D_{A,co}$ is the comoving angular distance.

Finally, the shot noise component of the total line power spectrum—with the same units as the clustering term, namely, Jy^2 sr^{-2} (Mpc h^{-1})^3—takes the form

$$P^{shot}_{i,i}(z) = \int \mathrm{d}n_i \left(\frac{L_i}{4\pi D_L^2}\right)^2 \left(y_i D_{A,co}^2\right)^2. \tag{2.2.3}$$

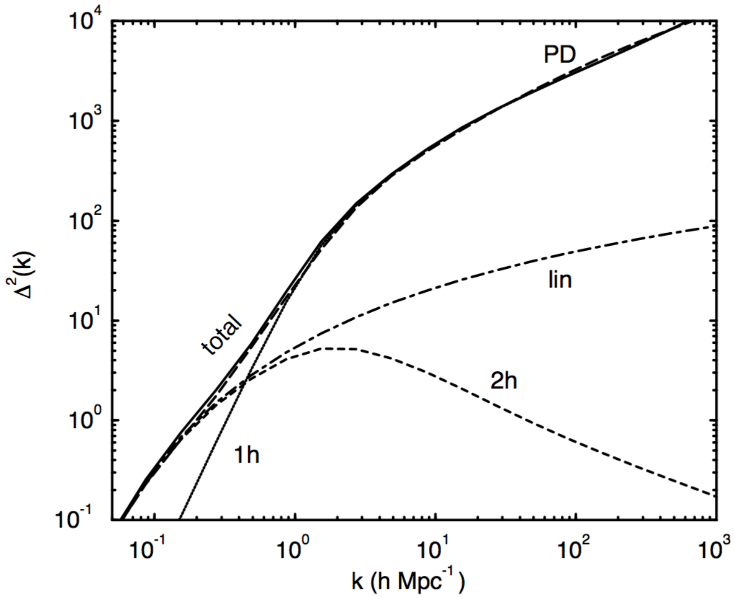

Figure 2.1: Dimensionless, full nonlinear dark matter power spectrum, $\Delta^2(k) = k^3 P_{\delta,\delta}(k)/(2\pi^2)$ (solid curve, labeled "total"). Contributions to the total power from 1-halo and 2-halo terms are also shown and labeled. The prediction from linear theory is also shown as the dot-dashed curve. Note that the linear power spectrum closely resembles the 2-halo term on large-scales, and is thus an adequate representation of the actual power at low wavenumbers. Figure from Cooray & Sheth (2002).

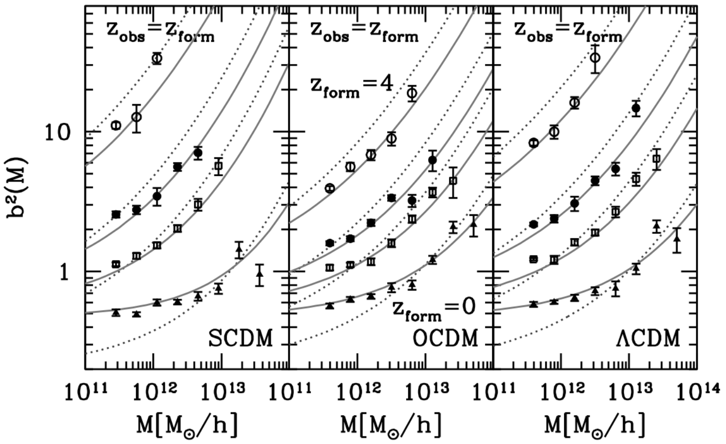

Figure 2.2: Halo bias as a function of halo mass, as calculated for the Sheth-Tormen (solid curves) and Press-Schechter (dotted curves) halo mass functions, and for cosmologies where $\Omega_0 = 1$, $\Omega_\Lambda = 0$, and $h = 0.5$ (SCDM; left panel); $\Omega_0 = 0.3$, $\Omega_\Lambda = 0$, and $h = 0.7$ (OCDM; middle panel); and $\Omega_0 = 0.3$, $\Omega_\Lambda = 0.7$, and $h = 0.7$ (ΛCDM; right panel). The relation between halo bias and mass is shown at four redshifts, $z_{\text{form}} = 4, 2, 1,$ and 0 (from top to bottom), corresponding to the formation of the virialized dark matter halo. Note that the increase in halo bias with halo mass indicates that massive halos follow the dark matter distribution more closely than less massive ones. Figure from Cooray & Sheth (2002).

2.2.2 Calculating IR line volume emissivity

The number density of line emitters and the line luminosity that appear in equations (2) and (3) can be derived by a variety of methods. In earlier papers on intensity mapping of molecular and fine-structure emission lines at high redshift (z $\gtrsim$ 6), one approach involved using the dark matter halo mass function in lieu of the line emitter density (and invoking a one-to-one correlation between halos and galaxies, which is reasonable at high redshifts). The line luminosity, in turn, could be scaled according to the star formation rate, which was related to halo mass via a proportionality constant comprised of factors describing the fraction of baryons available for star formation, as well as the dynamical timescale for star formation and a duty cycle for emission. While this approach is perhaps justified for the very early Universe (given the lack of information about the galaxy luminosity function at high redshift), the situation at later times is better understood; we make use of empirical constraints on the $z \sim 1$ epoch from far-IR/submm number counts and observations of far-IR line emission in galaxies.

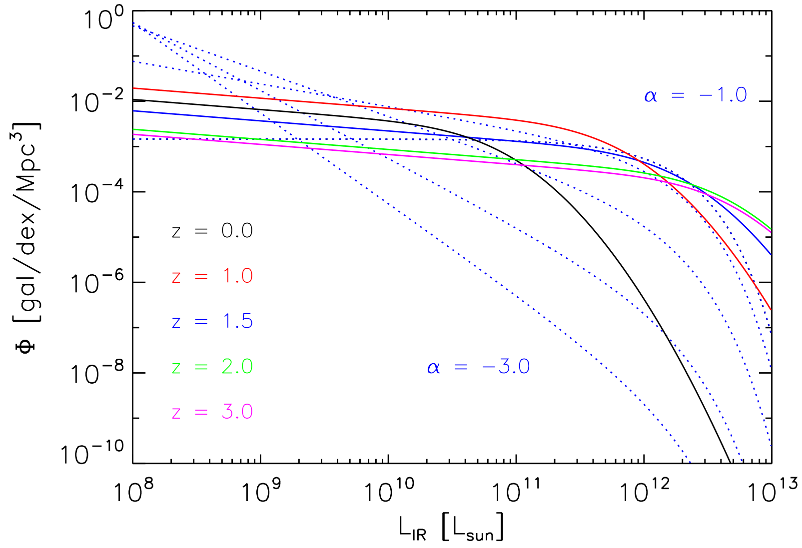

Figure 2.3: B11 IR luminosity function computed at $z = 0.0, 1.0, 1.5, 2.0,$ and 3.0 (solid black, red, blue, green, and magenta curves, respectively). Dotted blue curves represent Schechter-form luminosity functions—normalized such that the corresponding IR luminosity densities matches that of the B11 model—at $z = 1.5$ with faint-end slope (from top to bottom) $\alpha = -1.0, -1.5, -2.0, -2.5, -3.0$. Schechter functions with slopes steeper than $\alpha < -2.0$ are intended only for illustration.

We first employ the empirically-constrained, backwards-evolution model of the IR luminosity function $\Phi(L_{IR}, z)$ from Béthermin et al. (2011) (hereafter B11) to predict the number of galaxies with luminosity L_{IR} at a given redshift in some comoving volume of the Universe per logarithmic luminosity interval, i.e., $\frac{\mathrm{d}N(L_{IR},z)}{\mathrm{d}V\mathrm{dlog}_{10}L_{IR}}$ or $\frac{\mathrm{d}n_{IR}}{\mathrm{dlog}_{10}L_{IR}}$:

$$\begin{aligned}\Phi(L_{IR},z) = \Phi_*(z)\left(\frac{L_{IR}}{L_*(z)}\right)^{1-\beta} \\ \times \exp\left[-\frac{1}{2\xi^2}\log\left(1+\frac{L_{IR}}{L_*(z)}\right)\right]\end{aligned} \tag{2.2.4}$$

In the above expression, β and ξ set the faint-end power law slope and the bright-end Gaussian width, respectively, of the luminosity function. When evaluating Equation 2.2.4 at different redshifts and luminosities, we use the best-fit parameters from B11 (cf. their Table 1), and so keep $\beta = 1.223$ and $\xi = 0.406$. The parameters Φ_* and L_* follow a redshift evolution according to $\Phi_*(z) = 3.234 \times 10^{-3}\mathrm{gal/dex/Mpc^3}(1+z)^{r_\Phi}$ and $L_*(z) = 2.377 \times 10^{10}\mathrm{L_\odot}(1+z)^{r_L}$, where r_Φ and r_L also have a redshift-dependence, given by

$$r_\Phi = \begin{cases} 0.774, & z < z_{break,1} \\ -6.246, & z_{break,1} < z < z_{break,2} \\ -0.919, & z > z_{break,2} \end{cases}$$

$$\mathbf{r_L} = \begin{cases} 2.931, & z < z_{break,1} \\ 4.737, & z_{break,1} < z < z_{break,2} \\ 0.145, & z > z_{break,2} \end{cases}$$

The first break in redshift, $z_{break,1} = 0.879$, is a fitted parameter, whereas the second break is fixed at $z_{break,2} = 2.0$. In Figure 2.3, we plot the B11 luminosity function at several different redshifts up to $z = 3$.

To convert the infrared luminosity to a line luminosity, we apply the relation for L_i as a function of L_{IR} provided by Spinoglio et al. (2012a). (Working directly from the IR luminosity function, we do not include the population of IR-dark or IR-faint sources that nevertheless may contribute bright emission in the far-IR fine-structure lines (cf. Riechers et al. (2014)).) The fits in their paper were based on the diverse collection of ISO-LWS observations of local galaxies with luminosities between 10^8 and 10^{13} $\mathrm{L_\odot}$ from Brauher et al. (2008). For example, we reproduce below the relation for [CII]:

$$\log_{10}L_{\mathrm{[CII]}} = (0.89 \pm 0.03)\log_{10}L_{\mathrm{IR}} - (2.44 \pm 0.07), \tag{2.2.5}$$

indicating that [CII] is suppressed for higher luminosity systems. In general, the L_i-L_{IR} relations can be written in the form

$$\log_{10}L_i = (A \pm \sigma_A)\log_{10}L_{\mathrm{IR}} - (B \pm \sigma_B), \tag{2.2.6}$$

Slope, intercepts, and associated uncertainties described by the variables A, B, σ_A, and σ_B are summarized in Table 2.1 for a variety of IR lines.

Table 2.1: $L_i - L_{IR}$ relation variables from Spinoglio et al. (2012a)

Line i	A	σ_A	B	σ_B
[CII]158μm	0.89	0.03	2.44	0.07
[NII]122μm	1.01	0.04	3.54	0.11
[OI]63μm	0.98	0.03	2.70	0.10
[OIII]88μm	0.98	0.10	2.86	0.30
[OIII]52μm	0.88	0.10	2.54	0.31
[SiII]35μm	1.04	0.05	3.15	0.16
[SIII]33μm	0.99	0.05	3.21	0.14
[SIII]19μm	0.97	0.06	3.47	0.20
[NeII]13μm	0.99	0.06	3.26	0.20
[NeIII]16μm	1.10	0.07	3.72	0.23

The choice of using local L_i-L_{IR} relations for our study of $z \sim 1$ emitters may be unrealistic due to findings that suggest the so-called "deficit" in [CII] and other far-IR lines evolves with redshift such that the high-z counterparts to local systems do not exhibit suppressed far-IR line emission. The local IR relations then can be interpreted as underestimating emission of the fine-structure lines, since we likely overestimate the deficiency in the higher redshift, high luminosity systems of our model. While there are undeniably a number of uncertainties with the combined Béthermin-Spinoglio model, a simple extrapolation from the Hopkins & Beacom (2006b) star formation history clearly brackets our predicted [CII] intensity at the relevant redshifts, and so we adopt it as our fiducial model throughout this paper. In Section 4, however, we explore variations in the shape of the IR luminosity function and consider an alternative line-to-IR luminosity ratio (depicted as the dotted curves in Figure 2.3).

Next, it becomes possible to write the cosmic mean intensity and shot noise of the line, in units of Jy sr^{-1}, as a function of redshift based on the B11 luminosity function and Spinoglio et al. (2012a) $L_i - L_{\rm IR}$ relation as

$$\bar{S}_i(z) = \int \mathrm{dlog} L_{IR} \Phi(L_{IR}, z) \frac{f_i L_{IR}}{4\pi D_L^2} y D_{A,co}^2 \tag{2.2.7}$$

$$P_{i,i}^{shot}(z) = \int \mathrm{dlog} L_{IR} \Phi(L_{IR}, z) \left(\frac{f_i L_{IR}}{4\pi D_L^2} y D_{A,co}^2 \right)^2 \tag{2.2.8}$$

where the limits of integration are over the full range of expected IR luminosities, i.e. 10^8 to 10^{13} $L_\odot$, and f_i, i.e. $\frac{L_i(L_{IR})}{L_{IR}}$, is the fraction of IR luminosity emitted in line i, as computed from equation (3). In other words, we have written $\bar{S}_i$ and $P_{i,i}^{shot}(z)$ as the first and the second moments of the luminosity function.

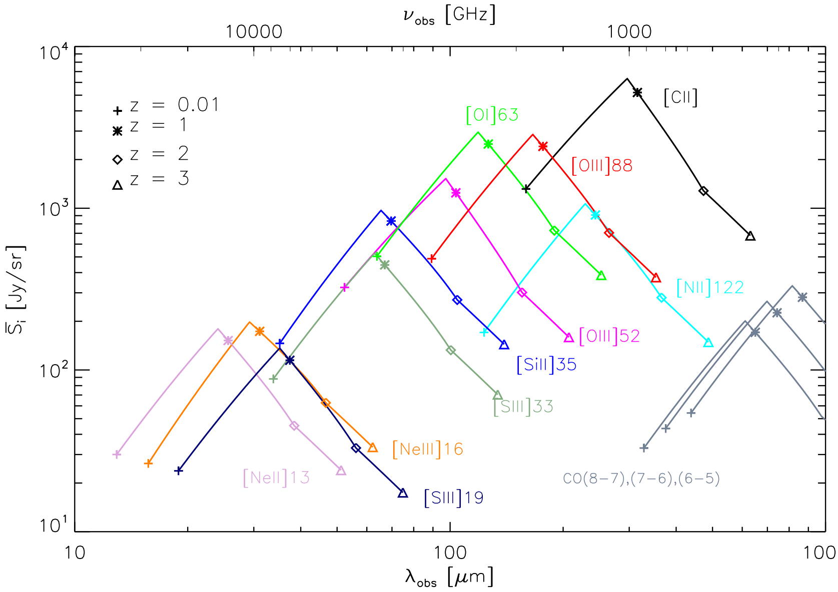

Figure 2.4: Intensity of fine-structure line emission as a function of observed wavelength for the empirical model based on the B11 luminosity function. Intensities of CO lines, which are not included in the IR luminosity relations from Spinoglio et al. (2012a), have been estimated using a luminosity scaling provided by Carilli (2011) for CO(1-0) and the relative intensities of the higher-J lines in Bothwell et al. (2013).

The resulting mean intensities for a variety of far-IR lines are plotted in Figure 2.4 as a function of redshift and observed wavelength. $\bar{S}_i$ vs λ_{obs} can be interpreted as identifying the dominant source of fluctuations, according to our model, of a given wavelength. As a specific example, if the target line of an observation is [OI]63μm at $z = 1$, it is necessary to distinguish between the target line and interlopers like [OIII]88μm from $z = 0.4$ and [OIII]52μm from $z = 1.4$, which contribute power at the observed wavelength. Visbal & Loeb (2010) showed how the cross spectra can be used to differentiate between a target line and a contaminating line (or "bad line", in their words), since emitters at different redshifts will be spatially uncorrelated. For the observed wavelengths of [CII], however, it is apparent from Figure 2 that, with the exception of contributions from [OIII]88μm and CO(8-7) near [CII] at $z \sim 0.01$ and $z > 2$, respectively, the [CII] line is relatively unaffected by interloper lines—a result of its luminosity and spectral isolation. It is for this practical reason, and for the astrophysical significance of [CII] mentioned in the Introduction, that we focus the remainder of this paper largely on [CII] emission.

2.2.3 [CII] Luminosity Functions and Expected Power Spectra

As laid out in Equations 2.2.1 and 2.2.2, $P^{clust}_{\text{[CII]},\text{[CII]}}$ is sensitive to intensity fluctuations from the full range of normal ($L_{IR} < 10^{11}$ L$_\odot$) to ULIRG-class ($L_{IR} > 10^{12}$ L$_\odot$)

systems because its amplitude is proportional to the mean line intensity, squared. The information contained in a power spectrum of individually detected galaxies is, in contrast to the line intensity mapping approach, necessarily limited to galaxies which are above a certain detection threshold, or $L_{IR,min}$. Figure 2.5 shows the integrated luminosity functions for [CII] in our model, which gives a sense of the depth that a galaxy survey must reach in order to completely probe the full integrated [CII] emission, i.e. all of $\bar{S}_i$. In this section, we examine the role of the various luminosity ranges on the amplitude of the observed [CII] power.

Power spectra at four representative redshifts ($z = 0.63, 0.88, 1.16$, and 1.48) comprised of the sources above a few different survey depths, or $L_{IR,min}$, are represented by Figure 2.6. (Note that we use $\Delta^2_{\mathrm{[CII],[CII]}} = k^3 P_{\mathrm{[CII],\,[CII]}}(k)/(2\pi^2)$ when plotting the power spectrum. In this notation, the factor k^3 cancels out the volumetric units of $P_{\delta,\delta}(k,z)$ and the integral of $\Delta^2_{\mathrm{[CII],[CII]}}$ over logarithmic k bins is equal to the variance in real space.) At these redshifts, the average linear bias has been assumed to take the observationally-motivated values of $\bar{b} = 2.0, 2.3, 2.6$, and 2.9, though, in general, the bias will likely depend on the galaxy luminosity provided that luminosity is correlated with halo mass. In this Figure, we see the clustering amplitude decrease as the IR detection threshold is raised from 10^8 $\mathrm{L}_\odot$ to 10^{12} $\mathrm{L}_\odot$. (Note that the reduction in the clustering amplitude is precisely the square of the factor of reduction in $\bar{S}_{\mathrm{[CII]}}$ plotted in Figure 2.5.) The level of decrease in clustering power as a result of raising $L_{IR,min}$ is most dramatic at the lower end of the redshift range of interest, when the luminosity function is represented mostly by normal galaxies and LIRGs. As ULIRGs rise to dominate the IR luminosity function at $z \sim 1.5$, the amplitude of the clustering component of $P_{\mathrm{[CII],[CII]}}(k,z)$ becomes relatively robust up to $L_{IR,min} \sim 10^{11}$ $\mathrm{L}_\odot$, implying that a large fraction of the fluctuations are captured at this depth; we infer from Figure 2.5 that, at $z = 1.48$, individually resolving galaxies at a depth of 6×10^{11} will recover half of the [CII] light, at which point the remaining power of unresolved fluctuations is 25% according to our model. For redshifts $z = 0.63, 1.16$ and 3.0, the corresponding depths to observe half-light are $\sim 10^{11}$, 2×10^{11}, and 10^{12} $\mathrm{L}_\odot$, respectively.

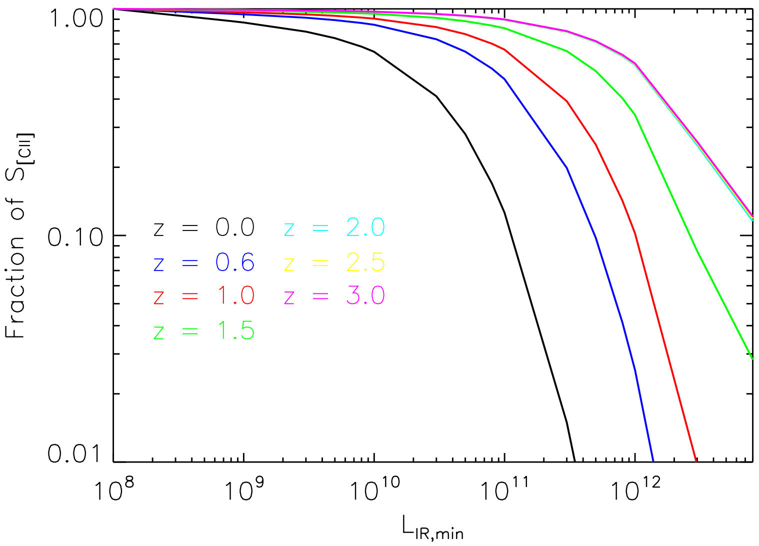

Figure 2.5: The fraction of total [CII] mean intensity as a function of lower limit in the luminosity function. Different color curves represent different redshifts, as labeled on the plot.

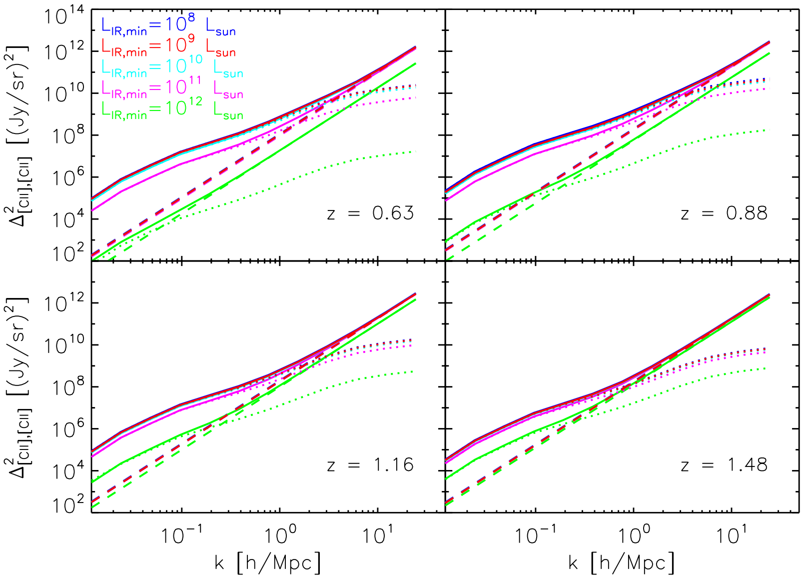

Figure 2.6: Predicted [CII] autocorrelation power spectra from $z = 0.63$ to $z = 1.48$. Blue, red, cyan, magenta, and green curves represent the power spectrum computed with a lower limit in the luminosity function corresponding to 10^8, 10^9, 10^{10}, 10^{11}, and 10^{12} $L_\odot$, respectively. Dotted curves indicate power from clustering (including contributions from linear and nonlinear terms), and dashed curves indicate the contribution from shot noise power.

2.3 The [CII] Power Spectrum

2.3.1 Observational Sensitivity to the Power Spectrum

We present in this section an assessment of detectability of the [CII] power spectrum. In order to quantify the observational sensitivity, we consider realistic experimental platforms with uninterrupted wavelength coverage in the redshift range of interest, namely, from 240 to 420 μm. This range is further divided into four bands to enable measuring redshift evolution in the signal. The width of each band has been set to span a redshift range of $\frac{\Delta z}{z_{center}} = 0.25$ to ensure there is no significant cosmological evolution within the band. Fiducial experimental parameters are summarized in Table 2.2, though we explore the effect of varying D_{ap} and A_{survey} on the signal-to-noise Ratio (SNR).

To define the survey depth, we adopt the quantity

$$f_{err} \equiv \frac{\sigma_N}{\sqrt{t_{obs}^{vox}}\bar{S}_i} \tag{2.3.1}$$

which we call the fractional error. It is simply the inverse of the SNR on the mean intensity in a single voxel. Here $\sigma_{\mathbf{N}}$ is the instrument sensitivity (noise equivalent intensity, or NEI, in units of Jy sr^{-1} s$^{1/2}$, $\bar{S}_i$ is the mean intensity and t_{obs}^{vox} is the observing time per voxel. (We take i = [CII] while the equations remain generally applicable to any line.) Error bar estimates and the total SNR for the power spectrum are calculated by assuming a spectrally flat noise power spectrum, so that the noise power in each voxel, P_N, is written as

$$\begin{aligned} P_N &= \sigma_N^2 \frac{V_{vox}}{t_{obs}^{vox}} \\ &= \left(f_{err}\bar{S}_i\right)^2 V_{vox} \end{aligned} \tag{2.3.2}$$

where V_{vox} is the volume of a voxel. The voxel volume is the product of pixel area, A_{pix} (in units of comoving Mpc^2 h^{-2}), and the line of sight distance along a spectral channel, $\Delta \mathrm{r}_{los}^{vox}$ (Mpc h^{-1}). A_{pix} depends on the telescope aperture and observed wavelength according to $A_{pix} = (\lambda_{i,obs}/D_{ap} \times D_A)^2$.

The variance of a measured k, $\sigma^2(k)$, is then written as

$$\sigma^2(k) = \frac{\left(P_{i,i}(k) + P_N(k)\right)^2}{N_{modes}(k)}, \tag{2.3.3}$$

where N_{modes} is the number of wavemodes that are sampled for a given k bin of some finite width Δlog(k). (We have chosen Δlog(k) = 0.3 for this analysis.) We restrict the mode counting to the upper-half plane in k-space, so as not to overestimate the number of independent modes sampled.

The total SNR, in turn, is calculated from the expression

$$SNR_{tot} = \sqrt{\sum_{bins} \left(\frac{P_{i,i}(k)}{\sigma(k)} \right)^2} \tag{2.3.4}$$

The expected [CII] power spectrum, with corresponding predictions for SNR, at the same redshifts from Figure 2.6 are shown in Figure 2.7. In calculating the power spectrum sensitivity for these power spectra, the two lowest line-of-sight modes and the lowest transverse mode are not included, since these modes will likely be compromised by the necessity of continuum foreground subtraction and beam-differencing in the fluctuation analysis. (The exact effect of continuum subtraction will need to be modeled via simulation.)

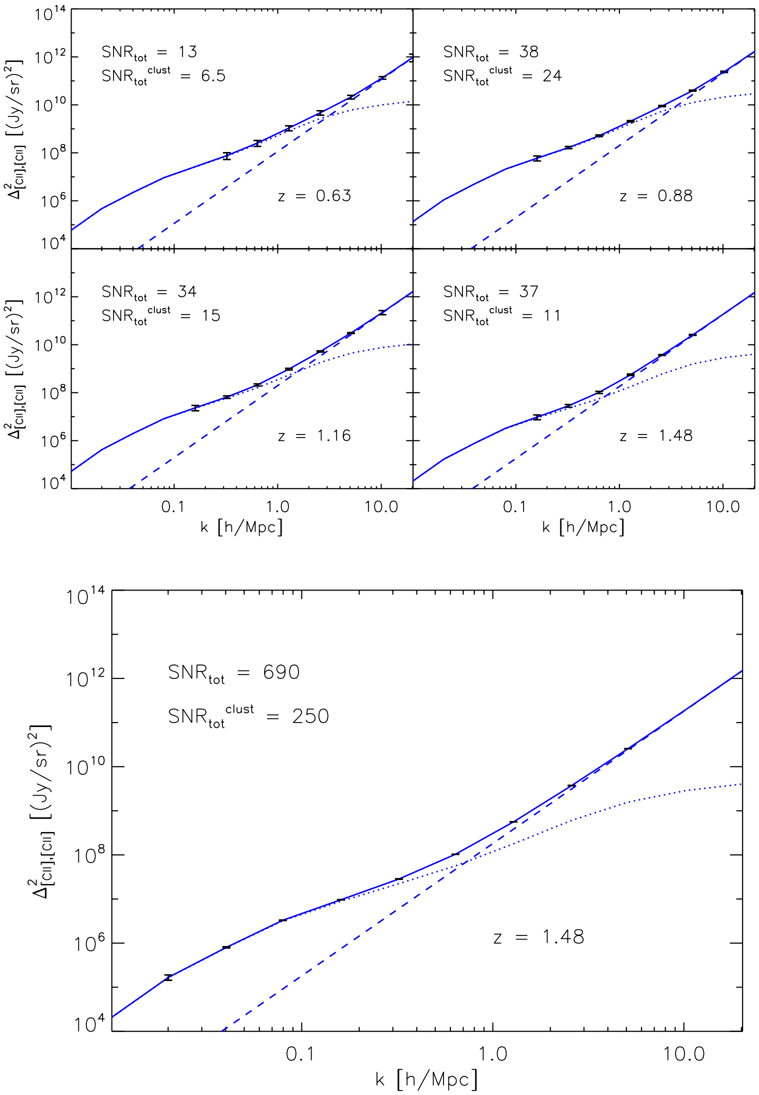

Figure 2.7: Top panel: Predicted [CII] power spectra with error bar estimates from $z = 0.63$ to $z = 1.48$ for the fiducial balloon experiment, and with a total observing time of 450 hours. Dotted curves indicate power from clustering (including contributions from linear and nonlinear terms), and dashed curves indicate the contribution from shot noise power. Bottom panel: [CII] power spectrum expected at $z = 1.48$ with error bar estimates for the fiducial cryogenic satellite experiment.

Table 2.2: Parameters for Envisioned Experimental Platforms

D_{ap} (m)	2.5			
$R = \lambda_{obs}/\Delta\lambda$	450			
Number of Spectral Channels	64			
$N_{instr}^{spatial}$ (instantaneous spatial pixels)	25			
t_{obs}^{survey} (hr)	450			
z_{cen} for [CII]	0.63	0.88	1.16	1.48
Wavelength Range (μm)	240-276	276-317	317-365	365-420
V_{voxel} (Mpc^3 h^{-3})	0.36	0.81	1.59	2.87
A_{pix} (Mpc^2 h^{-2})	0.044	0.096	0.19	0.35
Δr_{los}^{vox} (Mpc h^{-1})	7.8	7.8	7.7	7.5
$\bar{S}_{[CII]}$ (Jy sr^{-1})	4.56×10^3	6.33×10^3	4.05×10^3	2.55×10^3
	Atmospheric Balloon			
A_{survey} (deg^2)	1	1	1	1
σ_N (10^7 Jy sr^{-1} sec$^{1/2}$)	3.4	2.1	1.5	1.0
Line Sensitivity, S_γ (10^{-18} W m^{-2} sec$^{1/2}$)	15.8	11.3	9.20	7.10
f_{err}	160	63	61	56
	Cryogenic Satellite			
A_{survey} (deg^2)	1,000	1,000	1,000	1,000
σ_N (10^7 Jy sr^{-1} sec$^{1/2}$)	0.030	0.034	0.039	0.043
Line Sensitivity, S_γ (10^{-18} W m^{-2} sec$^{1/2}$)	0.139	0.185	0.240	0.306
f_{err}	45	32	50	77

Table 2.2 shows our instrument concepts. We specify a 25-beam grating spectrometer covering the 240-420 μm band, each with 64 $R = 450$ spectral channels operating near the photon background limit, illuminated with a 2.5-meter telescope. We consider a balloon experiment for which the photon background is due to 1% emissivity in the atmosphere (a conservative average value) and 4% in the telescope. A 450 hour integration (as might be obtained in a long duration balloon flight) over the 1 square degree with this system results in the σ_N, f_{err}, and line sensitivity values tabulated. We also consider a similar instrument on a cryogenic space-borne platform. The sensitivity in this case is obtained by specifying a detector sensitivity which is equal to the photon background noise, so that the quadrature sum is $\sqrt{2}$ times the photon noise. The photon background is taken to be due to the combination of zodiacal light, galactic dust, and a 6-K telescope telescope with 4% emissivity. This is an optimized instrument with advanced detectors – it is similar to the best case of the proposed BLISS instrument for SPICA (e.g., see Bradford et al. (2012)). As the tabulated depths indicate, the space-borne system is much more sensitive. Nevertheless, the balloon-borne experiment is capable of measuring the power spectrum with good sensitivity, and all error bars in this paper are based on the 450-hour balloon experiment, unless otherwise noted.

We find that the total power spectrum, including power from both shot noise and clustering, is observable using the balloon platform with SNR $>$ 10 at all examined redshifts; the clustering power, in turn, can be detected with SNR $>$ 10 in the redshift range from $z = 0.88 - 1.48$. From space, it becomes feasible to survey larger areas (~1,000 deg^2) and maintain high SNR on the order of 100. (See Figure 2.7 for calculated SNRs.)

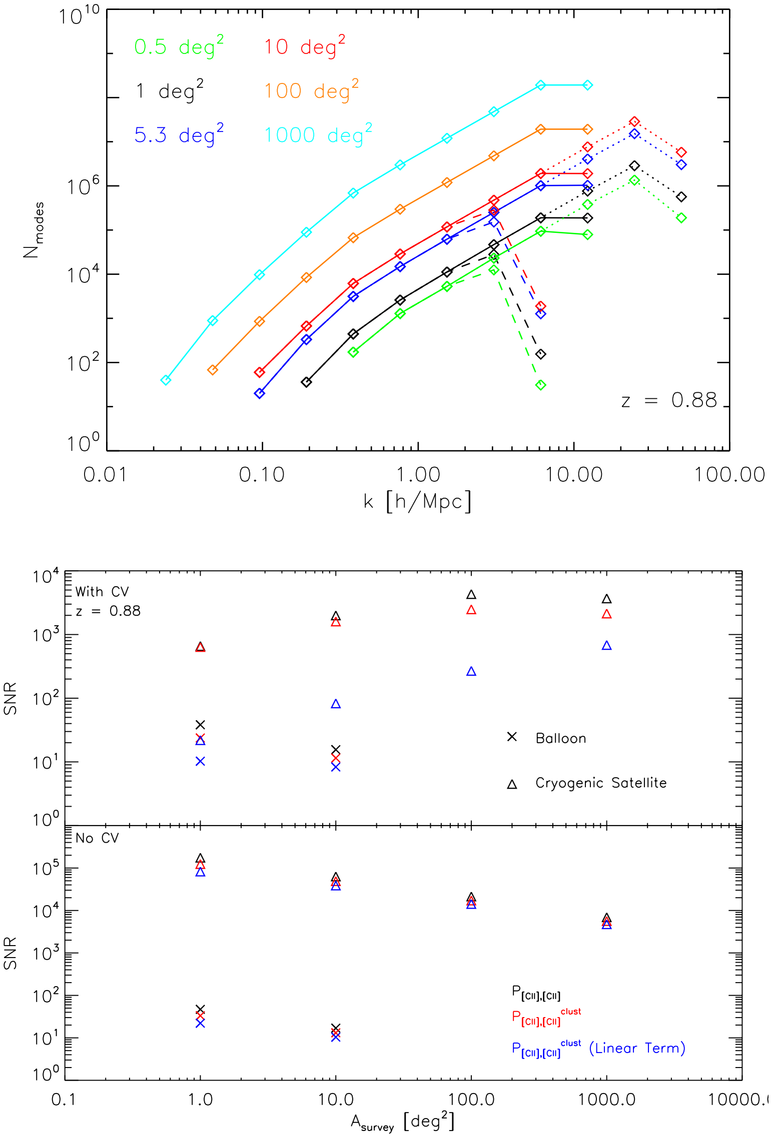

Figure 2.8: Top panel: Number of modes as a function of k at $z = 0.88$ for different survey areas. Telescopes with apertures yielding 0.1, 1, and 10 times the fiducial V_{vox} are shown as the dotted, solid, and dashed lines, respectively. Note that the decline in N_{mode} at high-k is a consequence of the finite size of the rectangular voxels in our surveys; their transverse dimension is set by the instrumental beam size and the line-of-sight dimension by the spectral resolution. Bottom panel: SNR on the total power spectrum (black), clustering power spectrum (red), and the linear portion ($k \lesssim 0.1$ h/Mpc) of the clustering power spectrum (blue) with and without error from cosmic variance. Values for the balloon and cryogenic satellite experiments described in the text are designated with crosses and triangles, respectively.

In the top and bottom panels of Figure 2.8 we examine the effect of changing the survey area and telescope aperture on accessible wavemodes and SNR, where the number of modes has been plotted as a function of k, and SNR has been plotted as as a function of survey area. Our fiducial survey area of $A_{survey} = 1.0$ deg^2 for the balloon experiment is optimal for measuring as many large scale ($k \lesssim 0.1$ h/Mpc) modes as possible with highest SNR in each k-bin, as illustrated in the lower panels of Figure 2.8. In this figure observing time is fixed, so the total SNR increases with survey area when modes are cosmic variance dominated—as in the case for the cryogenic satellite experiment—and decreases when modes are noise-dominated—as in the balloon experiment. When cosmic variance is not included, larger areas merely translate to lower integration time (i.e., greater noise) per voxel, and SNR decreases. The lack of significant change in SNR when including or excluding cosmic variance in the error budget for the balloon experiment indicates that the survey is not cosmic-variance limited. We do not consider surveys with areas less than a square degree because this prohibits measurement of power on large physical scales (cf. top panel of Figure 2.8).

To better demonstrate how the observational parameters drive the behavior of SNR, we rewrite P_N in terms of the parameters from Table 1 (where the units of A_{survey} have been converted to physical area in units of Mpc^2 h^{-2}) giving

$$\begin{aligned} P_N &= \left(\sigma_N^2 A_{pix} \Delta r_{los}^{vox}\right) / \left(\frac{t_{obs}^{survey}}{n_{beams}/N_{instr}^{spatial}}\right) \\ &= \left(\sigma_N^2 A_{pix} \Delta r_{los}^{vox}\right) / \left(\frac{t_{obs}^{survey} N_{instr}^{spatial}}{A_{survey}/A_{pix}}\right) \\ &= \sigma_N^2 \frac{\Delta r_{los}^{vox} A_{survey}}{t_{obs}^{survey} N_{instr}^{spatial}} \end{aligned} \tag{2.3.5}$$

In this form, it becomes apparent that—with fixed number of spatial pixels, spectral resolution, and total observing time—the only factor driving up the amplitude of noise power is the survey area; the effect of increasing aperture only allows access to higher wavenumbers, which is important for subtracting the shot noise from the total power to reveal the clustering.

2.3.2 Measuring Line Luminosity Density Over Cosmic Time

As noted above, intensity mapping is naturally sensitive to the full range of galaxy luminosities through the mean intensity, which is imprinted in the linear (2-halo) clustering term. Shot noise must be accurately subtracted, and this should be straightforward given the high SNR in the shot-noise dominated k bins (Figure 2.7). Next, per Equation 2.2.1, a measurement of the clustering power in the line emission directly constrains the product $\bar{S}_i^2 \bar{b}_i^2$. To extract $\bar{S}_i$, it is necessary to divide out

$P_{\delta,\delta}(k,z)$ and $\bar{b}^2_{\text{[CII]}}(z)$. The confidence with which these are *a priori* known quantities becomes lower as k increases. For example, the 1-halo power spectrum for DSFGs appears to be dependent on the IR luminosity of the contributing sources (Viero et al. 2012), indicating the need to map sufficiently wide areas that access k modes where the power is largely independent of the level of 1-halo power. In the case of the galaxy bias, measurements of the angular dependence of the clustering can, in principle, be used to independently solve for $\bar{b}_i$ via the anisotropy in the angular power spectrum induced by redshift space distortions, as suggested in Lidz et al. (2011a).

Returning to Figure 2.8 (top panel), we see that, for the purpose of measuring $\bar{S}_{\text{[CII]}}$ with the fiducial survey of 1 deg^2 with the balloon experiment, there are two k bins ($k = 0.16$ and 0.32 h/Mpc) in which the 2-halo clustering accounts for at least 80% of the total power. (A survey with 10 deg^2, also shown in Figure 2.8, is wide enough to have three k bins available in the linear regime, but the sensitivity on the additional mode with t_{obs}^{survey}= 450 hours is marginal.) Thus, in considering the case of $A_{survey} = 1.0$ deg^2, we find that it is possible to measure the co-moving [CII] luminosity density, $\rho_{\text{[CII]}}(z)$, in physical units of L$_\odot$ (Mpc/h)$^{-3}$,

$$\rho_{\text{[CII]}}(z) = \int \text{dlog}L_{IR}\Phi(L_{IR},z)f_{\text{[CII]}}L_{IR} \tag{2.3.6}$$

$$= \bar{S}_{\text{[CII]}}4\pi\lambda_{\text{[CII]},rest}H(z), \tag{2.3.7}$$

within $\sim$ 10% accuracy from $z = 0.63$ to $z = 1.48$, as depicted in Figure 2.9. Here, the fractional uncertainty on $\rho_{\text{[CII]}}(z)$ (or, equivalently, on $\bar{S}_{\text{[CII]}}(z)$ via the mapping described in Equation 2.3.7) has been calculated according to standard error propagation as half the fractional uncertainty on $P_{\text{[CII]},\text{[CII]}}(k,z)$, so that the SNR on $\bar{S}_{\text{[CII]}}(z)$ is twice the SNR on the clustering power spectrum, $P_{i,i}^{clust}(k,z)$:

$$\text{SNR on } \bar{S}_{\text{[CII]}} = 2\times\sqrt{\sum_{\text{linear k}-\text{bins only}}\left(\frac{P_{i,i}^{clust}(k)}{\sigma_{clust}(k)}\right)^2} \tag{2.3.8}$$

where σ_{clust} is merely the shot-noise subtracted version of Equation 2.3.3, or, explicitly,

$$\sigma_{clust}(k) = \sqrt{\frac{\left(P_{i,i}^{clust}(k)+P_N(k)\right)^2}{N_{modes}(k)}}, \tag{2.3.9}$$

In Figure 2.9, we also include, for comparison, an estimate for $\rho_{\text{[CII]}}(z)$ based on the analytic fit to SFRD(z) provided by Hopkins & Beacom (2006b) and flat ratios of $L_{\text{[CII]}}/L_{IR} = 0.001$ and 0.003. (For this purpose, we use the standard relation between SFRD and infrared luminosity described in Kennicutt (1998b).)

The cryogenic satellite offers an unprecedented platform for quantifying the evolution of far-IR line emission in cosmological volumes over time, with fractional uncertainties on the order of a tenth of a percent at each redshift for the 1,000 deg^2 survey ($t_{obs}^{survey} = 450$ hr).

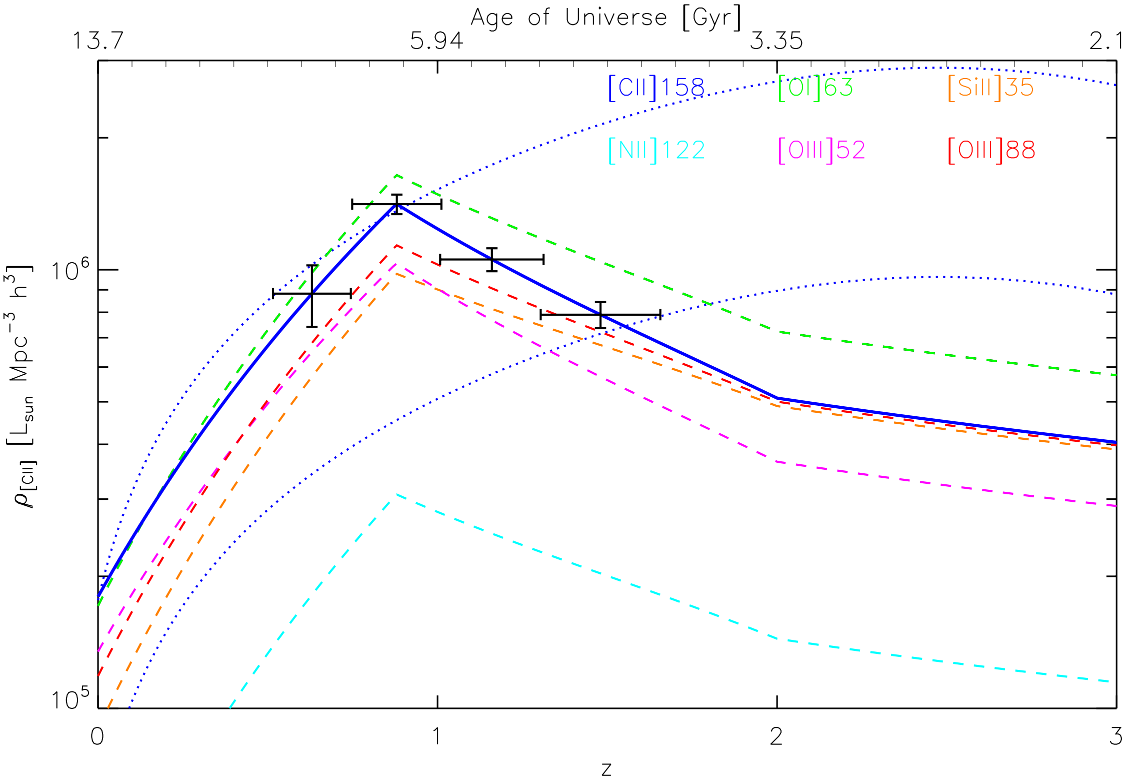

Figure 2.9: Error bar estimates on $\rho_{[\mathrm{CII}]}$, as measured by the fiducial balloon experiment, at redshifts $z = 0.63$, 0.88, 1.16, and 1.48. Errors in z correspond to the redshift space spanned by the spectrometer bandwidth. The solid blue curve is the underlying, fiducial Béthermin-Spinoglio model for [CII] luminosity density. The luminosity density of other bright IR lines, also from the fiducial model, are shown as the dashed colored curves, and the dotted curve is an estimate for $\rho_{[\mathrm{CII}]}$ based on the fit to SFRD(z) provided by Hopkins & Beacom (2006b), where we have used constant ratios of $L_{[\mathrm{CII}]}$ to L_{IR} equal to 0.001 (bottom curve) and 0.003 (top curve) to convert from IR luminosity density to [CII] luminosity density. Note that one can distinguish the different cosmic [CII] emission histories with the fiducial balloon experiment.

2.4 Observational Strategy: Comparing Intensity Mapping with Traditional Galaxy Surveys

2.4.1 Probes of the mean line intensity

Now let us turn to a question regarding the motivation for intensity mapping in general, as well as in the specific case of [CII] at the redshifts relevant to this study. Having identified the galaxy redshift surveys as an alternative method to measure the mean intensity of the line-emitting galaxy population and to measure the 3-D clustering power spectrum, it is natural to draw a comparison of the two approaches.

The principal advantage of intensity mapping is that it naturally measures the aggregate emission per Equation 2.2.7, since the power spectrum depends on the integral of the [CII] luminosity function. Galaxy surveys always miss some of the light in the faintest galaxies, and this completeness problem is illustrated in Figure 2.11. To make concrete comparisons in what follows we employ toy models for the infrared luminosity function (dotted curves in Figure 2.3) written in the Schechter formalism—parametrized by the usual α, L_*, and ϕ_*—and normalize the total IR luminosity density according to B11 (cf. Appendix for details). We stress that these Schechter models are not intended to represent a real interpretation of the distribution of galaxies, but are merely helpful for illustrating the effect of the LF *shape* on the relative usefulness of intensity mapping and traditional galaxy surveys. In converting the IR LF to a line luminosity function, we use, in addition to the Spinoglio et al. (2012a) relation for $L_{[\mathrm{CII}]}/L_{IR}$, a conservative and flat line-to-IR luminosity ratio of 10^{-3}, relegating the luminosity-dependence of this ratio (and any redshift evolution) as a second order effect.

The line sensitivity, S_γ (units of W m^{-2} s$^{1/2}$), is the figure of merit for detecting an unresolved line in a point source, and we define individual detections at the 5σ level as having a flux above the instrumental noise in a voxel, i.e., above $5 \times \frac{S_\gamma}{\sqrt{t_{obs}^{vox}}}$. (In addition to instrumental noise, both Poisson fluctuations in the abundance of faint sources as well as the clustering of these sources may impact the ability to detect galaxies in the survey. However, we have explicitly checked that this "confusion noise" is subdominant compared to instrumental noise for surveys considered in this work and do not consider this further here.) A convenient expression, which explicitly ties the minimum detectable line luminosity to a set of theoretical and experimental parameters, for the detection threshold can be written as

$$L_{i,min} = 5 \times f_{err} \rho_i V_{vox}, \tag{2.4.1}$$

Here, f_{err} is the fractional error (Eq. 2.3.1) and ρ_i is the comoving luminosity density of line i at some z, or $L_* \phi_* \Gamma(2+\alpha, L/L_*)$ in the Schechter notation, so that equality holds between Equation 2.4.1 and the more conventional expression for the

5σ detection threshold:

$$\frac{L_{i,min}}{4\pi D_L^2} \Leftrightarrow 5 \times \frac{S_\gamma}{\sqrt{t_{obs}^{vox}}} \tag{2.4.2}$$

The survey depths $L_{IR,min}$ as a function of f_{err}, V_{vox}, and α are plotted in Figure 2.10. Note that we are investigating the effect of changing telescope aperture, which only changes the transverse dimensions of V_{vox}.

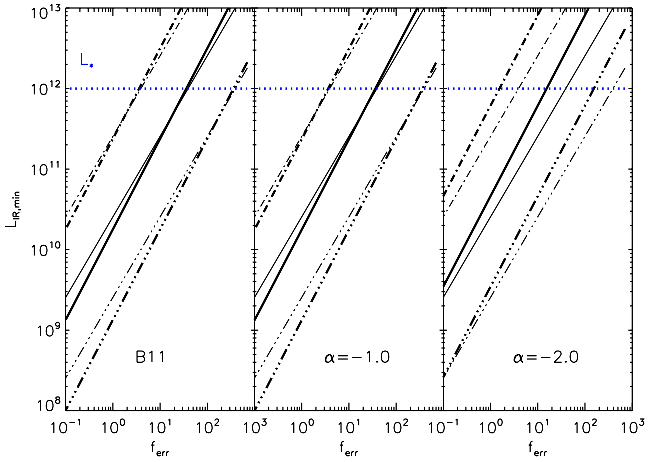

Figure 2.10: IR depth as a function the fractional error. $L_{IR,min}$ refers to the minimum source luminosity that may be directly in the survey at 5σ confidence. Results are plotted for the B11 (leftmost panel) model as well as the toy Schechter functions (remaining panels). Solid curves correspond to the fiducial aperture, $D_{ap} = 2.5$ m. Dashed curves correspond to apertures scaled by a factor $\sqrt{\epsilon}$, where $\epsilon = 10$ (triple-dot-dashed) and $\epsilon = 0.1$ (dot-dashed). Thick curves correspond to our fiducial model for [CII] line intensity, based on Spinoglio fits, whereas thin curves denote the use of a constant ratio of $\frac{L_{[\mathrm{CII}]}}{L_{IR}} = 10^{-3}$.

Since the intensity mapping technique contains information in the power spectrum from sources below a given S_γ, we expect that regimes in which the majority of galaxies are too faint to be resolved are better-suited for intensity mapping observations than observations via the traditional galaxy survey. Inspection of Equation 2.4.1 yields that this scenario occurs for large voxels (or large beam sizes), large fractional errors, or steep luminosity functions where the bulk of the galaxy number density is comprised of galaxies with sub-L_* luminosities. These three limiting cases for the fiducial square degree survey at $z = 1.48$ are illustrated in Figures 2.11 and 2.12 for the experimental goals of measuring mean intensity and the clustering power spectrum, respectively.

As an example of the problem posed by steep luminosity functions for galaxy surveys aiming to measure the mean intensity, we refer to the top panel of Figure 2.11. Here, we find that for LFs with α of -1.5 (not shown) or -2.0, the galaxy surveys detect only 30% and $< 1\%$ of the total [CII] light in integrating to an f_{err}

of 10. Increasing the telescope aperture by a factor of $\sqrt{10}$ (shown as the triple-dot-dashed curves) boosts this fraction to 60% in the case of $\alpha = -1.5$, but still recovers 10% or less of the $\rho_{[\mathrm{CII}]}$ for $\alpha = -2.0$.

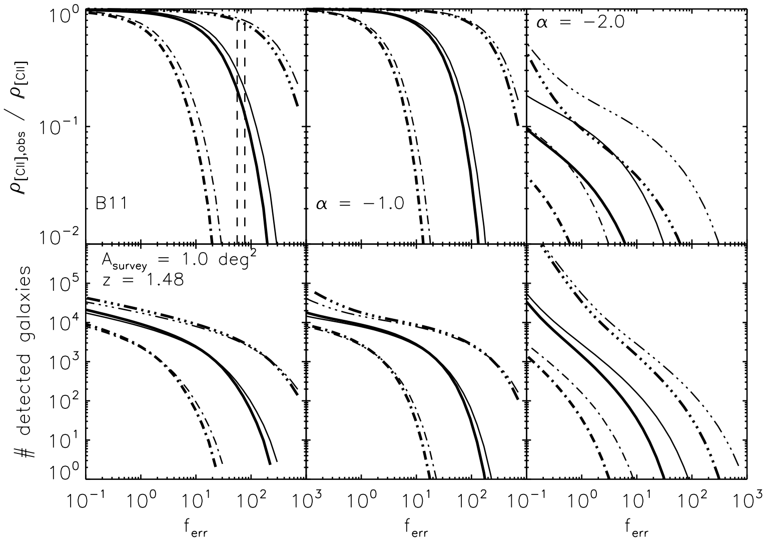

Figure 2.11: Observed fraction of [CII] luminosity density as a function of survey time for the square degree field and the predicted number of [CII]-detected galaxies . Results are plotted for the B11 (leftmost panel) model as well as the toy Schechter functions (remaining panels). Solid curves correspond to the fiducial aperture, $D_{ap} = 2.5$ m. Dashed curves correspond to apertures scaled by a factor $\sqrt{\epsilon}$, where $\epsilon = 10$ (triple-dot-dashed) and $\epsilon = 0.1$ (dot-dashed). Thick curves correspond to our fiducial model for [CII] line intensity, based on Spinoglio fits, whereas thin curves denote the use of a constant ratio of $\frac{L_{[\mathrm{CII}]}}{L_{IR}} = 10^{-3}$. Reference values of f_{err} for the fiducial balloon- and space-borne experiments are shown as dashed vertical lines.

The bottom row of Figure 2.11 breaks down the total emission in terms of the number of detectable galaxies. As is clear from comparison of panels in the top and bottom rows, a large sample of galaxies (of order 1,000 or greater) does not necessarily ensure an unbiased measure of the mean [CII] intensity. If, however, one extracts the aggregate, unresolved emission from [CII] via the intensity mapped power spectrum, one is essentially measuring $\frac{\rho_{[\mathrm{CII}],obs]}}{\rho_{[\mathrm{CII}]}} = 1$ as soon as SNR on the linear clustering term of the power spectrum is sufficiently high, which was depicted in Figure 2.9.

Note that $f_{err} = 1$ allows the galaxy survey to reach a depth ($L_{IR,min} = 4 \times 10^{10}$ $L_{\odot}$ according to Figure 2.10) corresponding to 90% of the total [CII] light at $z = 1.48$ for the B11 model, as shown in the top and leftmost panel of Figure 2.11. A survey to this depth therefore might offer a means to extract the mean intensity by simply integrating the luminosity function. Such a low fractional error, however, requires either very low instrument noise or very long integration times—roughly 10^4 hours for the fiducial balloon-borne instrument when observing a square degree field, for instance. (We refer the reader to Table 2.3 for the conversions between f_{err} and integration time per voxel for the fiducial balloon experiment, as well as for the cryogenic satellite experiment.)

Comparison with small-beam ground-based surveys

Observations from the ground will, of course, lack redshift coverage as they are restricted to known atmospheric windows, yet we examine more closely the ability of ground-based facilities—current and planned—to constrain the mean [CII] intensity with individual detections.

For observations with an ALMA pencil beam survey at $z = 1.2$ (860 GHz, or roughly the central frequency of Band 10), the depth to recover 90% of the [CII] light is $L_{IR,min} = 1.5 \times 10^{10}$ $\mathrm{L}_\odot$, corresponding to a [CII] line flux of 1.4×10^{-20} W m^{-2}. A 5σ detection of this flux demands 22 hours of integration time per beam, assuming a 1σ-1hr sensitivity of 1.4 mJy at $R = 1,000$ with dual polarization and a 12-m array composed of 50 antennas.[1] But, crucially for ALMA, to observe enough galaxies in each luminosity and redshift bin for this purpose requires both many tunings of the observing frequency and telescope pointings on the sky to overcome shot noise, which is the dominant source of noise in the volume of the small ALMA beam. One can estimate the fractional uncertainty on $\bar{S}_{\mathrm{[CII]}}$ due to variance σ^2_{shot} from shot noise, and thus the number of pencil beams $N_{pencils}$ required to achieve a certain fractional uncertainty from the following:

$$\frac{\sigma_{shot}}{\bar{S}_{\mathrm{[CII]}}} = \frac{1}{N^{1/2}_{pencils}} \frac{1}{\bar{S}_{\mathrm{[CII]}}} \left(\frac{P^{shot}_{\mathrm{[CII]},\mathrm{[CII]}}}{V_{beam}} \right)^{1/2} \tag{2.4.3}$$

Above, V_{beam} is the volume of the pencil beam survey,

$$V_{beam} = A^{\mathrm{ALMA}}_{pix} \times \Delta r^{survey}_{los} \tag{2.4.4}$$

where the physical pixel area is $A^{\mathrm{ALMA}}_{pix} = 0.0073$ $(\mathrm{Mpc/h})^3$, and the comoving line-of-sight distance corresponding to the frequency range of the survey is given by Δr^{survey}_{los}. As a concrete example for ALMA, for 16 GHz of backend bandwidth, translating to a redshift depth of 0.04 centered at $z = 1.2$, $V_{beam} = 0.45$ $(\mathrm{Mpc/h})^3$. $P^{shot}_{\mathrm{[CII]},\mathrm{[CII]}}$ is the shot noise as calculated from the combined B11-Spinoglio model. From this expression, we find that $N_{pencils} = 48,000$ in order to achieve $\frac{\sigma_{shot}}{\bar{S}_{\mathrm{[CII]}}}$ of 10%, which, at 1.1×10^6 hours of total observing time excluding overheads, would then match the fractional uncertainty on $\bar{S}_{\mathrm{[CII]}}$ attained by the fiducial intensity mapping balloon experiment in 450 hours.

We note that in the future, CCAT will be more powerful than ALMA for this experiment. While this waveband is not baselined in the first-generation spectrometer

---

[1] Sensitivities have been calculated with the ALMA Sensitivity Calculator, available online at http://almascience.eso.org/proposing/sensitivity-calculator

concept X-Spec, a multi-object wideband spectrometer on CCAT will be somewhat faster than ALMA. Each CCAT backend beam is a factor of 20 less sensitive than ALMA at these frequencies (850 GHz, ALMA Band 10), but the large bandwidth eliminates the need for multiple tunings (~ 6 to cover the full 850 GHz band) and increases the volume of the survey. With 100 backend beams as is baselined for an early generation X-Spec, CCAT/X-Spec has an advantage of a factor of 600 in time, more than overcoming the ALMA sensitivity advantage. With the bandwidth and beam size included, the volume of a CCAT pencil beam is $1.73 \times$ larger than and ALMA beam, so the number of independent beams required to overcome shot noise is smaller by this factor.

Follow-up of known continuum sources with ALMA and CCAT is a possibility to lower the time cost of blind surveys, but this then becomes a biased estimate of the mean intensity, unlike the complete measurement provided by intensity mapping experiments. A benefit of the galaxy surveys, however, is their ability to independently measure the galaxy bias on large scales by comparison to the expected dark matter power spectrum, provided that the surveys can overcome cosmic variance. One appealing scenario is, therefore, to exploit the complementarity of the different approaches and perform galaxy surveys and intensity mapping experiments in conjunction with one another.

Table 2.3: Conversions between t_{obs}^{vox} and f_{err} at $z = 1.48$

$t_{obs}^{vox} f_{err}^2$ ($\times 10^6$)	B11	$\alpha = -1.0$	α = -2.0
Atmospheric Balloon	1.54	1.57	2.83
Cryogenic Satellite	0.0286	0.0292	0.00526

2.4.2 Probes of the power spectrum

There may be applications—such as measuring the BAO peak or searching for primordial non-Gaussianity in large-scale structure—for which the mean intensity is not required, and the shape of the power spectrum, rather than its absolute value, is of interest. For this application, we compare the SNR on a linear-term k bin (up to $k < 0.3$ h/Mpc) for both galaxy detection and intensity mapping surveys (denoted, respectively, by the subscripts "GS" and "IM"), with the expressions:

$$\mathrm{SNR}_{GS} = \frac{\sqrt{N_{modes}}}{1 + 1/(\bar{b}_i^2 P_{\delta,\delta} \bar{n}_{gal})} \tag{2.4.5}$$

$$\mathrm{SNR}_{IM} = \frac{\sqrt{N_{modes}}}{1 + P_N / \left(\bar{S}_i^2 \bar{b}_i^2 P_{\delta,\delta}\right)} \tag{2.4.6}$$

$$= \frac{\sqrt{N_{modes}}}{1 + (f_{err}^2 V_{vox})/(\bar{b}_i^2 P_{\delta,\delta})}$$

Equations 2.4.5 and 2.4.6 assume that the sources in the galaxy survey have the same clustering, and thus the same $\bar{b}_i$, as the sources in the intensity mapping experiment. The quantity $\bar{n}_{gal}^{-1}$ in the expression for SNR_{GS} denotes the shot noise for the galaxy survey, as $\bar{n}_{gal}$ refers to the mean number density of galaxies detected in the survey volume.

Even in this limited comparison of relative SNRs, the intensity mapping often outperforms galaxy surveys, as shown in Figure 2.12. For the steepest faint-end slope ($\alpha = -2.0$) we have tested, $\mathrm{SNR}_{IM} > \mathrm{SNR}_{GS}$ for all f_{err} and beam sizes (i.e., telescope apertures). For the flatter LFs, there are ranges of f_{err} where $\mathrm{SNR}_{IM} > \mathrm{SNR}_{GS}$ for the fiducial case, corresponding to when the galaxy surveys are shot-noise dominated. Figure 2.13 summarizes the results in Figure 2.12 by plotting contours of constant $\frac{\mathrm{SNR}_{IM}}{\mathrm{SNR}_{GS}}$ in the $L_{IR,min} - \alpha$ plane. We see in this figure that there is only a small region—occupied by very flat luminosity functions with slope $\alpha < -1.2$—where the galaxy survey measures the clustering power spectrum with greater SNR than the intensity mapping experiment. It is important to remember that while surveys may detect a large number of galaxies, and thus attain appreciable SNR_{GS} on the power spectrum, the sample of detected galaxies may not yield a measurement of mean intensity, for which a large fraction of the total [CII] light must be observed (cf. Figure 2.11.)

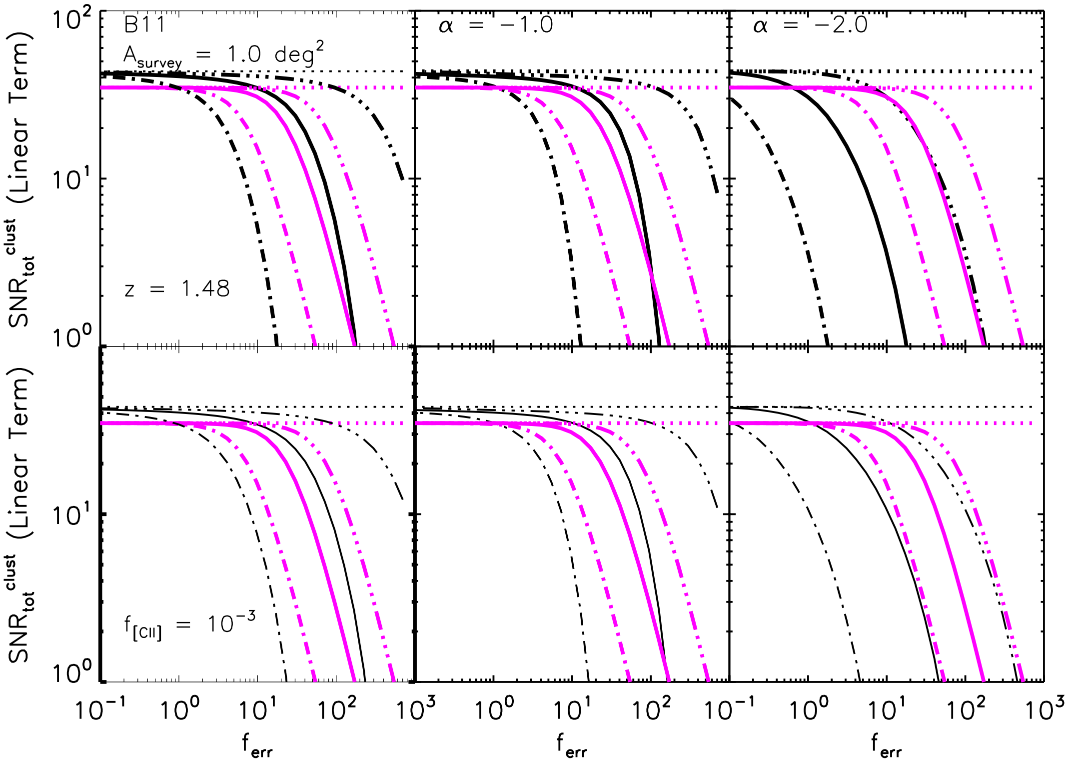

Figure 2.12: Total signal-to-noise ratio on the linear portion of the clustering power spectrum of [CII] at $z = 1.48$ as a function of the fractional error. Results are plotted for the B11 (left panels) model as well as the toy Schechter functions (middle and right panels). SNR_{IM} and SNR_{GS} are plotted as the magenta and black curves, respectively. Solid curves correspond to the fiducial aperture, $d_{ap} = 2.5$ m. Dashed curves correspond to apertures scaled by a factor $\sqrt{\epsilon}$, where $\epsilon = 10$ (triple-dot-dashed) and $\epsilon = 0.1$. The horizontal dotted line is the maximum SNR possible for each approach as set by the number of modes in the survey volume, which is lower for the intensity mapping experiment due to our described mode removal. Results are shown for predictions of [CII] intensity based on the Spinoglio fits (top panel) and a constant ratio of $\frac{L_{[\mathrm{CII}]}}{L_{IR}} = 10^{-3}$ (bottom panel).

We have focused on calculating the SNR of the linear clustering term, which constrains the total [CII] emission and the luminosity-weighted bias of the emitting galaxies. Measurements at smaller scales may help to constrain the spatial distribution of the galaxies within their host dark matter halos, by measuring the shape of the 1-halo term.

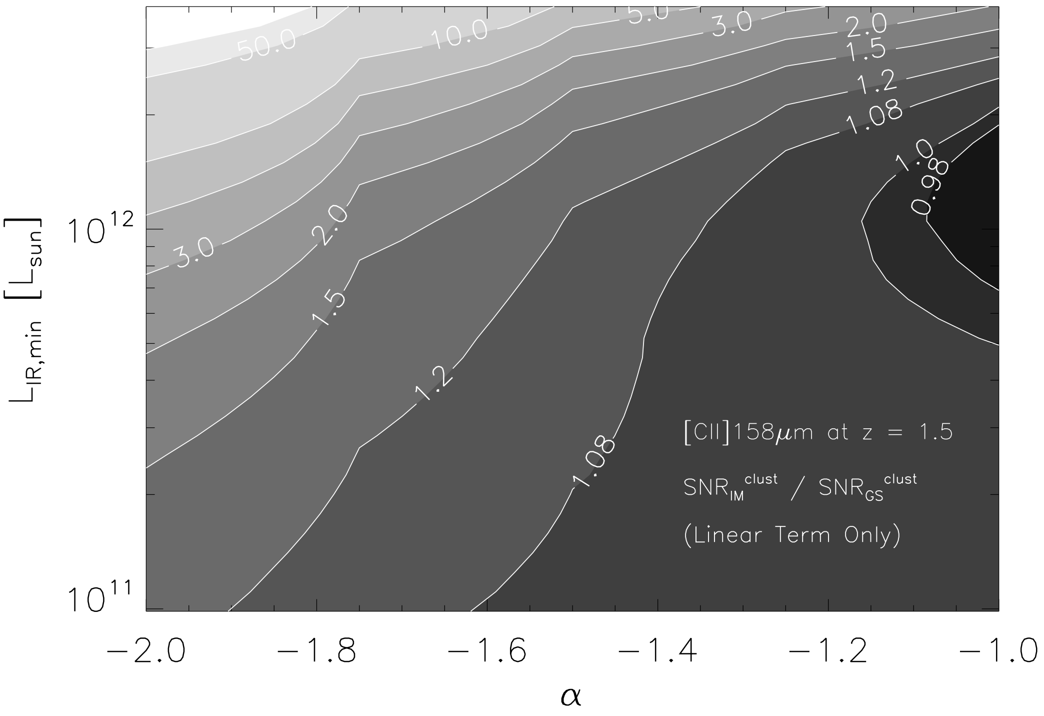

Figure 2.13: Contours of $\mathrm{SNR}_{IM}/\mathrm{SNR}_{GS}$ for the linear term in the [CII] clustering power spectrum at $z = 1.48$, determined for a given depth (in L_{IR}) and IR LF faint-end slope α.

2.5 Summary and Outlook

We have demonstrated the utility of the intensity mapping technique in measuring 3-D power spectrum of far-IR line emission at moderate redshifts, focusing on the important star-formation indicator [CII]. Fluctuations of far-IR fine-structure line intensities have been modeled by combining with the theorized dark matter power spectrum the empirically-constrained estimates of the IR luminosity from the B11 IR luminosity function and Spinoglio et al. (2012a) line-to-L_{IR} relations. We have presented predictions for the measurement of the [CII] auto-power spectrum between $0.63 < z < 1.48$, and found the power spectrum to be detectable in both clustering and shot noise terms in this redshift range with a modest, balloon-borne experimental platform, and exceptionally so with a more ambitious space-borne experimental platform. On large scales, the fact that the clustering amplitude of [CII] fluctuations is proportional to the mean [CII] intensity indicates the potential for measuring cosmic evolution of aggregate [CII]—or of any target line—emission with the line intensity mapping approach, modulo uncertainties in the bias, which may be removed by independent measures such as redshift space distortions. For the fiducial experiments considered in this paper, we have found that it would be possible to measure the [CII] luminosity density with fractional uncertainties on the order of 10% or less. In examining the effect of luminosity function shape, telescope aperture, and fractional error (or instrument noise level) on the relative performances of intensity mapping to galaxy surveys, we have further demonstrated that, in the case where experiments with low fractional errors are not feasible, intensity mapping experiments often outperform galaxy redshift surveys when measuring the mean [CII] intensity. For steep luminosity functions, intensity mapping appears to be the only means of measuring average intensity and thus constraining the bulk of the luminosity function, as well as the optimal method of measuring the clustering power spectrum.

Although beyond the scope of this paper, our findings here reinforce the notion that the $z > 6$ Universe presents an ideal landscape to learn about galaxy populations via intensity mapping. Strong evidence for steep ($\alpha \sim -2.0$) luminosity functions in the rest frame UV at $z \sim 7$ (Bouwens et al. 2014), and larger voxels for a given aperture at higher redshifts, combine to position intensity mapping more favorably compared to galaxy surveys in probing the nature and clustering of the reionizing population.

Looking to the future, the unprecedented sensitivity of background-limited spectrometer technology aboard space-borne experiments as described in this paper may become novel and important platforms to conduct large ($\sim 1,000\ \mathrm{deg}^2$) blind spatio-spectral surveys of far-IR line emission, and warrants further study.

The authors thank Olivier Doré for useful discussions, and Yan Gong for valuable comments that improved this manuscript. BU acknowledges support from the NASA GSRP Fellowship.

Chapter 3

FS Line Intensity Mapping During the Epoch of Reionization

While 3D tomography of ISM lines at moderate redshift can provide insight to the faint end of the luminosity function that may be otherwise unobservable by traditional galaxy surveys, this population of intrinsically faint sources is responsible for less than half of the total [CII] emission, for instance, at that cosmic epoch.

Line intensity mapping during the Epoch of Reionization is particularly appealing because the faint sources are likely to dominate the number density of galaxies and ionizing photon budget of the Universe at that time. Thus, an intensity mapping experiment of ISM lines may provide the only means of directly probing the majority of the galaxy population during Reionization, and would provide highly complementary information about the Reionization process. The infrared FS lines, which are well-established tools to diagnose the physical conditions in the ISM of galaxies, and which we have shown to be useful probes of the mean intensity and galaxy clustering at moderate redshifts, lend themselves as ideal targets for tomographic mapping experiments at high redshift.

In order to estimate the theoretical signal of FS line intensity fluctuations during the Epoch of Reionization, we rely on a simplified model that relates the [OI]63 luminosity emitted by a galaxy to the mass of its host dark matter (DM) halo. This model is comprised of three main components:

(i) A distribution of DM halo masses and spatial positions at the redshift of interest
(ii) A function relating SFR to DM halo mass, M_h
(iii) A function relating FS line luminosity to SFR

There are a variety of approaches one can adopt for each step outlined above, particularly in (ii) and (iii), where theoretical uncertainties are large and observations of the relevant quantities (i.e., FS line luminosities and star formation rates) are currently limited at $z > 6$.

While it is possible to analytically predict the distribution of DM halo masses and their spatial clustering with, for example, the analytic halo model formalism (**?**), we instead obtain the required distributions in (i) from a halo catalog containing masses down to $M_h \sim 10^8$ M$_\odot$[1] and spatial positions of DM halos in a simulated volume (Lidz et al. 2009) of (130 Mpc h^{-1})^3 at $z = 6.9$. According to Lidz et al. (2009), this redshift is near the end of the Reionization process, when hydrogen gas in the intergalactic medium (IGM) is $\sim$ 80% ionized. The DM halos are then entered into a pixellated grid of $(512)^3$ voxels, which provides the underlying framework for our computations of FS line intensity power spectra.

For (ii), we assume that the baryon content in the DM halo reflects the cosmological ratio, Ω_b/Ω_M, in order to write the SFR as a linear function of M_h. Allowing only a fraction, f_*, of these baryons to form stars over a dynamical timescale, $t_{\rm SF}$, leads to the following relation:

$$\mathrm{SFR} = f_* \frac{\Omega_b}{\Omega_M} \frac{M_h}{t_{\rm SF}} \tag{3.0.1}$$

The fraction of DM halos in the simulation volume undergoing SF is set by the age of the DM halo, or roughly $t_{\rm SF}$ divided by the Hubble time, $t_{\rm H}$. We call this ratio a duty cycle, $f_{\rm duty}$, and find that it is approximately equal to 0.1 when the Universe was 0.8 Gyr old at $z = 6.9$, for the Λ-CDM concordance model[2]. As pointed out in Lidz et al. (2011b), when applied to a halo mass function such as the Sheth-Tormen Mass function (Sheth et al. 2001), Equation 3.0.1 leads to an estimate of the SFR density at $z = 7$ that is comparable to the SFR required to ionize the Universe, under various plausible assumptions about the probability of ionizing photons in galaxies to enter the IGM, for instance.

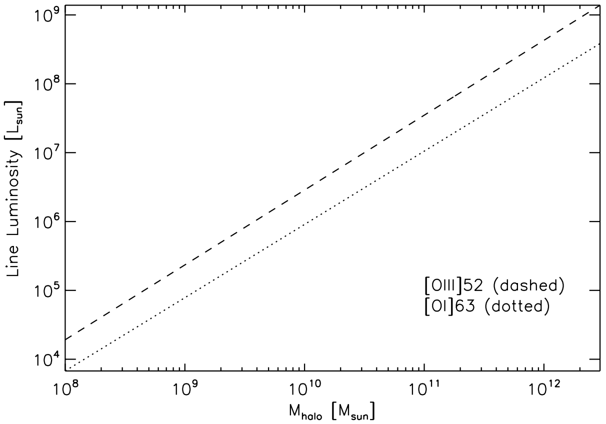

Figure 3.1: [OI]63 and [OIII]52 line luminosities as functions of DM halo mass.

---

[1] This mass, at redshifts during Reionization, corresponds to a DM halo with virial temperature $T_{vir} \geq 10^4$ K, at which temperature gas is able to cool via atomic processes and form stars.

[2] $\Omega_M = 0.27$, $\Omega_\Lambda = 0.73$, and $H_0 = 71$ km s^{-1} Mpc^{-1}

The remaining component in our model is to prescribe a function relating FS line luminosity to SFR. We apply the empirically calibrated line luminosity-SFR relations from De Looze et al. (2014),

$$\log_{10}\mathrm{SFR} = \alpha_i \log_{10} L_i + \beta_i, \tag{3.0.2}$$

where $\alpha_i = 0.94 \pm 0.05$ and 0.92 ± 0.05 and $\beta_i = -6.37 \pm 0.29$ and -6.71 ± 0.33 for $i =$ [OI]63 and [OIII]52, respectively. For now, we focus on these particular spectral lines since they be redshifted into the wavelength coverage of instruments aboard, for example, FIR surveyor space mission concept, CALISTO (Bradford et al. 2015). (Note that we assume the [OIII]52/[OIII]88 line luminosity ratio is of order unity, in order to use the relation for [OIII]88 reported in De Looze et al. (2014).) The sample of galaxies used in that work to calibrate the line luminosity-SFR includes a sample of low-metallicity dwarf galaxies that may be representative of galaxy populations at redshifts during Reionization. For this class of galaxies, De Looze et al. (2014) that the [OIII] line is often brighter than [CII] and [OI]63, and that both [OIII] and [OI]63 are strongly correlated with SFR. Harder ionizing radiation fields and larger fractions of ionized gas in the ISM are possible causes for the brightness of [OIII] emission in the metal poor dwarfs (Cormier et al. 2015). Figure 3.1 shows our model predictions for [OI]63 and [OIII]52 line luminosities as functions of halo mass at $z = 6.9$.

Now, we are ready to compute the expected power spectra of line intensity fluctuations during Reionization. The FS line power spectrum, $P_{i,i}(k)$, we calculate is the average power in spherical shells of width $2\pi/L_x^{sim}$, where L_x^{sim} $(= L_y^{sim} = L_z^{sim})$ is the length of one side ($= 130$ Mpc h^{-1}) of the simulation box, and is plotted as $\Delta^2_{i.,i} = k^3 P_{i,i}(k)/\left(2\pi^2\right)$, with units of surface brightness, squared (Jy^2 sr^{-2}). To demonstrate the sensitivity of the power spectrum on the minimum halo mass, $M_{h,min}$, that is included in the survey volume, we show in Figure 3.2 the [OI]63 power spectrum computed for $M_{h,min} = 10^8, 10^9, 10^{10}$, and 10^{11} M$_\odot$. In Figure 3.3, we show for each cut in M_h, a slice in the corresponding volume in real space. Physical dimensions of the slices are $L_x^{slice} = L_y^{slice} = 130$ Mpc h^{-1} and L_z^{slice}=0.25 Mpc h^{-1}, or, in terms of the number of pixels, $n_x^{slice} = n_y^{slice} = 512$ pixels and $n_z^{slice} = 1$ pixel. As the threshold for mass increases, the number of halos—as well as the mean intensity of [OI]63—in the volume decreases, with all 20,907,733 halos in the volume for $M_{h,min} = 10^8$ M$_\odot$, followed by 4,482,372 for $M_{h,min} = 10^9$ M$_\odot$, 273,737 for $M_{h,min} = 10^{10}$ M$_\odot$, and 2,988 for $M_{h,min} = 10^{11}$ M$_\odot$. The mean [OI]63 intensity in the volume after each cut in halo mass is 596 Jy sr^{-1}, 457 Jy sr^{-1}, 178 Jy sr^{-1}, and 17.24 Jy sr^{-1}, respectively. (We do not consider $M_{h,min} \geq 10^{12}$ M$_\odot$ because there are only 4 DM halos in the volume at $z = 6.9$ above this mass threshold.) In the power spectrum, the removal of halos from the volume subsequently decreases the amplitude of power spectrum by the square of the ratio of mean intensities before and after each mass cut, and increases the power from shot noise until this term clearly dominates the power spectrum for $M_{h,min} \geq 10^{10}$ M$_\odot$ (Figure 3.2). The effect

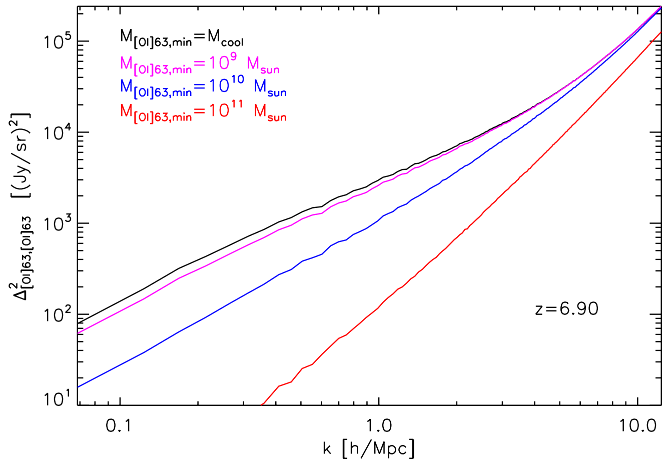

Figure 3.2: Theoretical [OI]63 power spectra for different $M_{h,min}$ in the simulation box at $z = 6.9$. M_{cool} refers to 10^8 $\mathrm{M}_{\odot}$, the so-called "atomic cooling mass" for DM halos.

of removing halos above a certain mass threshold is akin to raising the minimum required mass for DM halos to host SF, or to raising the detection threshold of traditional galaxy surveys that rely on detecting sources above a specific flux.

The sensitivity of a hypothetical imaging spectrometer (10 by 10 spatial pixels, 200 $R = 500$ spectral channels) aboard CALISTO to detecting the [OI]63 and [OIII]52 auto-power spectra is shown in Figure 3.4. Error bars in this figure contain terms for cosmic variance and detector noise power, P_N, and the usual factor $N_m^{-1/2}$ from the averaging over k-modes. The detector noise power is calculated from the quoted NEP of 4×10^{-20} W Hz$^{-1/2}$at 400μm in Table 1 of Bradford et al. (2015). NEPs at longer wavelengths are slightly improved than this number because NEP $\propto \sqrt{\Delta\nu}$, where $\Delta\nu$ is the spectrometer resolution, so that the NEP is 3.59×10^{-20} W Hz$^{-1/2}$ for 497μm and 3.95×10^{-20} W Hz$^{-1/2}$ for 407μm; the listed wavelengths correspond to the observed wavelengths of [OI]63 and [OIII]52 at the redshift of interest. In units of surface brightness, the NEI for the respective surveys in each line is $1.2{\times}10^5$ Jy sr^{-1} and 2.0×10^5 Jy sr^{-1}. We have a adopted a survey geometry to match the transverse area of (130 Mpc h^{-1})^2 of the simulation box, which amounts to mosaics of roughly 80-100 fields-of-view for the relevant line intensity mapping surveys, for which we allot a total observing time of 900 hours. Larger survey areas do not improve power spectrum sensitivity in this case because the survey is already nearly cosmic-variance limited at this redshift. We chose a survey depth of 810 Mpc h^{-1}, corresponding to half of the available instantaneous bandwidth for the envisioned instrument and spanning a redshift of $\Delta z = 0.2(1{+}z)$. For reference, the volume per voxel in the [OI]63 and [OIII]52 line intensity mapping surveys is 19 (Mpc h^{-3})^3 and 12 (Mpc h^{-3})^3, respectively, leading noise powers P_N of 6.1×10^6 (Jy sr^{-1})^2 (Mpc h^{-1})^3 and 1.7×10^7 (Jy sr^{-1})^2 (Mpc h^{-1})^3. Table 3.1

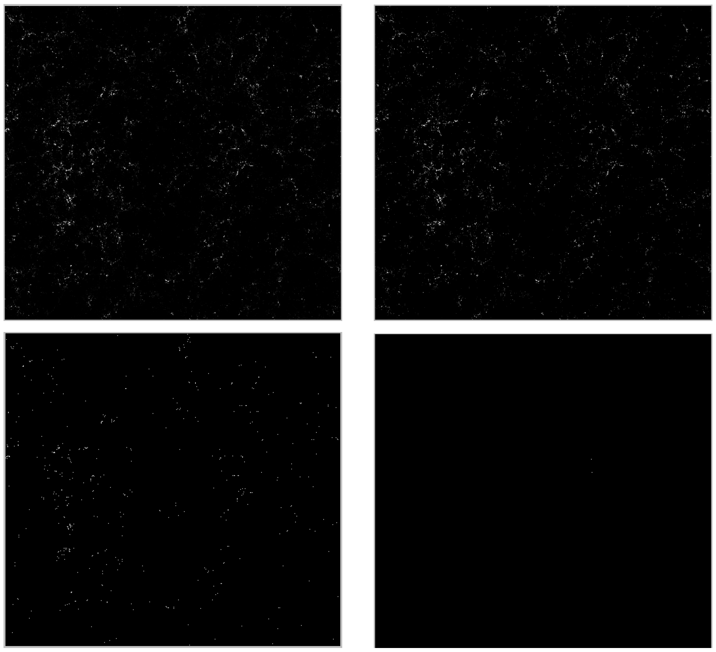

Figure 3.3: Slices in the real space simulation volume showing the positions of halos with $M_h \geq M_{h,min}$, for $M_{h,min} = 10^8$ M$_\odot$ (*top left*), 10^9 M$_\odot$ (*top right*), 10^{10} M$_\odot$ (*bottom left*), and 10^{11} M$_\odot$ (*bottom right*).

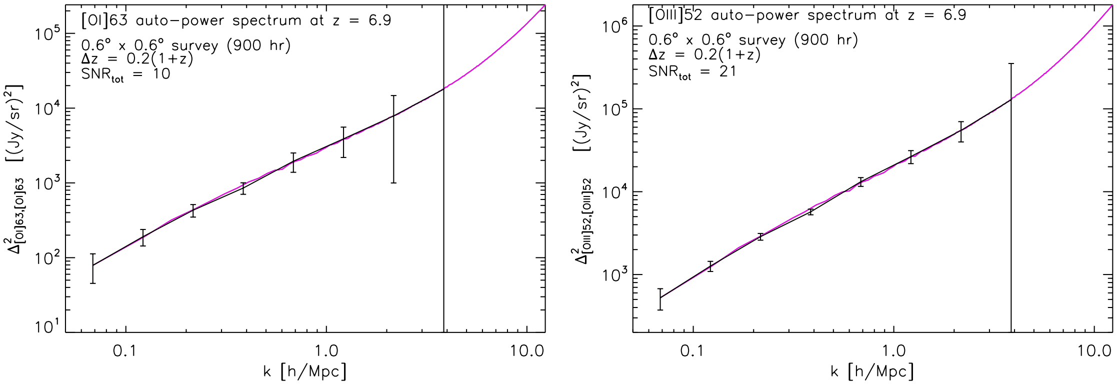

Figure 3.4: Predicted [OI]63 (*left*) and [OIII]52 (*right*) auto-power spectra at $z = 6.9$, for a 900-hr survey 0.6 degrees across and with a depth of $\Delta z = 0.2(1+z)$.

Table 3.1: Parameters for envisioned [OI]63 and [OIII]52 intensity mapping surveys

Telescope aperture (m)	5.0	
R	500	
Depth of spectral channel (Mpc h^{-1})	8.1	
# spectral channels	100	
Bandwidth (Mpc h^{-1})	810	
# instantaneous spatial pixels	100	
Target redshift, z	6.9	
Survey Area (deg^2)	$(0.6)^2$	
Observing time per survey (hr)	900	
Target spectral line	[OI]63	[OIII]52
Observed wavelength (μm)	497	409
Mean line intensity (Jy sr^{-1})	600	1500
Surface brightness sensitivity per voxel (10^6 Jy sr^{-1} $\mathrm{sec}^{-1/2}$)	1.2	2.0
Pixel Area (Mpc^2 h^{-2})	2.3	1.5
Observing Time per voxel (hr)	12.1	8.1
Voxel Volume (Mpc^3 h^{-3})	18.5	12.4
Noise Power (10^6 Jy^2 sr^{-2} Mpc^3 h^{-3})	6.1	17

summarizes the survey parameters considered in this study.

Note that while the chosen depth is longer than the depth of the simulation volume, we only use the additional modes from this larger depth in order to calculate sensitivity on k-modes with magnitudes greater than the fundamental mode, $2\pi/L_x = 2\pi/L_x = 2\pi/L_x = 0.048$ h^{-1} Mpc, of simulation volume. (We have also discarded the lowest two k modes in our sensitivity estimate, in anticipation of foreground removal.) The largest accessible k modes in the volume are determined by the spatial resolution for the 5-m aperture of CALISTO at these wavelengths, and correspond to Nyquist frequencies of 1.4 h^{-1} Mpc and 2.1 h^{-1} Mpc for the [OI]63 and [OIII]52 surveys, respectively. Signal-to-Noise (S/N) ratios for the [OI]63 and [OIII]52 auto power spectra for a couple k modes that probe the clustering and shot noise terms of the power spectrum are listed in Table 3.2. The [OI]63-[OIII]52 cross-power spectrum (not shown) is helpful for verifying that the observed signals originate from the target redshift, and we include S/N for the k modes of interest in Table 3.2, as well.

The NEP of the considered hypothetical instrument implies a point-source sensitivity of 3.4×10^{-20} W m^{-2} $\mathrm{sec}^{-1/2}$ at 497μm and 3.8×10^{-20} W m^{-2} $\mathrm{sec}^{-1/2}$ at 407μm, which translates to [OI]63 and [OIII]52 line luminosities, at $z = 6.9$,of 1.2×10^8 $\mathrm{L}_\odot$ and 1.7×10^8 $\mathrm{L}_\odot$, respectively. Using Equations 3.0.1 and 3.0.2 to back out the mass of the host DM halo emitting in each line, we find that $M_h = 1.0 \times 10^{12}$ $\mathrm{M}_\odot$ for [OI]63 and $M_h = 4.2 \times 10^{11}$ for [OIII]52. From Figure 3.2, it is clear that it is possible to measure the clustering term of the power spectrum and, thus, the mean intensity of either FS line at such high redshift, for the survey

Table 3.2: Predicted S/N on FS line power spectra at $z = 6.9$

Power Spectrum	Total S/N	S/N($k = 0.38$ h^{-1} Mpc)	S/N($k = 1.2$ h^{-1} Mpc)
$\Delta^2_{\mathrm{[OI]63,[OI]63}}$	10.0	5.7	2.3
$\Delta^2_{\mathrm{[OIII]52,[OI]52}}$	21	13	5.6
$\Delta^2_{\mathrm{[OI]63,[OI]52}}$	20	12	5.1

parameters considered here.

Chapter 4

Conclusion

We have learned over the course of this thesis that the infrared fine-structure lines of trace metals in the interstellar medium are useful tools for studying the evolution of galaxies.

In Chapter 1, we saw the power of FS lines to expose co-extant star-formation and X-ray radiation from an accreting supermassive black hole in a galaxy during the epochs of peak cosmic SF and black hole accretion. Then, in Chapter 2, we abandoned detailed single-object studies for an aggregate view of FS line emission from the ISM of galaxies via power spectrum measurements in the intensity mapping approach. Focusing on the [CII]158 line, but developing a framework for studying a suite of IR FS emission lines during the epoch of peak cosmic SF activity, we found that intensity mapping from hypothetical balloon-borne and space-borne missions would enable measurements of the evolution of the total [CII] luminosity density with redshift during $z \sim 0.5-1.5$. Finally, in Chapter 3, we considered extending the application of intensity mapping experiments to higher redshifts to probe galaxies during the Epoch of Reionization. To do so, we adopted a hypothetical space mission and discussed the detectability of the [OIII]52 and [OI]63 auto- and cross-power spectra.

Appendices

Appendix A

Appendix to the Preface

FIR FS line flux ratios and line-to-FIR continuum flux ratios have been computed with *Cloudy* (Ferland et al. 1998) for isobaric and plane-parallel models of combined HII region/PDRs. The edge of the PDR has been defined as per Abel et al. (2005), i.e., where the fraction of hydrogen nuclei in the gas that is comprised of molecular hydrogen has risen to 0.5. Different input SEDs have been used to simulate conditions in instantaneous and continuous starbursts of various durations, as well as in the direct vicinity of stars of various effective temperatures, $T_{eff,*}$. (See Figure A.1 for a sample of input SEDs.) The Cloudy models have been run on grids of varying ionization parameter U—the ratio of ionizing photon flux to gas density—and gas density, n_{H_+}, defined as the initial density at irradiated face of the cloud; hydrogen is entirely ionized at this position in the HII region/PDR model.

Flux ratios presented in Figures A.2 through A.14 include:

[OIII]88,52/[NII]122

[OIII]88,52/[CII]

[OIII]88,52/[OI]63

[OI]63/[CII]

[CII]/[NII]122

[OI]63/FIR

[CII]/FIR

[NII]122/FIR

[OIII]88,52/FIR

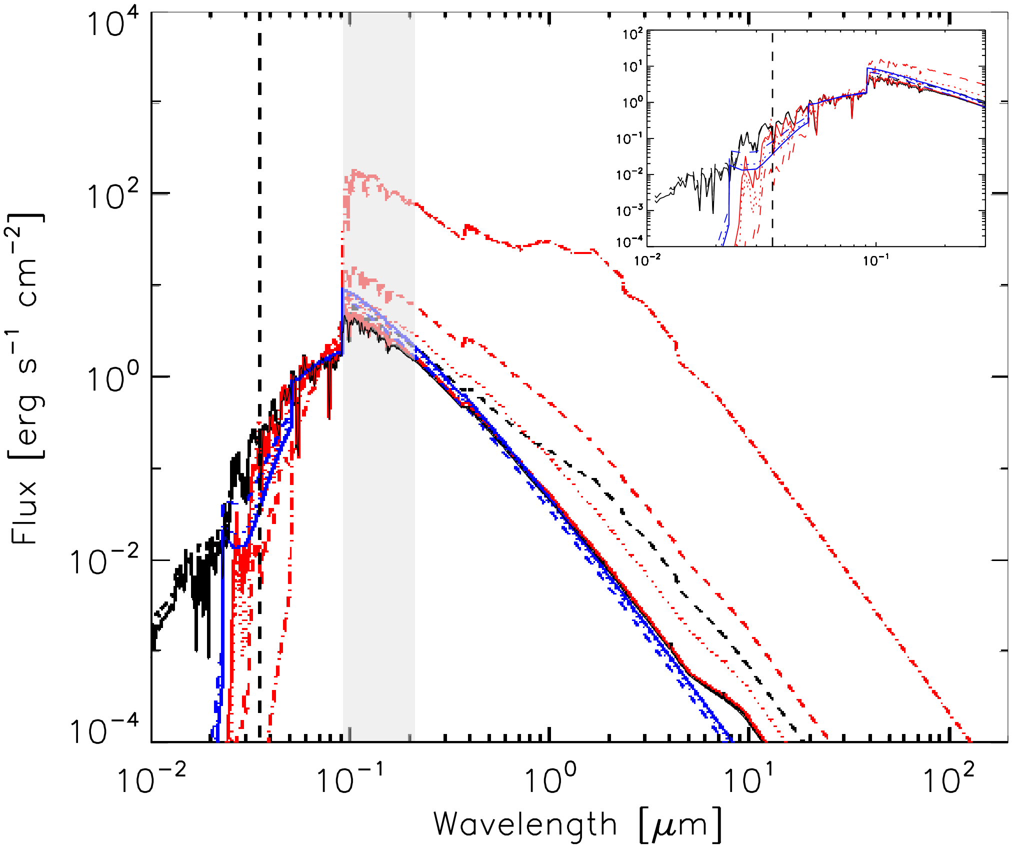

Figure A.1: Input SEDs. Curves shown are SEDs for the various continua used in the Cloudy modeling: instantaneous starbursts (*red curves*) of 3 (*solid*), 4 (*dotted*), and 5 (*dashed*) Myr duration; continuous starbursts (*black curves*) of 5 (*solid*) and 10 (*dashed*) Myr duration; CoStar stellar atmospheres (*blue curves*) for $T_{eff,*}$ = 36000 (*solid*), 36300 (*dotted*), 37000 (*dashed*) K. Shaded gray region corresponds to photon energies in the FUV band. Black dashed vertical line indicates the second ionization energy of the oxygen atom (IE = 35.1 eV). Inset shows the SEDs at wavelengths between 0.01 μm and 0.3 μm.

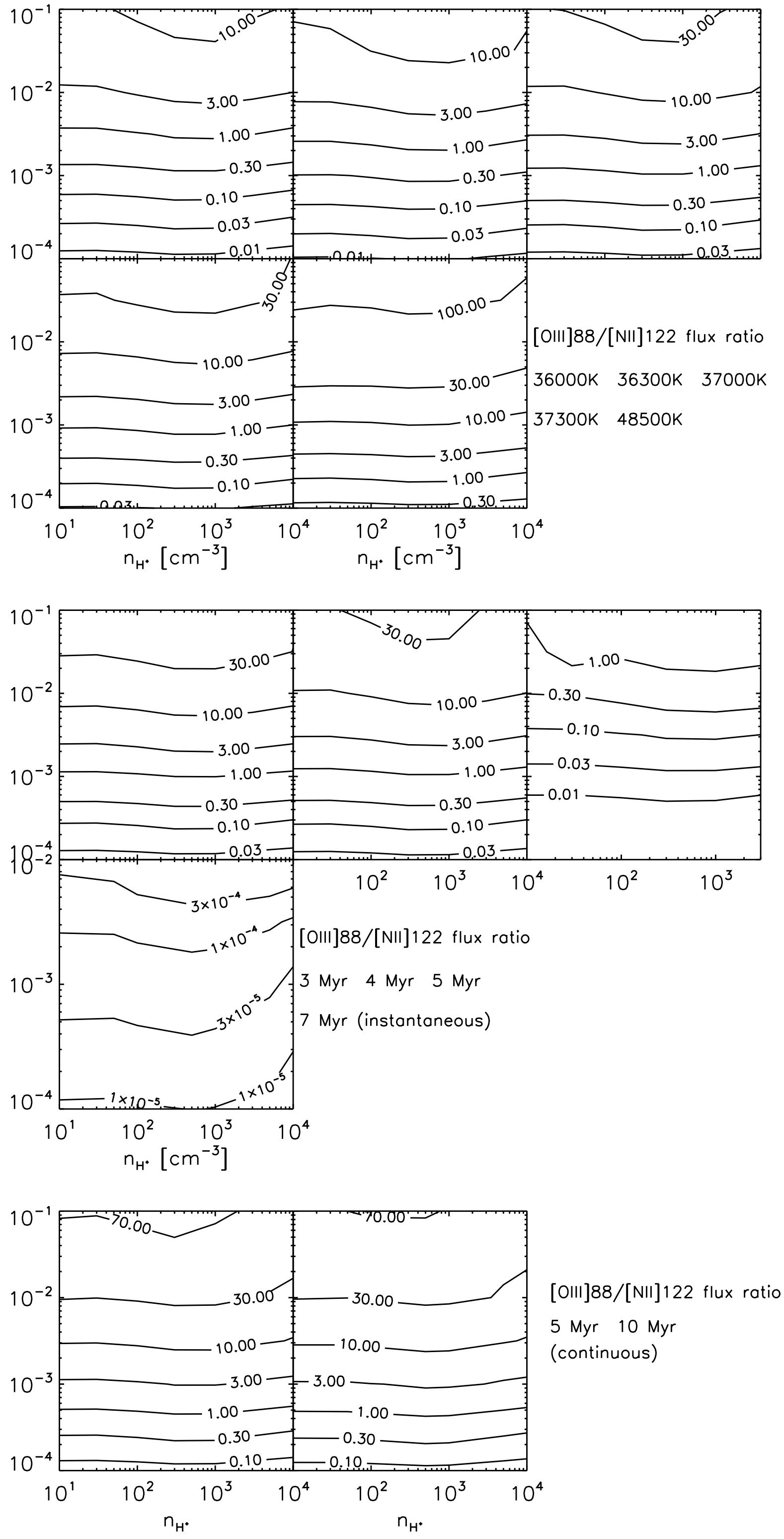

Figure A.2: Cloudy combined HII region/PDR models.

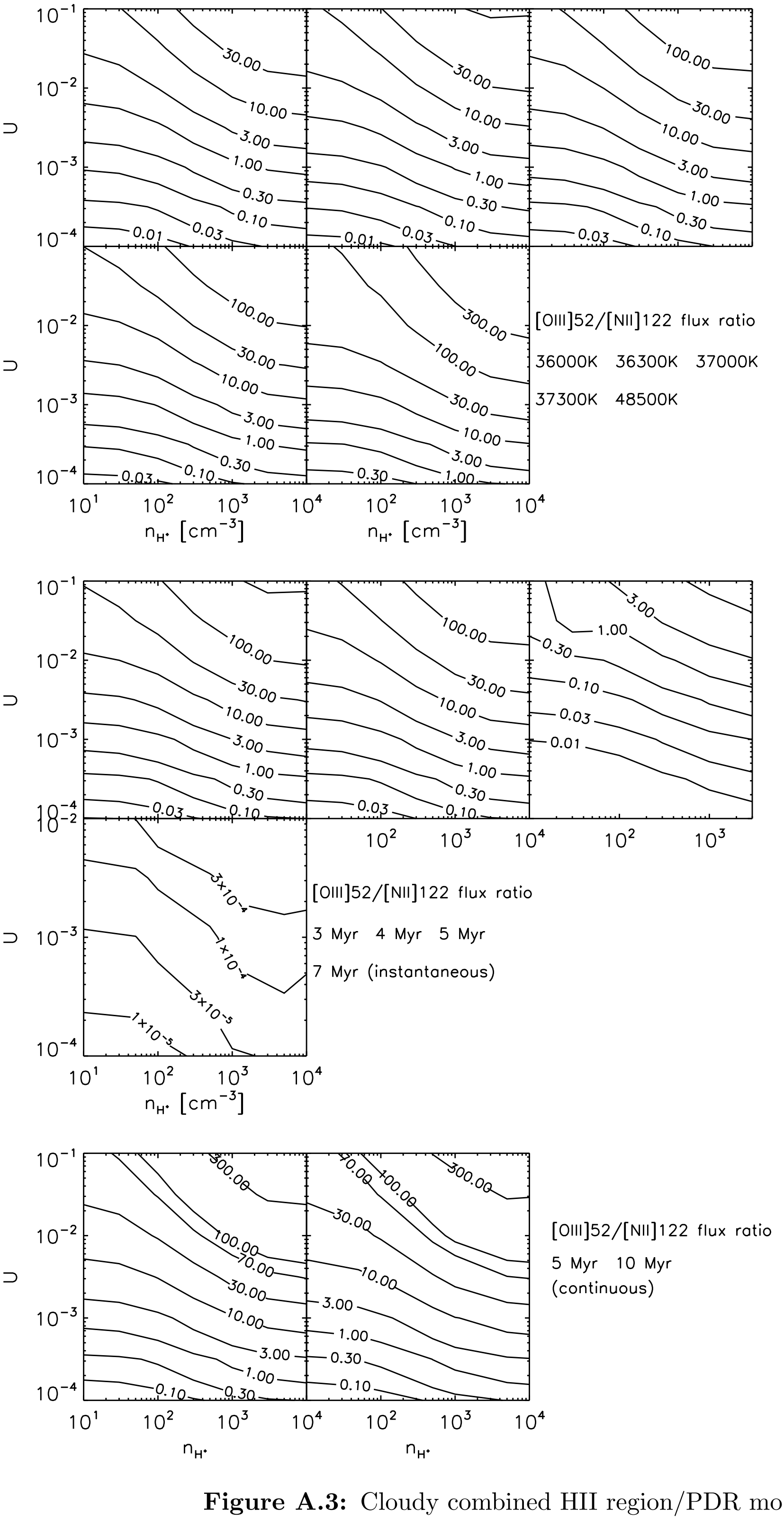

Figure A.3: Cloudy combined HII region/PDR models.

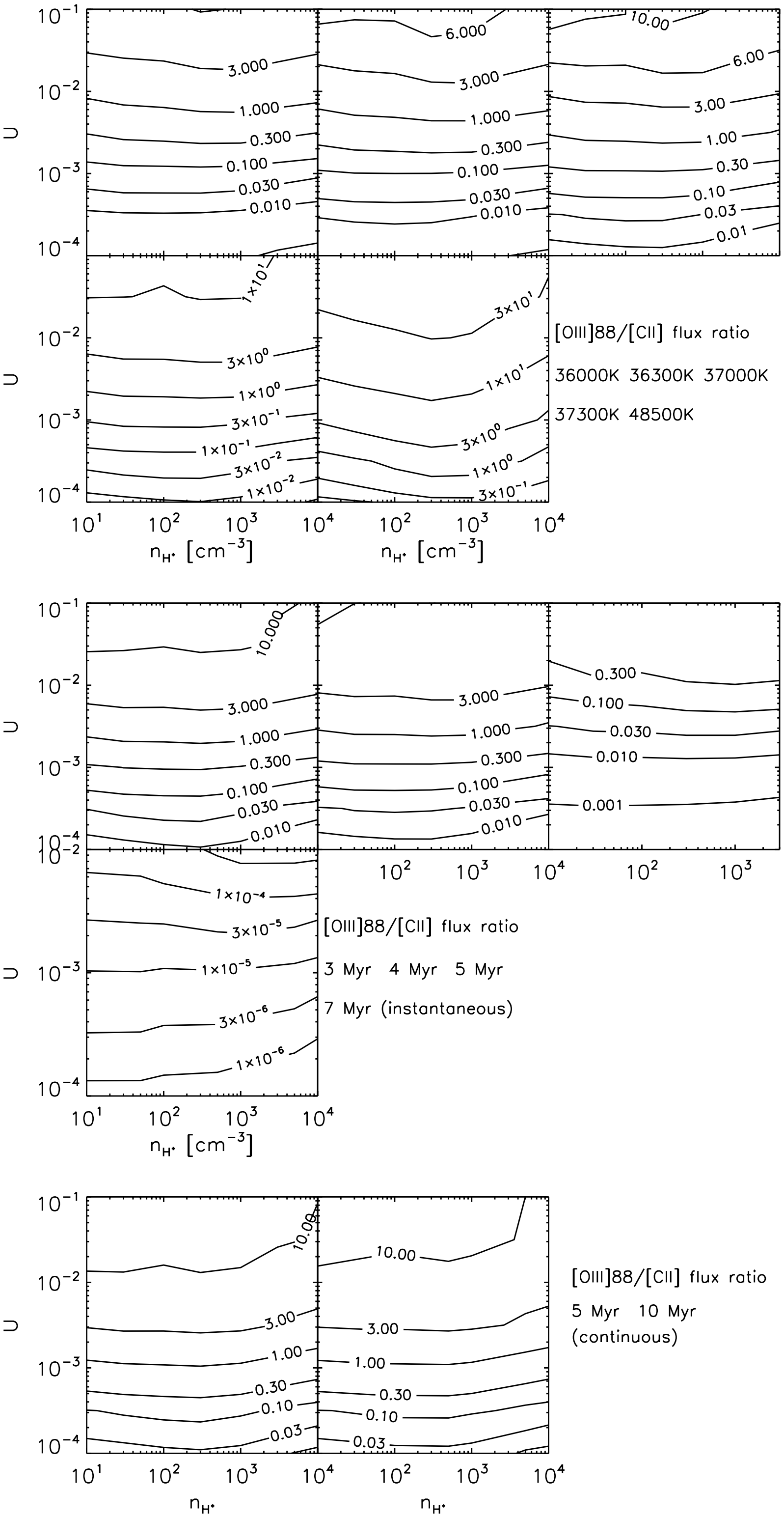

Figure A.4: Cloudy combined HII region/PDR models.

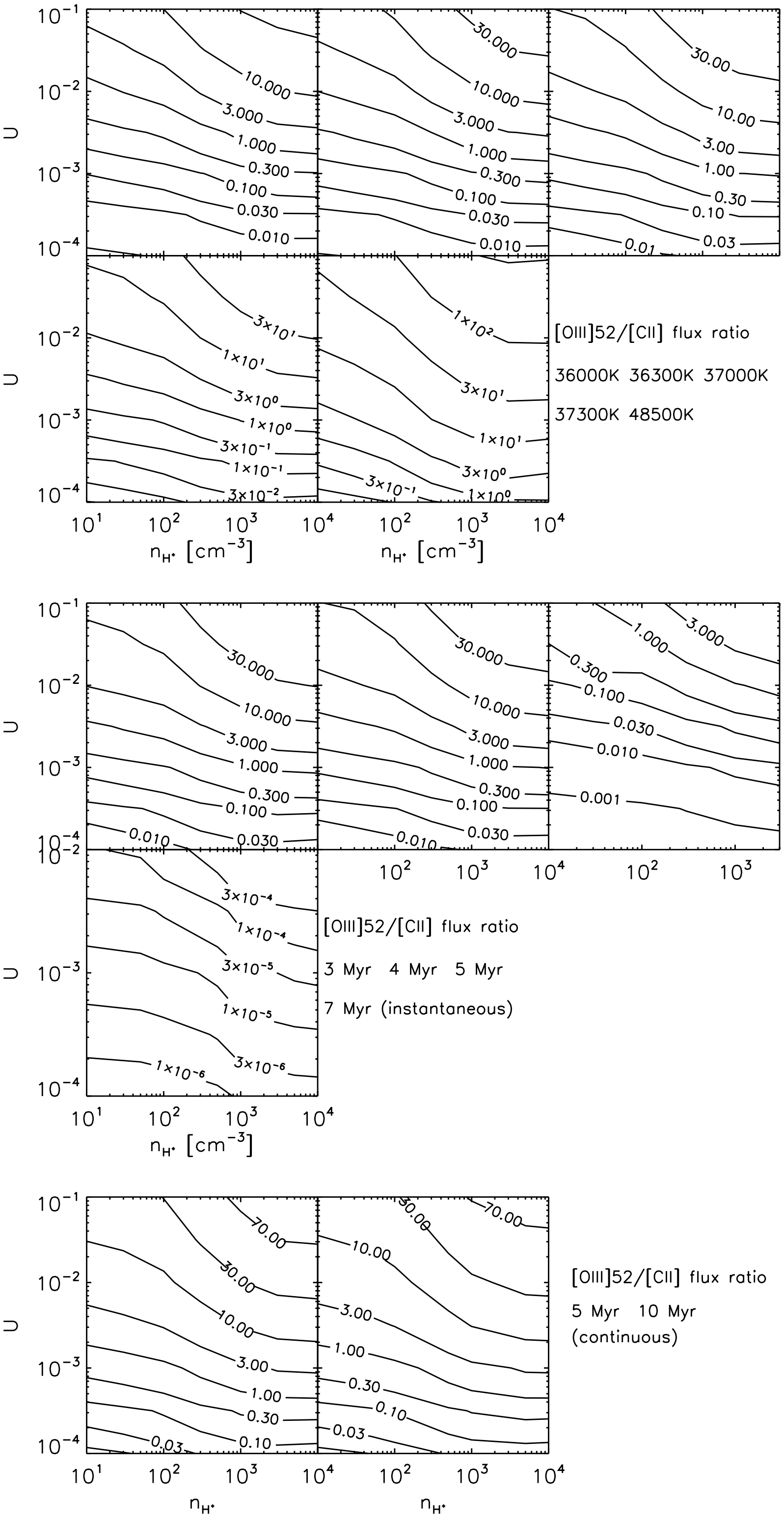

[OIII]52/[CII] flux ratio

36000K 36300K 37000K

37300K 48500K

[OIII]52/[CII] flux ratio

3 Myr 4 Myr 5 Myr

7 Myr (instantaneous)

[OIII]52/[CII] flux ratio

5 Myr 10 Myr

(continuous)

Figure A.5: Cloudy combined HII region/PDR models.

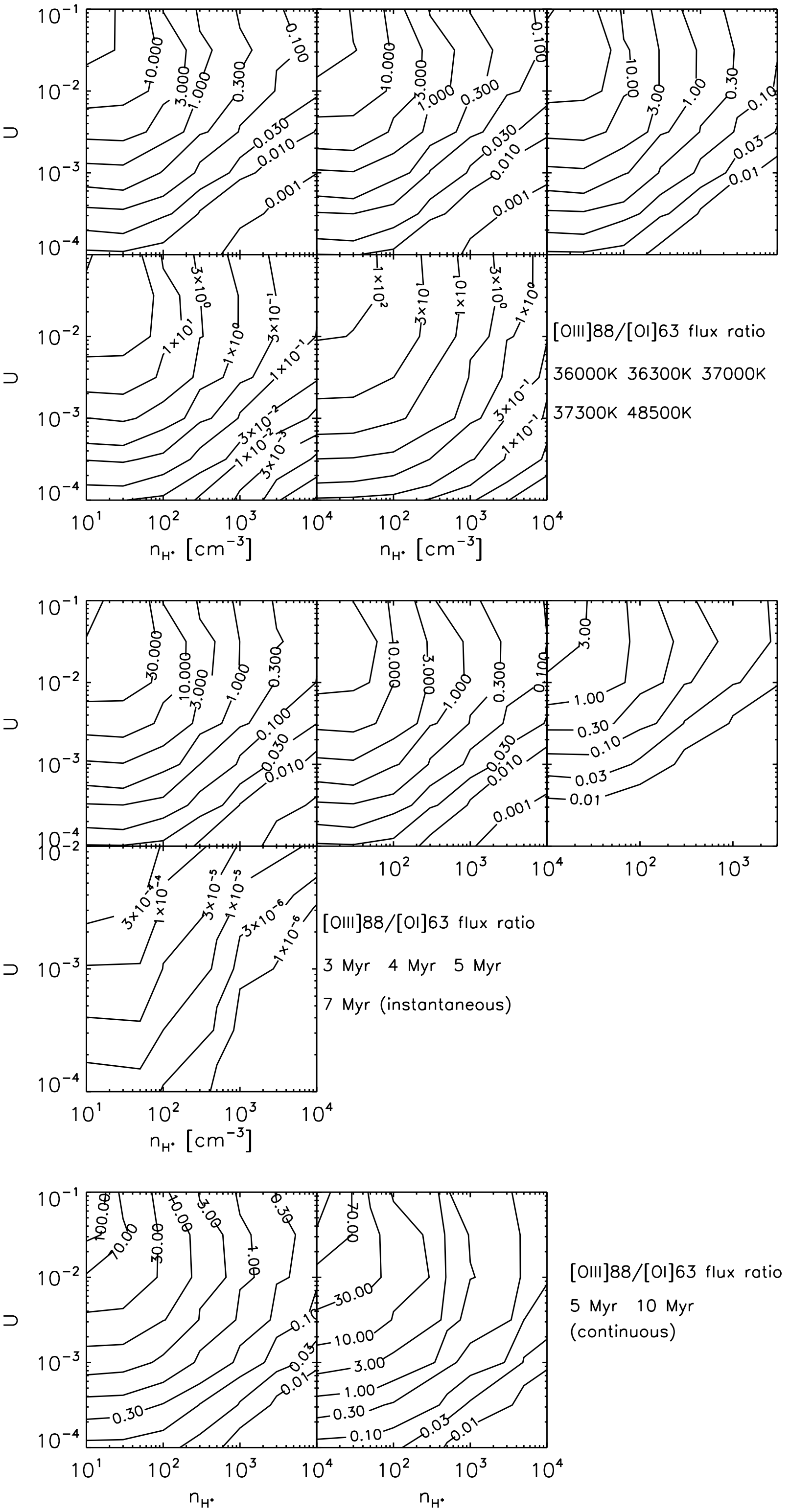

Figure A.6: Cloudy combined HII region/PDR models.

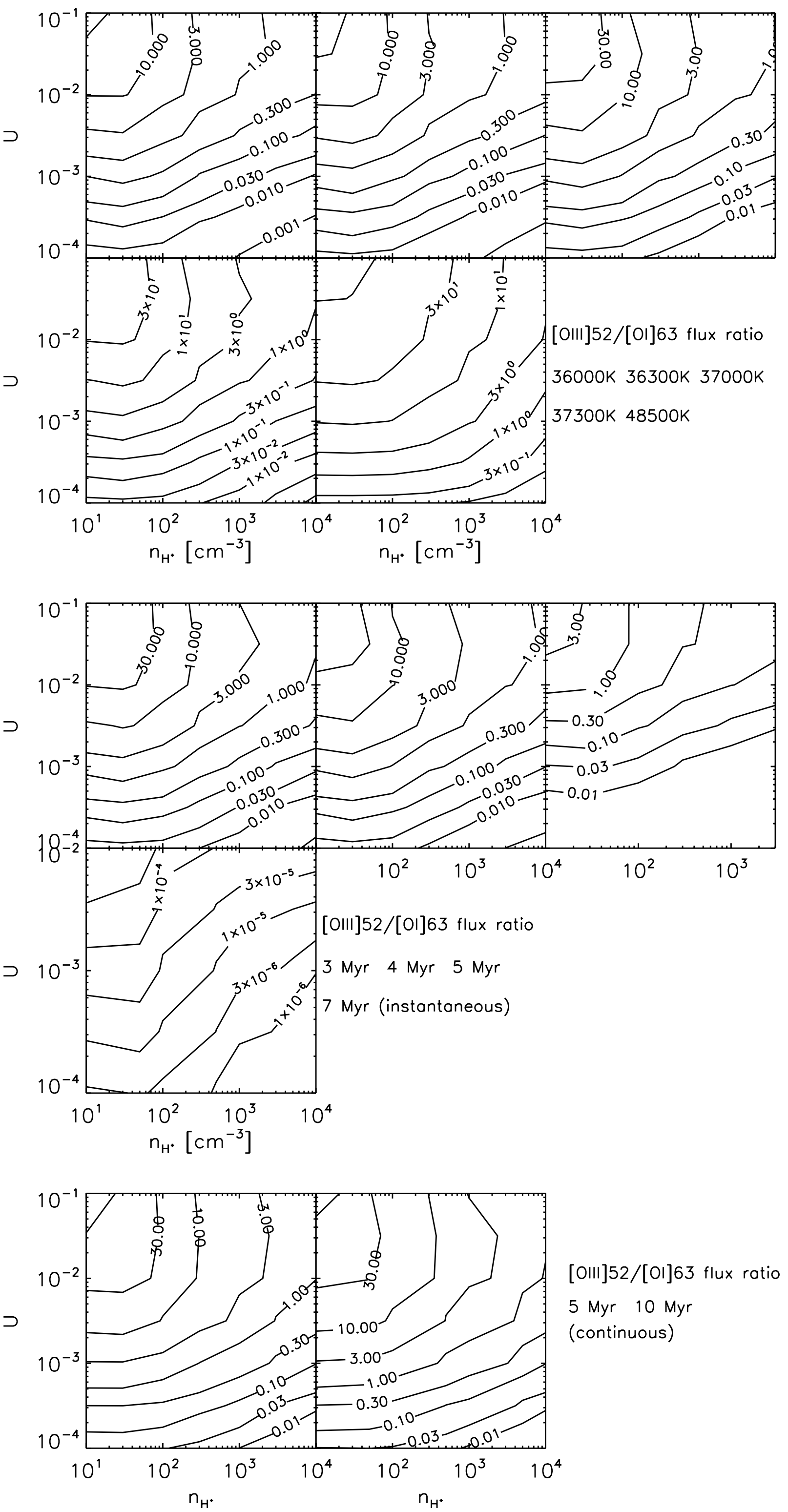

Figure A.7: Cloudy combined HII region/PDR models.

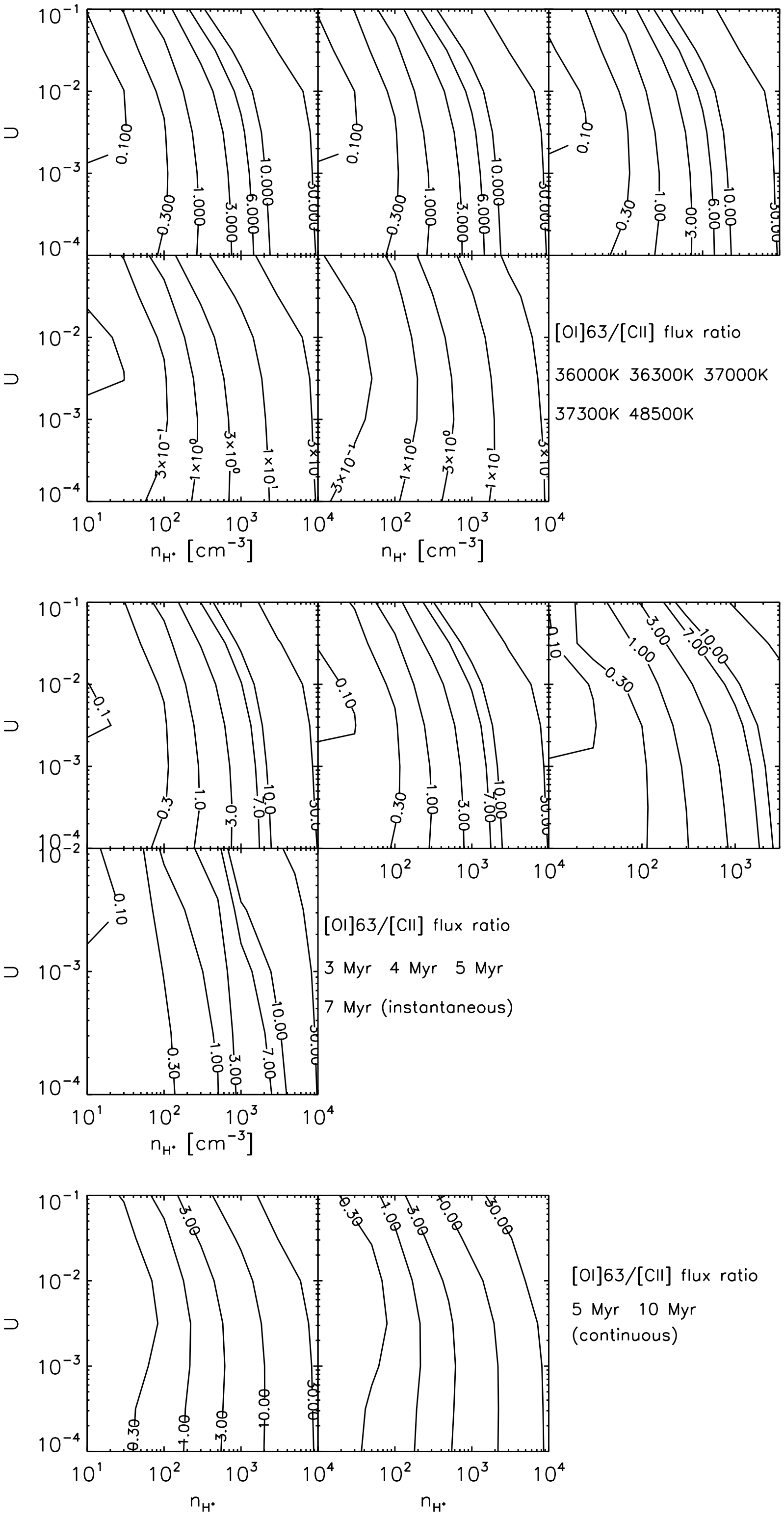

Figure A.8: Cloudy combined HII region/PDR models.

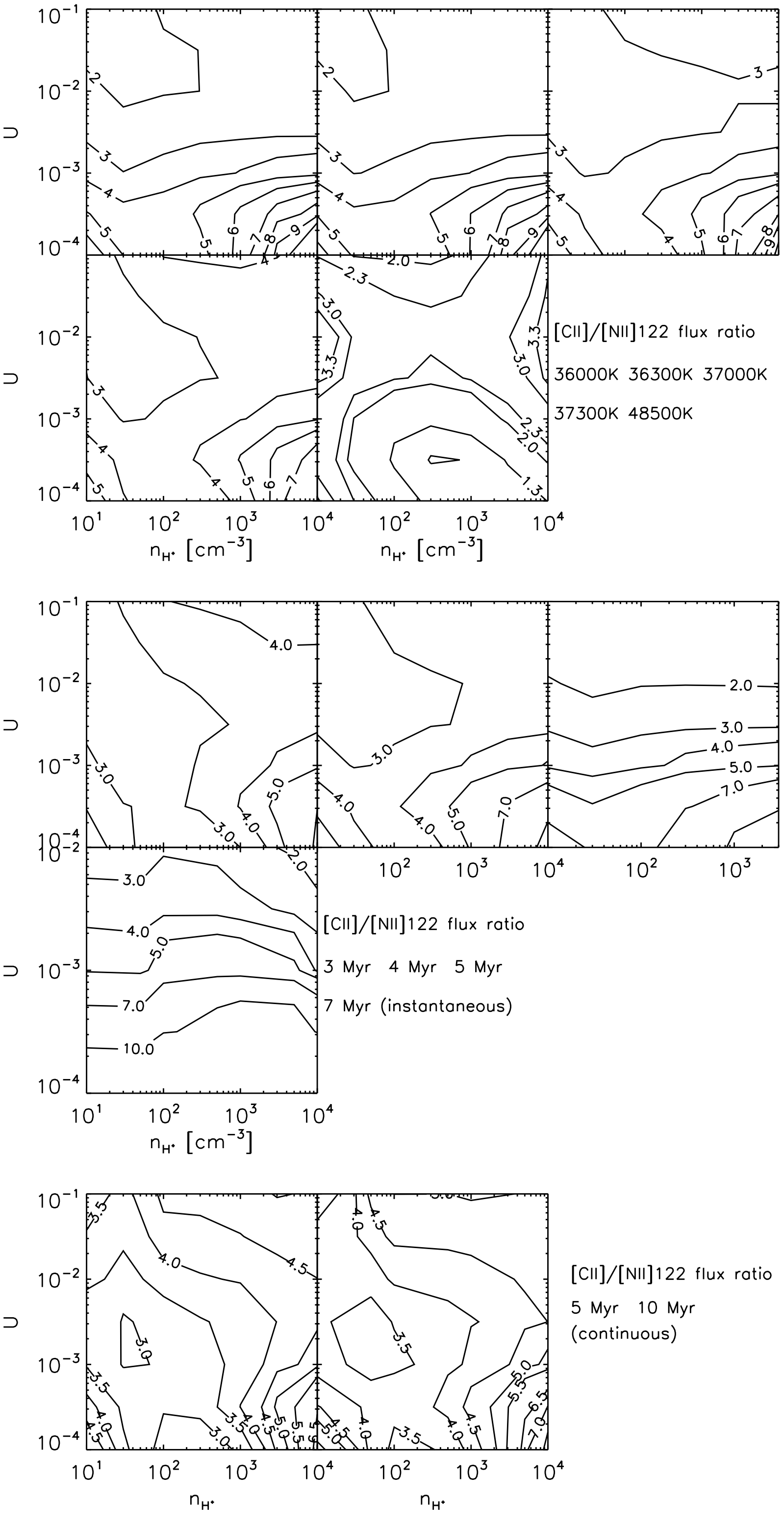

Figure A.9: Cloudy combined HII region/PDR models.

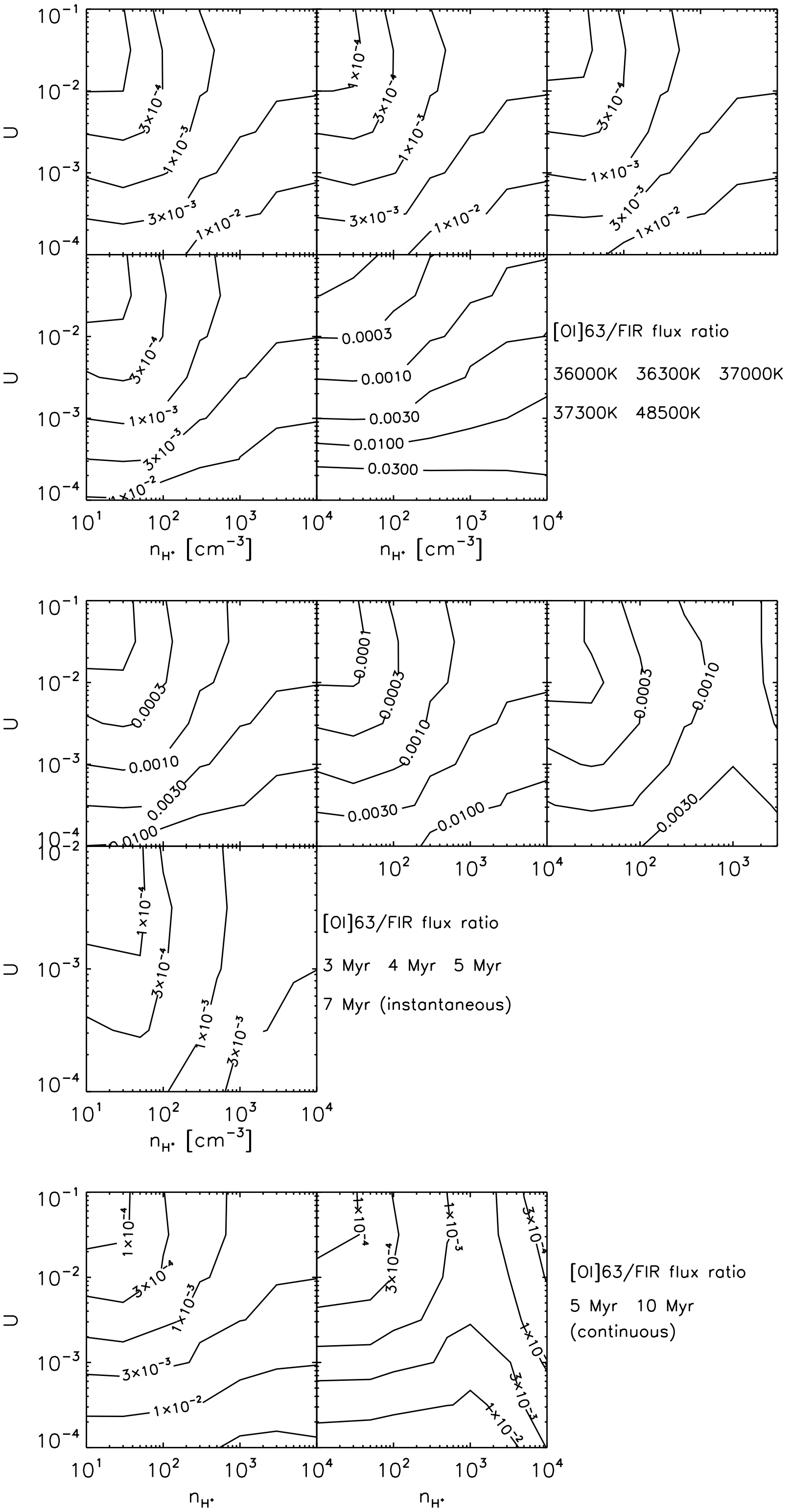

Figure A.10: Cloudy combined HII region/PDR models.

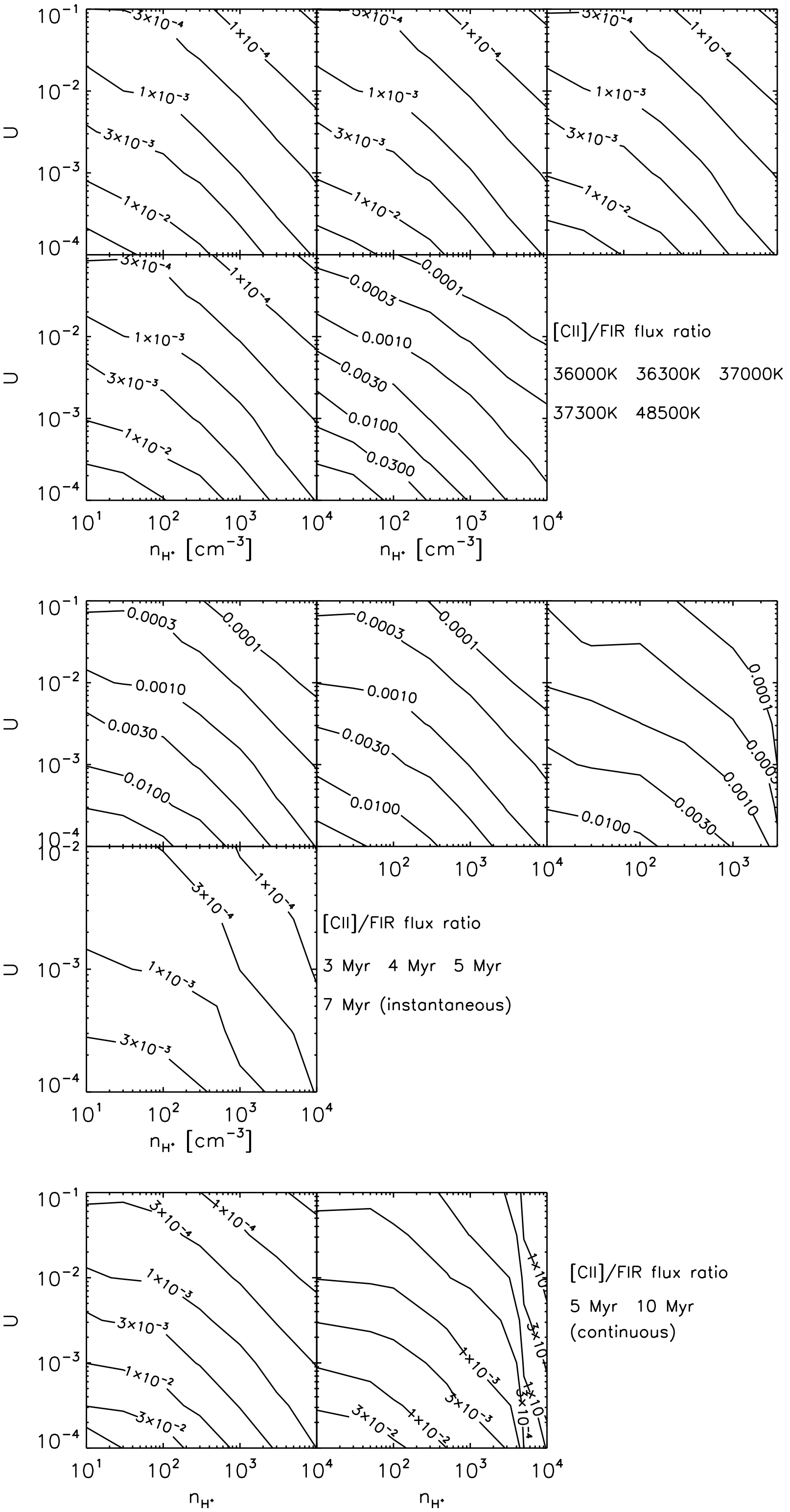

Figure A.11: Cloudy combined HII region/PDR models.

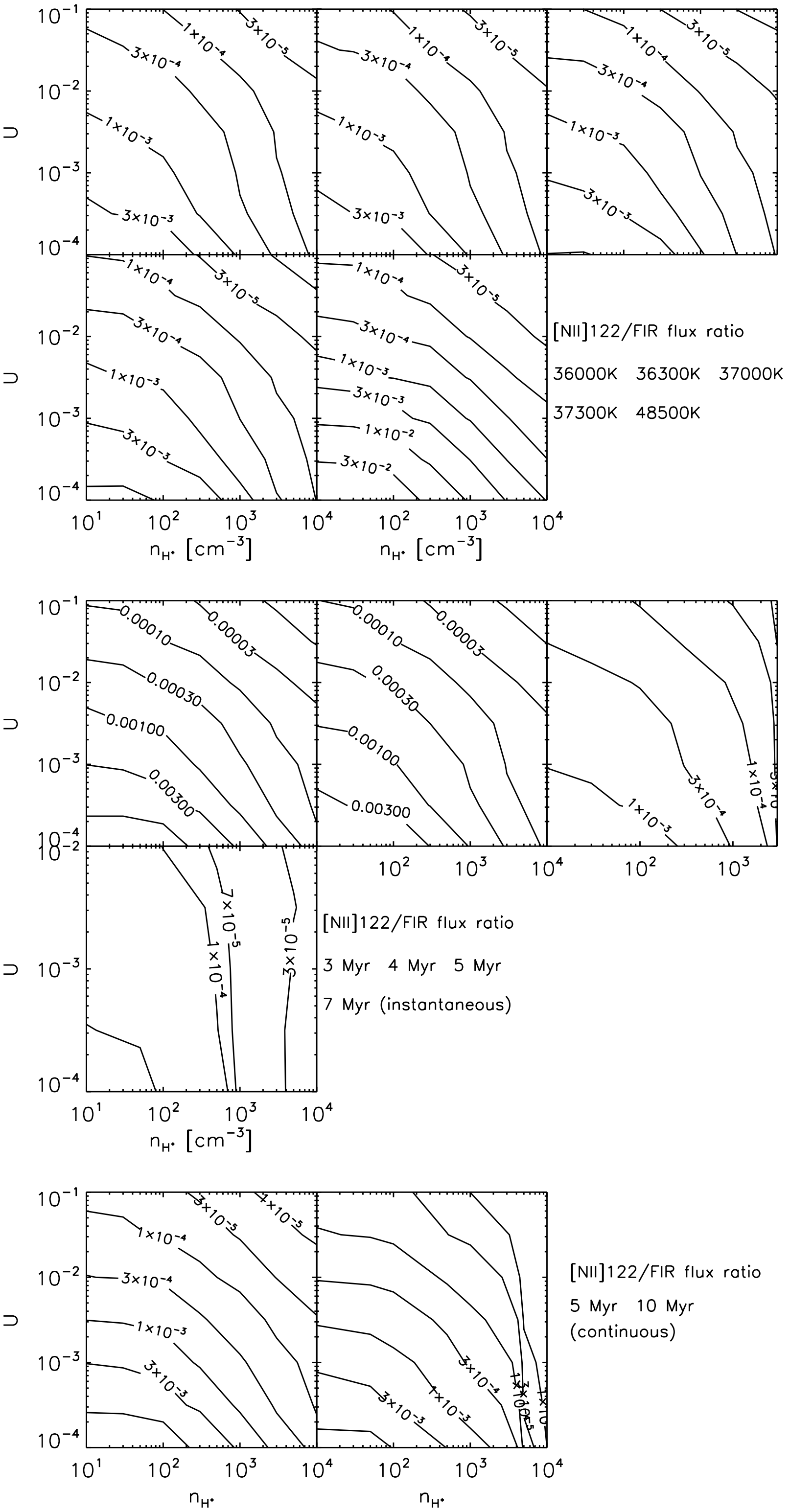

Figure A.12: Cloudy combined HII region/PDR models.

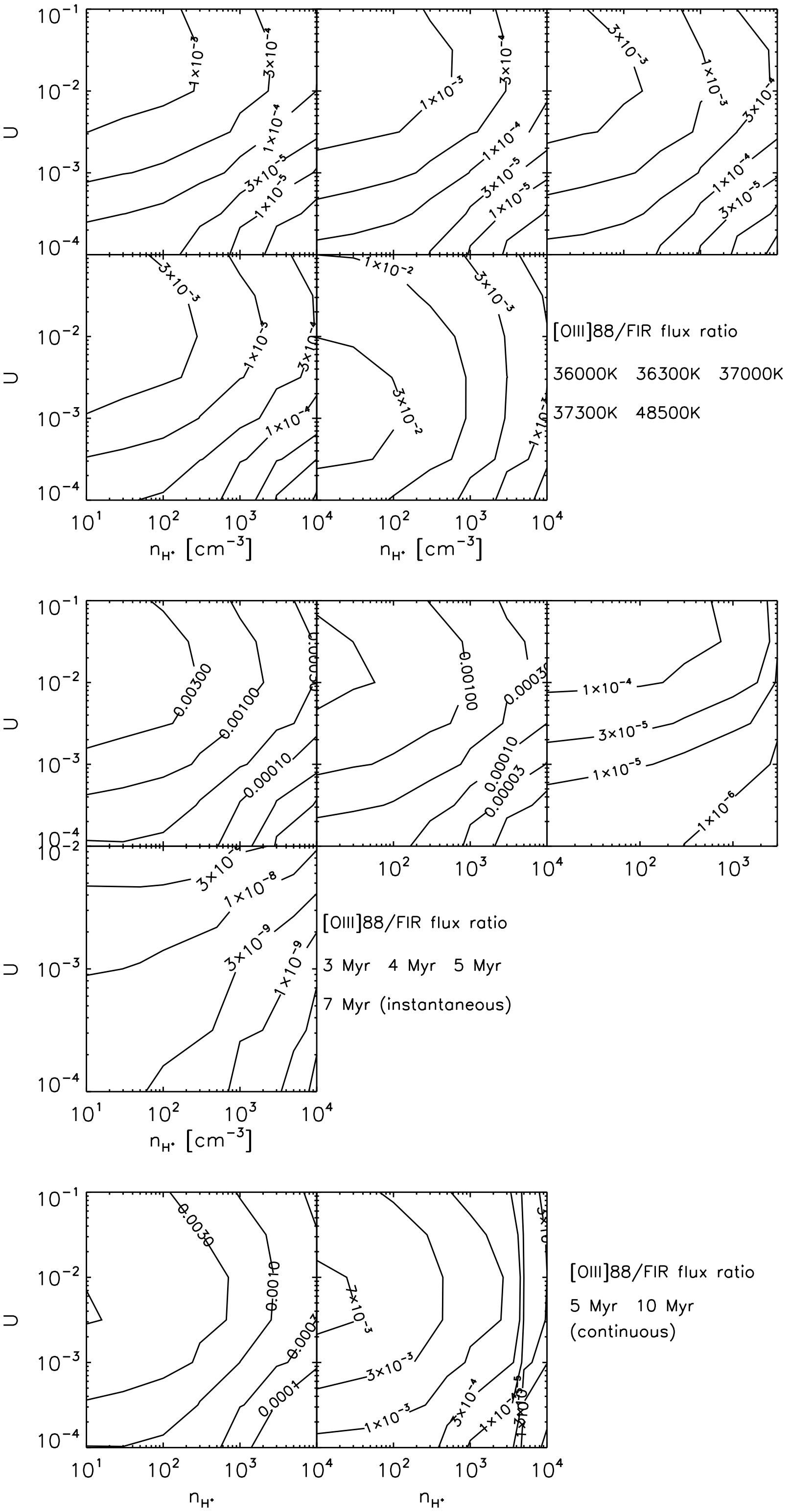

Figure A.13: Cloudy combined HII region/PDR models.

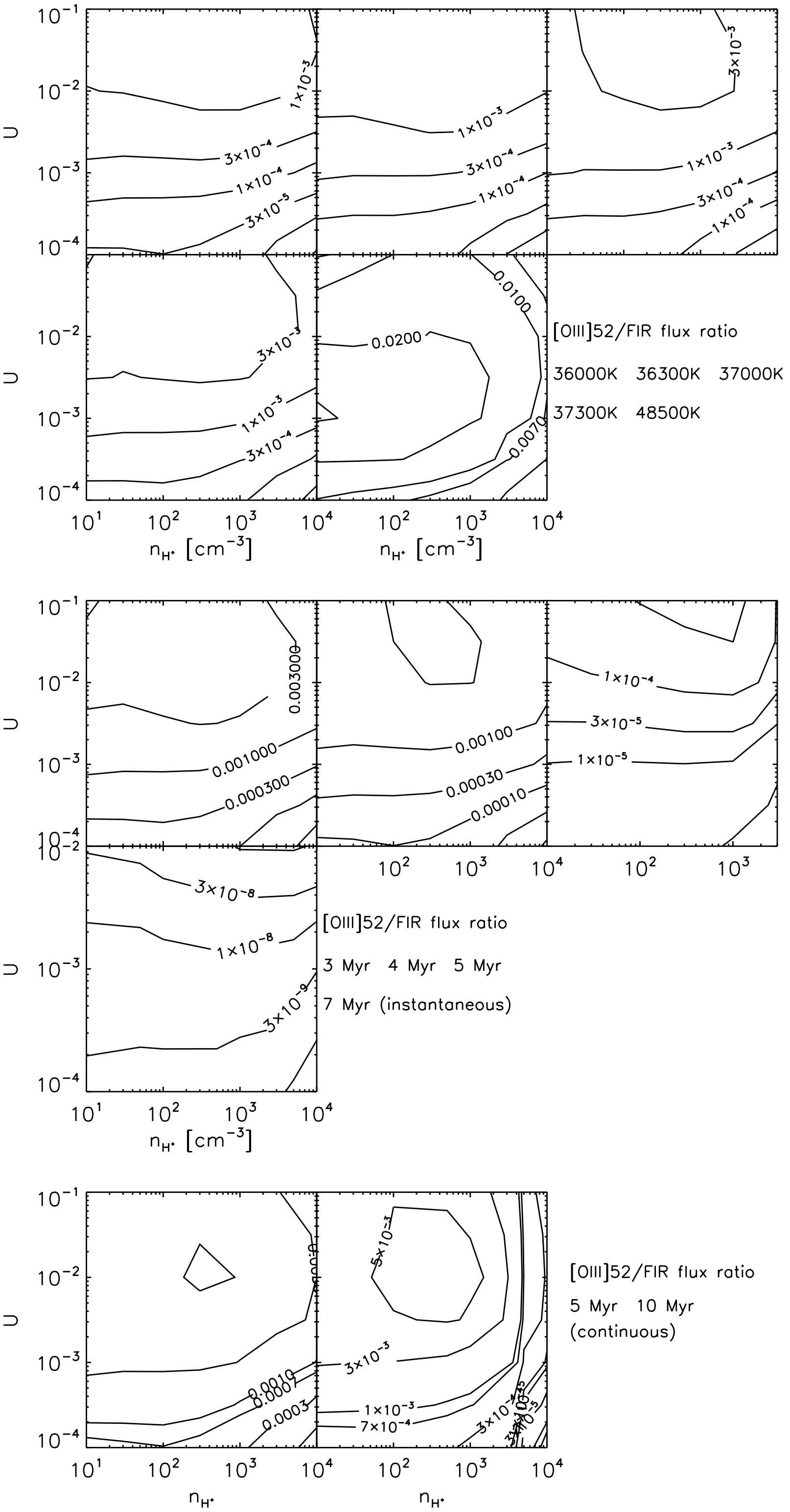

Figure A.14: Cloudy combined HII region/PDR models.

Appendix B

Appendix to Chapter1

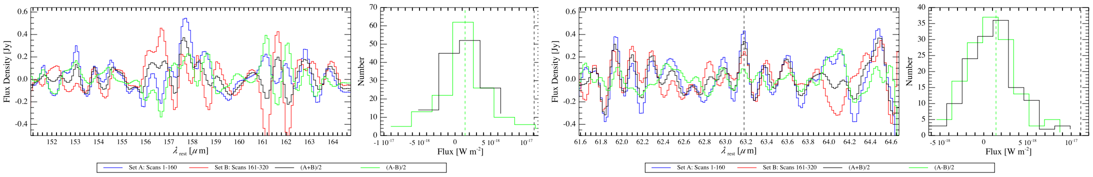

Figure B.1: Same as Figure 1.3, with SPIRE-FTS spectra for [CII]158μm and [OI]63μm in FSC 10214+4724 (top panel) and APM 08279+5255 (bottom panel), respectively.

In addition to the Cloverleaf, the high-redshift quasars APM 08279+5255 (z = 3.91), FSC 10214+4724 (z = 2.29), and MG 0751 (z = 3.20) were also targeted for observations with *Herschel* SPIRE-FTS in the `OT1_mbradfor_1` program . We present in this appendix the results of a search for [CII]158μm and [OI]63μm emission in these sources.

For FSC 10214+4724, we report a 2σ upper limit on the apparent [CII]158μm flux as $< 1.79 \times 10^{-17}$ W m^{-2}. We have have performed similar jackknife tests and flux uncertainty estimates as in Section 1.2 on the portion of the SPIRE-FTS spectrum containing the expected [CII]158μm emission, and show the original and jack-knifed spectrum, as well the histogram of fluxes for each wavelength position in the spectrum, in Figure B.1 (upper panel).

For APM 08279+5255, we report a 2σ upper limit on the apparent [OI]63μm flux as $< 1.34 \times 10^{-17}$ W m^{-2}. Orginal and jack-knifed spectrum, and flux histogram, are shown in Figure B.1 (lower panel). The redshifted [CII]158μm line for this source falls outside of the spectral coverage of SPIRE-FTS.

No detections or upper limits are reported for MG 0751.

Appendix C

Appendix to Chapter 2

To explore the effect of the luminosity function shape on the relative performances of intensity mapping and galaxy surveys in observing the [CII] power spectrum and mean intensity of [CII] emitters, we have introduced toy models to represent different $\Phi(L_{IR}, z) \equiv \frac{\mathrm{d}N}{\mathrm{d}L_{IR}\mathrm{dV}}$.

We parametrize our luminosity function as a Schechter function

$$\Phi(L_{IR}, z)\mathrm{d}L_{IR} = \phi_* \left(\frac{L_{IR}}{L_*}\right)^{\alpha} \exp\left(-\frac{L_{IR}}{L_*}\right) \mathrm{d}L_{IR} \tag{C.0.1}$$

where ϕ_* is the normalization for number density, L_* is the characteristic luminosity at the knee, and α is the faint-end slope, as usual.

Power-law luminosity functions are notoriously ill-behaved if the lower limit of integration for either the luminosity functions or its moments is extended to zero. Rather than implement a break in the power law, we simply cut it off at some $L_{IR,min}$ and choose to fix in our analysis the total IR luminosity density from galaxies as predicted by B11, denoted as ρ_{IR}^{B11}, such that

$$\int \mathrm{d}L_{IR}\phi_* L_* \left(\frac{L_{IR}}{L_*}\right)^{\alpha+1} \exp\left(-\frac{L_{IR}}{L_*}\right) \equiv \rho_{IR}^{\mathrm{B11}} \tag{C.0.2}$$

This is motivated by the observation that in many cases we do have constraints on the integrated light (from, for example, the cosmic infrared background or from the cosmic star formation rate density or the requirement of critical reionization), whereas we may not in general have detailed constraints on the distribution of light among galaxies, i.e., the shape of luminosity function.

The number density of sources, n_{gal}, can, in turn, be computed from

$$n_{gal} = \int \mathrm{d}L_{IR}\phi_* \left(\frac{L_{IR}}{L_*}\right)^{\alpha} \exp\left(-\frac{L_{IR}}{L_*}\right) \tag{C.0.3}$$

Finally, equation C.0.2 allows us to calculate the [CII] luminosity density for each IR-normalized toy model as

$$\rho_{[\mathrm{CII}]} = \int \mathrm{d}L_{IR}\phi_* L_* \left(\frac{L_{IR}}{L_*}\right)^{\alpha+1} f_{[\mathrm{CII}]} \exp\left(-\frac{L_{IR}}{L_*}\right) \tag{C.0.4}$$

where $f_{[\mathrm{CII}]}$ is the fraction of IR luminosity emitted in [CII], or $\frac{L_{[\mathrm{CII}]}(L_{IR})}{L_{IR}}$, described by the Spinoglio relations. Because $L_{[\mathrm{CII}]}$ is slightly sublinear in L_{IR}, it follows that the toy models with steep faint-end slopes will produce more [CII] emission than their flatter counterparts.

Bibliography

Abel, N. P., Ferland, G. J., Shaw, G., & van Hoof, P. A. M. 2005, ApJS, 161, 65

Alloin, D., Guilloteau, S., Barvainis, R., Antonucci, R., & Tacconi, L. 1997, A&A, 321, 24

Barvainis, R., Antonucci, R., & Coleman, P. 1992, ApJ, 399, L19

Barvainis, R., Maloney, P., Antonucci, R., & Alloin, D. 1997, ApJ, 484, 695

Barvainis, R., Tacconi, L., Antonucci, R., Alloin, D., & Coleman, P. 1994, Nature, 371, 586

Béthermin, M., Dole, H., Lagache, G., Le Borgne, D., & Penin, A. 2011, A&A, 529, A4

Bothwell, M. S. et al. 2013, ApJ, 779, 67

Bouwens, R. J. et al. 2014, ArXiv e-prints

Bradford, C. M. et al. 2009a, ApJ, 705, 112

Bradford, C. M. et al. 2009b, in Astronomical Society of the Pacific Conference Series, Vol. 417, Submillimeter Astrophysics and Technology: a Symposium Honoring Thomas G. Phillips, ed. D. C. Lis, J. E. Vaillancourt, P. F. Goldsmith, T. A. Bell, N. Z. Scoville, & J. Zmuidzinas, 341

Bradford, C. M. et al. 2012, in Society of Photo-Optical Instrumentation Engineers (SPIE) Conference Series, Vol. 8442, Society of Photo-Optical Instrumentation Engineers (SPIE) Conference Series

—. 2011, ApJ, 741, L37

—. 2015, ArXiv e-prints

Bradford, C. M., Nikola, T., Stacey, G. J., Bolatto, A. D., Jackson, J. M., Savage, M. L., Davidson, J. A., & Higdon, S. J. 2003, ApJ, 586, 891

Bradford, C. M., Stacey, G. J., Nikola, T., Bolatto, A. D., Jackson, J. M., Savage, M. L., & Davidson, J. A. 2005, ApJ, 623, 866

Braito, V. et al. 2004, A&A, 420, 79

Brauher, J. R., Dale, D. A., & Helou, G. 2008, ApJS, 178, 280

Breysse, P. C., Kovetz, E. D., & Kamionkowski, M. 2014, ArXiv e-prints

Brown, R. L. & Vanden Bout, P. A. 1991, AJ, 102, 1956

Burgarella, D. et al. 2013a, A&A, 554, A70

—. 2013b, A&A, 554, A70

Carilli, C. L. 2011, ApJ, 730, L30

Carilli, C. L. & Walter, F. 2013, ARA&A, 51, 105

Chang, T.-C., Pen, U.-L., Bandura, K., & Peterson, J. B. 2010, ArXiv e-prints 1007.3709

Cicone, C. et al. 2014, A&A, 562, A21

Colbert, E. J. M., Weaver, K. A., Krolik, J. H., Mulchaey, J. S., & Mushotzky, R. F. 2002, ApJ, 581, 182

Colbert, J. W. et al. 1999a, ApJ, 511, 721

—. 1999b, ApJ, 511, 721

Cooray, A. et al. 2010, A&A, 518, L22

Cooray, A. & Sheth, R. 2002, Phys. Rep., 372, 1

Cormier, D. et al. 2015, A&A, 578, A53

Daddi, E. et al. 2007, ApJ, 670, 156

Dale, D. A., Helou, G., Brauher, J. R., Cutri, R. M., Malhotra, S., & Beichman, C. A. 2004, ApJ, 604, 565

De Looze, I. et al. 2014, A&A, 568, A62

Díaz-Santos, T. et al. 2013, ApJ, 774, 68

Elbaz, D. et al. 2011, A&A, 533, A119

Fan, X. et al. 2006, AJ, 132, 117

Ferkinhoff, C. et al. 2011a, ApJ, 740, L29

—. 2011b, ApJ, 740, L29

Ferkinhoff, C., Brisbin, D., Nikola, T., Stacey, G. J., Sheth, K., Hailey-Dunsheath, S., & Falgarone, E. 2015, ApJ, 806, 260

Ferland, G. J., Korista, K. T., Verner, D. A., Ferguson, J. W., Kingdon, J. B., & Verner, E. M. 1998, PASP, 110, 761

Flower, D. R. & Pineau Des Forêts, G. 2010, MNRAS, 406, 1745

Garnett, D. R., Edmunds, M. G., Henry, R. B. C., Pagel, B. E. J., & Skillman, E. D. 2004, AJ, 128, 2772

Glenn, J. et al. 2010, MNRAS, 409, 109

Goldsmith, P. F. & Langer, W. D. 1978, ApJ, 222, 881

Gong, Y., Cooray, A., Silva, M., Santos, M. G., Bock, J., Bradford, C. M., & Zemcov, M. 2012, ApJ, 745, 49

Gong, Y., Cooray, A., Silva, M. B., Santos, M. G., & Lubin, P. 2011, ApJ, 728, L46

Graciá-Carpio, J. et al. 2011, ApJ, 728, L7

Greve, T. R. et al. 2014, ApJ, 794, 142

Groves, B. A., Dopita, M. A., & Sutherland, R. S. 2004, ApJS, 153, 9

Hailey-Dunsheath, S., Nikola, T., Stacey, G. J., Oberst, T. E., Parshley, S. C., Benford, D. J., Staguhn, J. G., & Tucker, C. E. 2010a, ArXiv e-prints 1003.2174

—. 2010b, ApJ, 714, L162

Hailey-Dunsheath, S. et al. 2012, ApJ, 755, 57

Hazard, C., Morton, D. C., Terlevich, R., & McMahon, R. 1984, ApJ, 282, 33

Heckman, T. M. & Best, P. N. 2014, ARA&A, 52, 589

Hogg, D. W. 1999, ArXiv Astrophysics e-prints

Hollenbach, D. J. & Tielens, A. G. G. M. 1997, ARA&A, 35, 179

Hopkins, A. M. & Beacom, J. F. 2006a, ApJ, 651, 142

—. 2006b, ApJ, 651, 142

Joy, M., Lester, D. F., & Harvey, P. M. 1987, ApJ, 319, 314

Jullo, E. et al. 2012, ApJ, 750, 37

Kamenetzky, J. et al. 2012, ApJ, 753, 70

Kamenetzky, J., Rangwala, N., Glenn, J., Maloney, P. R., & Conley, A. 2014, ApJ, 795, 174

Kaufman, M. J., Wolfire, M. G., & Hollenbach, D. J. 2006, ApJ, 644, 283

Kennicutt, Jr., R. C. 1998a, ARA&A, 36, 189

—. 1998b, ApJ, 498, 541

Komossa, S., Burwitz, V., Hasinger, G., Predehl, P., Kaastra, J. S., & Ikebe, Y. 2003, ApJ, 582, L15

Lebouteiller, V. et al. 2012, A&A, 548, A91

Lester, D. F., Dinerstein, H. L., Werner, M. W., Watson, D. M., Genzel, R., & Storey, J. W. V. 1987, ApJ, 320, 573

Li, A. & Draine, B. T. 2001, ApJ, 554, 778

Lidz, A., Furlanetto, S. R., Oh, S. P., Aguirre, J., Chang, T.-C., Doré, O., & Pritchard, J. R. 2011a, ApJ, 741, 70

—. 2011b, ApJ, 741, 70

Lidz, A., Zahn, O., Furlanetto, S. R., McQuinn, M., Hernquist, L., & Zaldarriaga, M. 2009, ApJ, 690, 252

Luhman, M. L. et al. 1998, ApJ, 504, L11

Lutz, D. et al. 2007, ApJ, 661, L25

Madau, P. & Dickinson, M. 2014, ARA&A, 52, 415

Magain, P., Surdej, J., Swings, J.-P., Borgeest, U., & Kayser, R. 1988, Nature, 334, 325

Malhotra, S. et al. 1997, ApJ, 491, L27

—. 2001, ApJ, 561, 766

Maloney, P. R., Hollenbach, D. J., & Tielens, A. G. G. M. 1996, ApJ, 466, 561

Meijerink, R. et al. 2013, ApJ, 762, L16

Meijerink, R., Spaans, M., Loenen, A. F., & van der Werf, P. P. 2011, A&A, 525, A119

Morales, M. F. & Wyithe, J. S. B. 2010, ARA&A, 48, 127

Mortlock, D. J. et al. 2011, Nature, 474, 616

Nagao, T., Maiolino, R., Marconi, A., & Matsuhara, H. 2011, A&A, 526, A149

Oberst, T. E. et al. 2006, ApJ, 652, L125

Osterbrock, D. E. 1989, Astrophysics of gaseous nebulae and active galactic nuclei

Ott, S. 2010, in Astronomical Society of the Pacific Conference Series, Vol. 434, Astronomical Data Analysis Software and Systems XIX, ed. Y. Mizumoto, K.-I. Morita, & M. Ohishi, 139

Panuzzo, P. et al. 2010, A&A, 518, L37

Parsons, A. R. et al. 2013, ArXiv e-prints 1304.4991

Planck Collaboration et al. 2013, ArXiv e-prints

Press, W. H. & Schechter, P. 1974, ApJ, 187, 425

Pullen, A., Dore, O., & Bock, J. 2013a, ArXiv e-prints

Pullen, A. R., Chang, T.-C., Doré, O., & Lidz, A. 2013b, ApJ, 768, 15

Rangwala, N. et al. 2011, ApJ, 743, 94

Riechers, D. A. et al. 2014, ArXiv e-prints

—. 2011a, ApJ, 739, L32

Riechers, D. A., Walter, F., Carilli, C. L., Cox, P., Weiss, A., Bertoldi, F., & Menten, K. M. 2011b, ApJ, 726, 50

Riechers, D. A., Walter, F., Carilli, C. L., Weiss, A., Bertoldi, F., Menten, K. M., Knudsen, K. K., & Cox, P. 2006, ApJ, 645, L13

Riechers, D. A., Walter, F., Cox, P., Carilli, C. L., Weiss, A., Bertoldi, F., & Neri, R. 2007, ApJ, 666, 778

Robertson, B. E., Ellis, R. S., Furlanetto, S. R., & Dunlop, J. S. 2015, ApJ, 802, L19

Rosenberg, M. J. F. et al. 2015, ApJ, 801, 72

Rubin, R. H. 1985, ApJS, 57, 349

Sargsyan, L. et al. 2012, ApJ, 755, 171

Schaerer, D. & de Koter, A. 1997, A&A, 322, 598

Sheth, R. K., Mo, H. J., & Tormen, G. 2001, MNRAS, 323, 1

Smith, R. E. et al. 2003, MNRAS, 341, 1311

Solomon, P., Vanden Bout, P., Carilli, C., & Guelin, M. 2003, Nature, 426, 636

Spinoglio, L., Dasyra, K. M., Franceschini, A., Gruppioni, C., Valiante, E., & Isaak, K. 2012a, ApJ, 745, 171

Spinoglio, L. et al. 2012b, ApJ, 758, 108

Spinoglio, L., Tommasin, S., & Malkan, M. A. 2009, in Revista Mexicana de Astronomia y Astrofisica Conference Series, Vol. 37, Revista Mexicana de Astronomia y Astrofisica Conference Series, 120–131

Springel, V. et al. 2005, Nature, 435, 629

Stacey, G. J., Hailey-Dunsheath, S., Ferkinhoff, C., Nikola, T., Parshley, S. C., Benford, D. J., Staguhn, J. G., & Fiolet, N. 2010a, ApJ, 724, 957

Stacey, G. J., Hailey-Dunsheath, S., Ferkinhoff, C. an d Nikola, T., Parshley, S. C., Benford, D. J., Staguhn, J. G., & Fiolet, N. 2010b, ApJ, 724, 957

Suchkov, A., Allen, R. J., & Heckman, T. M. 1993, ApJ, 413, 542

Suginohara, M., Suginohara, T., & Spergel, D. N. 1999, ApJ, 512, 547

Switzer, E. R. et al. 2013, MNRAS, 434, L46

Tacconi, L. J., Genzel, R., Tecza, M., Gallimore, J. F., Downes, D., & Scoville, N. Z. 1999, ApJ, 524, 732

Tielens, A. G. G. M. 2005, The Physics and Chemistry of the Interstellar Medium

Tingay, S. J. et al. 2013, Journal of Physics Conference Series, 440, 012033

Uzgil, B. D., Aguirre, J. E., Bradford, C. M., & Lidz, A. 2014, ApJ, 793, 116

van der Werf, P. P. et al. 2011, ApJ, 741, L38

—. 2010, A&A, 518, L42

van Dishoeck, E. F. & Black, J. H. 1986, ApJS, 62, 109

Vasta, M., Barlow, M. J., Viti, S., Yates, J. A., & Bell, T. A. 2010, MNRAS, 404, 1910

Venturini, S. & Solomon, P. M. 2003, ApJ, 590, 740

VERITAS Collaboration et al. 2009, Nature, 462, 770

Viero, M. P. et al. 2012, ArXiv e-prints

Visbal, E. & Loeb, A. 2010, J. Cosmology Astropart. Phys., 11, 16

Visbal, E., Trac, H., & Loeb, A. 2011, J. Cosmology Astropart. Phys., 8, 10

Weiß, A., Downes, D., Henkel, C., & Walter, F. 2005, A&A, 429, L25

Weiß, A., Henkel, C., Downes, D., & Walter, F. 2003, A&A, 409, L41

White, S. D. M. & Rees, M. J. 1978, MNRAS, 183, 341

Wise, J. H., Demchenko, V. G., Halicek, M. T., Norman, M. L., Turk, M. J., Abel, T., & Smith, B. D. 2014, MNRAS, 442, 2560

Wolfire, M. G., Tielens, A. G. G. M., & Hollenbach, D. 1990, ApJ, 358, 116